Calhoun: The NPS Institutional Archive

DSpace Repository

Theses and Dissertations | 1. Thesis and Dissertation Collection, all items

2013-03

MESOSCALE SIMULATIONS OF COASTAL CIRCULATIONS EVALUATED USING MEASUREMENTS FROM A DENSE MESO NETWORK

Muggelberg, Daniel B.

Monterey, California. Naval Postgraduate School

http://hdl.handle.net/10945/32874

Downloaded from NPS Archive: Calhoun

http://www.nps.edu/library

Calhoun is the Naval Postgraduate School's public access digital repository for research materials and institutional publications created by the NPS community. Calhoun is named for Professor of Mathematics Guy K. Calhoun, NPS's first appointed -- and published -- scholarly author.

Dudley Knox Library / Naval Postgraduate School
411 Dyer Road / 1 University Circle
Monterey, California USA 93943

NAVAL POSTGRADUATE SCHOOL

MONTEREY, CALIFORNIA

THESIS

MESOSCALE SIMULATIONS OF COASTAL CIRCULATIONS EVALUATED USING MEASUREMENTS FROM A DENSE MESO NETWORK

by

Daniel B. Muggelberg

March 2013

Thesis Advisor: Qing Wang
Second Reader: Wendell Nuss

Approved for public release; distribution is unlimited

THIS PAGE INTENTIONALLY LEFT BLANK

REPORT DOCUMENTATION PAGE			Form Approved OMB No. 0704–0188
Public reporting burden for this collection of information is estimated to average 1 hour per response, including the time for reviewing instruction, searching existing data sources, gathering and maintaining the data needed, and completing and reviewing the collection of information. Send comments regarding this burden estimate or any other aspect of this collection of information, including suggestions for reducing this burden, to Washington headquarters Services, Directorate for Information Operations and Reports, 1215 Jefferson Davis Highway, Suite 1204, Arlington, VA 22202–4302, and to the Office of Management and Budget, Paperwork Reduction Project (0704–0188) Washington DC 20503.			
1. AGENCY USE ONLY *(Leave blank)*	**2. REPORT DATE** March 2013	**3. REPORT TYPE AND DATES COVERED** Master's Thesis	
4. TITLE AND SUBTITLE: MESOSCALE SIMULATIONS OF COASTAL CIRCULATIONS EVALUATED USING MEASUREMENTS FROM A DENSE MESO NETWORK			**5. FUNDING NUMBERS**
6. AUTHOR(S) Daniel B. Muggelberg			
7. PERFORMING ORGANIZATION NAME(S) AND ADDRESS(ES) Naval Postgraduate School Monterey, CA 93943–5000			**8. PERFORMING ORGANIZATION REPORT NUMBER**
9. SPONSORING /MONITORING AGENCY NAME(S) AND ADDRESS(ES) N/A			**10. SPONSORING/MONITORING AGENCY REPORT NUMBER**
11. SUPPLEMENTARY NOTES The views expressed in this thesis are those of the author and do not reflect the official policy or position of the Department of Defense or the U.S. Government. I.R.B. Protocol number N/A.			
12a. DISTRIBUTION / AVAILABILITY STATEMENT Approved for public release; distribution is unlimited			**12b. DISTRIBUTION CODE**

13. ABSTRACT (maximum 200 words)

This research focuses on the evaluation of a mesoscale model in simulating coastal sea-breeze circulations. Measurements for this purpose were made from a mesonetwork consisting of 36 towers and five Doppler Wind Profilers as part of the Weather Information Network Display System at Cape Canaveral Air Force Station, Florida. The tower measurements provides observations of wind, temperature, and humidity from at least one level on each tower, while 17 of the towers have two common levels that allow calculations of surface momentum flux and sensible and latent heat fluxes. For this research, two five-day periods are chosen for analyses and model verification of temporal and spatial variability of sea breeze circulations against high-resolution simulations from the U.S. Navy's Coupled Ocean-Atmosphere Mesoscale Prediction System (COAMPS^{TM}). In addition to traditional statistical method of model evaluation, this research also evaluated how the error statistics vary spatially relative to distance from the coastline, an unprecedented approach to studies in this region. Results from this study suggests general adequacy of COAMPS^{TM} in simulating the diurnal variation of the sea breeze circulation. However, significant errors result in some of the variables, such as surface fluxes.

14. SUBJECT TERMS Land-Sea Breeze, Atmospheric Boundary Layer, Turbulence, Momentum Flux, Heat Flux, Flux-Profile Relationship, Monin-Obukhov Similarity Theory, Bulk Aerodynamic Formulations, Mesoscale Modeling, COAMPS^{TM}	**15. NUMBER OF PAGES** 107
	16. PRICE CODE

17. SECURITY CLASSIFICATION OF REPORT	**18. SECURITY CLASSIFICATION OF THIS PAGE**	**19. SECURITY CLASSIFICATION OF ABSTRACT**	**20. LIMITATION OF ABSTRACT**
Unclassified	Unclassified	Unclassified	UU

NSN 7540–01–280–5500 Standard Form 298 (Rev. 2–89)
Prescribed by ANSI Std. 239–18

THIS PAGE INTENTIONALLY LEFT BLANK

Approved for public release; distribution is unlimited

MESOSCALE SIMULATIONS OF COASTAL CIRCULATIONS EVALUATED USING MEASUREMENTS FROM A DENSE MESO NETWORK

Daniel B. Muggelberg
Captain, United States Air Force
B.S., The Florida State University, 2006

Submitted in partial fulfillment of the
requirements for the degree of

MASTER OF SCIENCE IN METEOROLOGY

from the

NAVAL POSTGRADUATE SCHOOL
March 2013

Author: Daniel B. Muggelberg

Approved by: Qing Wang
Thesis Advisor

Wendell Nuss
Second Reader

Wendell Nuss
Chair, Department of Meteorology

THIS PAGE INTENTIONALLY LEFT BLANK

ABSTRACT

This research focuses on the evaluation of a mesoscale model in simulating coastal sea-breeze circulations. Measurements for this purpose were made from a mesonetwork consisting of 36 towers and five Doppler Wind Profilers as part of the Weather Information Network Display System at Cape Canaveral Air Force Station, Florida. The tower measurements provides observations of wind, temperature, and humidity from at least one level on each tower, while 17 of the towers have two common levels that allow calculations of surface momentum flux and sensible and latent heat fluxes. For this research, two five-day periods are chosen for analyses and model verification of temporal and spatial variability of sea breeze circulations against high-resolution simulations from the U.S. Navy's Coupled Ocean-Atmosphere Mesoscale Prediction System (COAMPS^{TM}). In addition to traditional statistical method of model evaluation, this research also evaluated how the error statistics vary spatially relative to distance from the coastline, an unprecedented approach to studies in this region. Results from this study suggests general adequacy of COAMPS^{TM} in simulating the diurnal variation of the sea breeze circulation. However, significant errors result in some of the variables, such as surface fluxes.

THIS PAGE INTENTIONALLY LEFT BLANK

TABLE OF CONTENTS

I. INTRODUCTION....1
- **A. COASTAL SEA AND LAND BREEZE CIRCULATIONS....1**
- **B. COASTAL ATMOSPHERIC BOUNDARY LAYERS....2**
- **C. MESOSCALE MODEL SIMULATIONS OF COASTAL CIRCULATIONS....5**
- **D. PURPOSE AND OVERVIEW....6**
- **E. MILITARY APPLICATIONS....7**

II. BACKGROUND INFORMATION....9
- **A. COASTAL THERMAL CIRCULATIONS....9**
  - **1. Factors Affecting Sea Breeze Circulations from Previous Simulations....10**
    - ***a. Sensible Heat Flux (SHF)....11***
    - ***b. Ambient Geostrophic Wind (V_g)....11***
    - ***c. Thermal Stability (N)....11***
    - ***d. Moisture (q)....12***
    - ***e. Water Body Dimension (d)....12***
    - ***f. Shoreline Curvature (r)....12***
    - ***g. Coriolis Force (f)....13***
    - ***h. Roughness Length (z_0)....13***
  - **2. Previous Studies of Coastal Circulation over KSC/CCAFS....13**
- **B. SURFACE LAYER AND SURFACE FLUX CALCULATION....15**
- **C. SURFACE FLUX PARAMETERIZATION IN MESOSCALE MODELS....18**
  - **1. Bulk Aerodynamic Parameterizations....20**
  - **2. Roughness Length in Numerical Models....21**

III. DATA PROCESSING AND SELECTED CASES....23
- **A. LOWER TROPOSPHERE OBSERVATIONS....23**
  - **1. Weather Information Network Display System (WINDS)....23**
  - **2. Doppler Radar Wind Profilers (DRWP)....24**
  - **3. Past Studies using KSC/CCAFS Mesonetwork....25**
- **B. DATA ORGANIZATION AND QUALITY CONTROL....25**
- **C. COAMPS™ MODEL SIMULATION....27**

IV. KSC/CCAFS OBSERVED SEA BREEZE CIRCULATIONS....31
- **A. MEASURES OF VARIABILITY....31**
  - **1. Temporal Variability....31**
  - **2. Spatial Variability....39**
  - **3. Surface Layer Evolution....45**

V. EVALUATION OF COAMPS™ SIMULATED COASTAL CIRCULATIONS....49
- **A. RESULTS FOR SELECTED CASES....51**

1. Case #1, 1–5 June 2008 51
2. Case #2, 18–22 June 2008 61
3. Sea and Land Breeze Transition 66
B. STATISTICAL EVALUATION 69
VI. SUMMARY AND CONCLUSION 77
A. SUMMARY 77
B. RECOMMENDATION FOR FUTURE RESEARCH 80
APPENDIX. CCAFS WINDS TOWER LOCATIONS AND INSTRUMENT COMPLEMENTS 83
LIST OF REFERENCES 85
INITIAL DISTRIBUTION LIST 89

LIST OF FIGURES

Figure 1. Diagram of an internal boundary layer (From Stull, 1988). 3
Figure 2. Growth of a convective TIBL (From Stull 1988). 4
Figure 3. Characteristics of sea breeze horizontal (l) and vertical (h) length scales and horizontal (u) and vertical (w) speed (From Crosman and Horel 2010) ...10
Figure 4. Contour plots of roughness length from (a) COAMPS^{TM} and (b) calculated z_0 from WINDS at 1200 EST on 21 June 2008. 22
Figure 5. Meteorological instrumentation distribution on KSC/CCAFS (From Wang, 2011). 24
Figure 6. Contour plot of potential temperature measured at 1.8 m at 1200 EST on 1 June 2008. A SBF is clearly seen in this figure in the region of dense isotherms. 27
Figure 7. COAMPS^{TM} model nested boundaries for simulations in this study. 28
Figure 8. COAMPS^{TM} generated contour plot of 1.8 m potential temperature at 1200 EST on 1 June 2008. 29
Figure 9. Temporal variations of observed wind speed (WS), wind direction (WD), potential temperature (θ) and specific humidity (q) from Tower 0313 for Case #1. 32
Figure 10. Temporal variations of calculated latent and sensible heat flux and momentum flux from Tower 0313 33
Figure 11. Temporal variations of observed wind speed, wind direction, potential temperature and specific humidity from Tower 0002 for Case #1. 34
Figure 12. Temporal variations of calculated latent and sensible heat flux and momentum flux from Tower 0002 35
Figure 13. Time series of wind speed, wind direction, potential temperature and specific humidity from Tower 0110 in Case #2. 36
Figure 14. Time series of calculated latent and sensible heat fluxes and momentum flux from Tower 0110 in Case #2. 37
Figure 15. Time series of wind speed, wind direction, potential temperature, specific humidity from Tower 0006 in Case #2. 38
Figure 16. Time series of calculated latent and sensible heat flux and momentum flux from Tower 0006 in Case #2. 39
Figure 17. Contour plots of WINDS measured potential temperature distribution at (a) 1000, (b) 1200, (c) 1400 and (d) 1600 EST on 1 June 2008. 40
Figure 18. Contour plots of WINDS measured potential temperature distribution at (a) 0900, (b) 1100, (c) 1300 and (d) 1500 EST on 18 June 2008 41
Figure 19. Same as in Figure 17, except for sensible heat flux (SHF from 17 towers). ...42
Figure 20. Wind speeds (ms^{-1}) from DWRP (a) 1, (b) 2, (c) 3 and (d) 5 for Case #1 43
Figure 21. Wind direction from DWRP (a) 1, (b) 2, (c) 3 and (d) 5 for Case #1 44
Figure 22. Vertical profiles of potential temperature, specific humidity, wind speed and direction from Tower 0313 (top) and Tower 0110 (bottom) every three hours on 3 June 2008 46

Figure 23. Vertical profiles of potential temperature, specific humidity, wind speed and direction from Tower 0313 shortly before, during and after SBF passage on 1 June 2008. 47
Figure 24. Series of surface observation charts for (a) 1, (b) 4, (c) 18 and (d) 21 June 2008 at 1200 UTC (From NOAA). 52
Figure 25. Contour plots comparing COAMPS^{TM} (left) and WINDS observations (right) of potential temperature at (a) 1000, (b) 1200 and (c) 1400 on 2 June 2008. 54
Figure 26. WINDS (red) and COAMPS^{TM} (blue) vertical profiles of potential temperature, specific humidity, wind speed, and wind direction from T ower 0313 at 0600 (top) and 1200 (bottom) EST on 2 June 2008. 56
Figure 27. COAMPS^{TM} interpolated time-height wind speed (ms^{-1}) plots at DWRP (a) 1, (b) 2, (c) 3 and (d) 5. 58
Figure 28. COAMPS^{TM} interpolated time-height wind direction (deg) plots at DWRP (a) 1, (b) 2, (c) 3 and (d) 5. 59
Figure 29. WINDS observation (red) and COAMPS^{TM} (blue) of (a) mean and (b) calculated flux values at Tower 0313 (top) and 0006 (bottom) for Case #1. ..61
Figure 30. Contour plots comparing COAMPS^{TM} (left) and WINDS observations (right) of potential temperature at (a) 1100, (b) 1200 and (c) 1400 on 19 June 2008. 62
Figure 31. Observed (red) and COAMPS^{TM}-derived (blue) vertical profiles of potential temperature, specific humidity, wind speed, and wind direction from Tower 0313 at 0600 (top) and 1200 (bottom) EST on 20 June 2008. 64
Figure 32. WINDS observation (red) and COAMPS^{TM} (blue) of (a) mean and (b) calculated fluxes at Towers 0313 (top) and 0110 (bottom) from Case #2. 66
Figure 33. Locations of WINDS towers used for subjective analysis in this study. 67
Figure 34. Subjectively analyzed WINDS observation (red) and COAMPS^{TM} (blue) mean time for (a) sea breeze onset; (b) land breeze onset and (c) sea breeze duration. 69
Figure 35. Scatterplot comparing COAMPS^{TM} and observations of (a) potential temperature, (b) specific humidity, (c) wind speed and (d) wind direction color coded by day (legend in θ) in case #1 and #2 to show temporal error variances. 71
Figure 36. Scatterplots comparing COAMPS^{TM} and observation of (a) sensible heat, (b) momentum and (c) latent heat fluxes at the coast (left) and inland (right) color coded by each day (legend in MFL) in case #1 and #2 to show temporal error variances. 73
Figure 37. Error bias Contour Error Maps of observation and COAMPS^{TM} for (a) potential temperature, (b) specific humidity, (c) wind speed, and (d) wind direction with distance from shore. 74
Figure 38. Statistical analysis of observation and COAMPS^{TM} for (a) potential temperature, (b) specific humidity, (c) wind speed, (d) wind direction, (e) sensible heat flux and (f) momentum flux with distance from shore. 76

LIST OF TABLES

Table 1. Table of objective statistics used in this study. 50
Table 2. Statistical skill score of select COAMPS™ forecast vs. observation variables 72
Table 3. Locations and instrumentation heights for the four launch critical WINDS towers and CCAFS used in this study (After CSR 2006). 83
Table 4. Locations and instrumentation heights for the 14 safety critical WINDS towers at CCAFS used in this study (After CSR 2006). 84

THIS PAGE INTENTIONALLY LEFT BLANK

LIST OF ACRONYMS AND ABBREVIATIONS

14 WS	14th Weather Squadron, formerly AFCCC
45 WS	45th Weather Squadron
ABL	Atmospheric boundary layer
AFB	Air Force Base
AFCCC	Air Force Combat Climatology Center
AGL	(Elevation) above ground level
CCAFS	Cape Canaveral Air Force Station
CSR	Computer Sciences Raytheon
COAMPS™	Coupled-Ocean-Atmospheric Mesoscale Prediction System
EDT	Eastern Daylight Time
F	Fahrenheit
K	Kelvin
MHz	Mega-Hertz
MSL	(Elevation above) mean sea level
NASA	National Aeronautics and Space Administration
NPS	Naval Postgraduate School
RH	Relative humidity
RASS	Radio Acoustic Sounding System
ROCC	Range Operations Control Center
SI	*Système International d'unités* [International System of Units]
SBF	Sea-breeze front
TKE	Turbulence kinetic energy
UTC	Universal Time Coordinated
USN	United States Navy
WINDS	Weather Information Network Display System
WMO	World Meteorological Organization

THIS PAGE INTENTIONALLY LEFT BLANK

ACKNOWLEDGMENTS

The author wishes to express his gratitude to Professor Wang of the Meteorology Department at the Naval Postgraduate School (NPS). Without her expertise, patience and key insights, this thesis would not have been made possible.

I dedicate this thesis to my late mother, Barbara Ann Mulkey (1954–2002), who taught me the value of perseverance and a good education; and to my wife, Crystal Carter Muggelberg, and son, James Daniel Muggelberg, for their love, support and sympathy throughout the thesis process.

THIS PAGE INTENTIONALLY LEFT BLANK

I. INTRODUCTION

A. COASTAL SEA AND LAND BREEZE CIRCULATIONS

The sea breeze circulation occurs regularly at many coastal locations during the warmer seasons. Thermal gradients between cool water and warm land surfaces force an acute atmospheric response to resolve this imbalance. This response forces warm air to rise and drives cooler air residing over water to fill vacated space left by rising warmer air mass over land. A sea breeze front (SBF) develops at the leading edge of this advective air mass and advances inland as the day progresses. Subsequent development of sensible weather phenomena resulting from SBF is a primary concern to populations and the numerous Department of Defense installations lying within 50 miles of a coastal interface. Thus, the overarching goal of this research is to improve analyses and forecasts of weather, climate, and environmental conditions in coastal zones.

The fundamental properties and dynamic variability of diurnally-driven SBFs have been extensively studied and documented (Miller et al. 2003). Heat capacity, conductivity and emissivity of water differ compared to land which produce small scale variation in surface heat fluxes, boundary layer eddies and internal boundary layer growth. Thermal gradients caused by these diverse thermal properties between land and water drive onshore flow during the day (sea breeze) and offshore flow at night (land breeze). During a sea breeze event, surface onshore flow is compensated in the upper levels by offshore flow at the top of the boundary layer. This relationship is known as a thermally direct circulation. At night, an opposite sense of the thermally direct circulation can develop with cooler inland air advancing offshore as a land breeze. These circulations are typically observed to reach between 500–2000 m deep and are obviously dependent on the magnitude of horizontal temperature gradient, which is seasonably variable.

Detailed relationships between physical exchanges of mass (including water and solid constituents), momentum, and energy exchanges between the Earth's surface and the atmosphere remain unresolved and an area of active research. Rigorous theoretical and mathematical treatment of these exchanges, or fluxes, has yielded numerous

techniques for calculating intricate boundary layer physics required for sea breeze formation. However, influences of surface inhomogeneity and nonlinearity of small-scale flow structures near the Earth's surface are extremely complicated and create problems with depicting such mesoscale phenomena. It is precisely these heterogeneities that define the essential mechanics of boundary layer turbulence. Given the mathematical difficulty that inclusion of higher-order nonlinearities imparts to the treatment of the boundary layer, numerical simulation are dependent upon decades of experimentation and computer modeling endeavors. Such studies have yielded numerous techniques for "parameterizing" the effects of turbulent fluxes in mesoscale models. To facilitate this study, a brief discussion of useful terminology and concepts follows.

B. Coastal Atmospheric Boundary Layers

The portion of the lower atmosphere extending vertically from the Earth's surface to a variable height between 100–3000 m comprises the atmospheric boundary layer (ABL) (Stull 1988); so called because it loosely defines the fluid boundary between the nongaseous surface of the earth and the remainder of the atmosphere (hereinafter the free atmosphere). More precisely, we qualitative define the ABL as that portion of the troposphere in close proximity to the Earth's surface whose internal flow characteristics respond to forcing from surface features with a time scale of an hour or less. The ABL is quite variable in time and space while the free atmosphere shows little diurnal variation.

The ABL contains several component layers discernible by their physical properties. Nearest to the surface, usually ranging no higher than a few centimeters in depth is the interfacial, or viscous, layer. It is only in this thin envelope of air directly in contact with the surfaces which transport of physical fields via turbulence is less efficient than by molecular transport (Stull 1988). Above the viscous layer, the lowest 10% to 15% (by depth) of the boundary layer is called the surface, or constant flux layer. In this layer, fluxes of momentum and energy are approximately constant in the vertical, and variations in the wind field are most directly attributable to static stability and local frictional effects. The influence of the Earth's rotation is insignificant and often neglected in the surface layer (Kaimal and Finnigan 1994).

The coastal region is characteristic of spatial heterogeneity with the coastline separating the ocean and the land mass. As such, the adjacent boundary layer is quite complicated. Associated with the onshore and offshore flow from sea breeze and land breeze circulations, the low level boundary layer air is modified by changing surface properties as it is advected downwind, resulting in development of an internal boundary layer (IBL), sublayers bounded above by a discontinuity in some variable or state of the surface layer (Garratt 1992). IBLs result from horizontal advection of air across surfaces which vary in any quantity capable of affecting the physical properties of the atmosphere (e.g., temperature, humidity, or surface roughness). The following sections will discuss the two types of boundary layer transformations common to the coastal regions in sea and land breeze conditions.

a. Roughness Internal Boundary Layers

A roughness boundary layer develops when a sharp transition in surface features result in significant change in surface roughness that hence modifies the overlying wind field. This type of IBL develops downstream of the new surface feature with modified wind stress and mean wind profiles in a layer that grows in depth with fetch limit. Compared to the effects of changing surface roughness, the effects of surface heat flux or surface layer stability is secondary (Cheng and Castro 2002). Figure 1 is a schematic diagram which illustrates the concept of an IBL caused by a change in surface roughness.

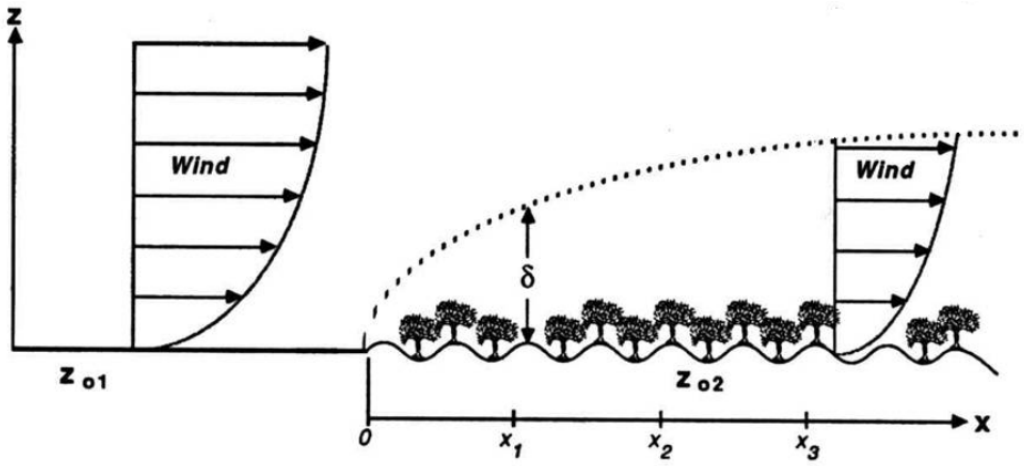

Figure 1. Diagram of an internal boundary layer (From Stull, 1988).

Several empirical methods have been developed to measure the height of a roughness IBL as it transitions from smooth to rough elements. Here, the height of the IBL, δ, is a function of fetch, the distance downstream from the point roughness changes. The IBL continues to grow in height with increasing distance from a surface change and modifies the vertical wind profile as it adjusts to the new surface. Above the IBL, flow is characteristic of the upwind surface while below it is affected by both the downstream and upstream roughness transition region (Benson 2005). In cases of extreme heterogeneity, multiple IBLs may be present, each responding to its corresponding local surface.

b. Thermal Internal Boundary Layer

A thermally-induced local circulation can produce a thermal internal boundary layer (TIBL), which creates potential surface fumigation of elevated pollutants. A common form of TIBL along coastal regions is the Convective TIBL. The Convective TIBL arises when air flows from a cooler to a warmer surface, inducing a steady-state mixed layer which deepens with distance from the shoreline. Figure 2 demonstrates the growth of a Convective TIBL as a function of distance downwind from a surface discontinuity.

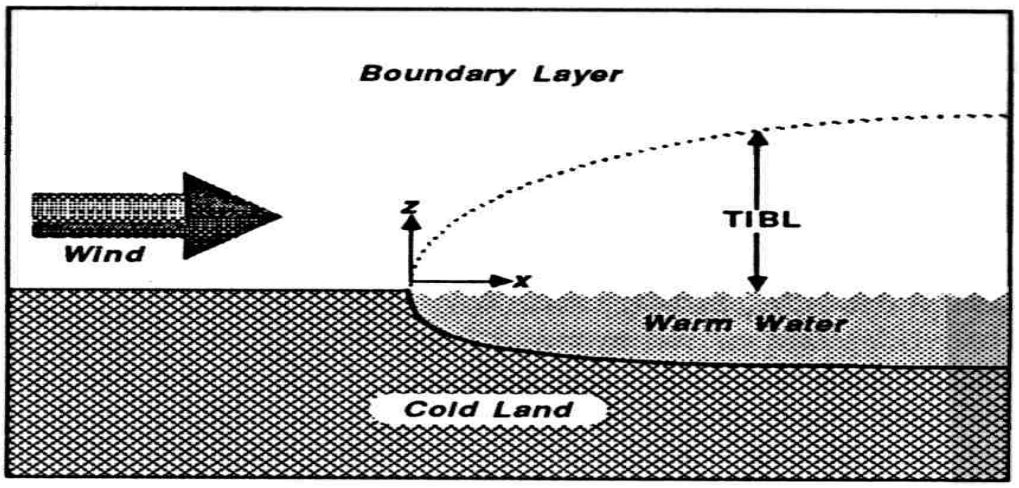

Figure 2. Growth of a convective TIBL (From Stull 1988).

C. MESOSCALE MODEL SIMULATIONS OF COASTAL CIRCULATIONS

Atmospheric motions occur on a broad spectrum of space and time scales. The term mesoscale meteorology refers to a spatial scale of atmospheric phenomena ranging in size from two to one thousand kilometers with a temporal scale greater than one hour but less than one day. Orlanski (1975) and Fujita (1986) provide additional detailed information regarding classes of mesoscale weather phenomena. In general, classification of mesoscale as the intermediate between micro and synoptic scales will suffice for this research purpose. Mesoscale phenomena are typically forced or supported by surface heterogeneity and fluctuations of energy across a defined boundary. Relevant forces affecting the mesoscale are pressure gradient force (including stability or buoyancy), Coriolis force, gravity, centrifugal forces and friction. These forces often change significantly across temporal and spatial scales consistent with mesoscale classification.

Mesoscale numerical weather prediction (NWP) typically involves forecasts for specific locations at precise times, such as a wind forecast for a military base at 0900 UTC. Mesoscale NWP models are in widespread operational use, but the technology still needs improvement through application and performance evaluations. The ability of a mesoscale model to numerically discretize weather phenomena is limited by the model's resolution (Kalnay 2003). That is, the smallest scales of motions which can be resolved are those with wavelengths greater than two grid sizes. Atmospheric processes occurring on scales less than a model's grid size are called "sub-grid" and must be parameterized. Despite advances in physical sciences and computation power, there will always remain important atmospheric processes and scales of motions too small for explicit resolution in atmospheric models. Critical evaluation of modeled sub-grid scale processes using fine resolution data is thus beneficial to improving forecast prediction.

Coastal thermal circulations are often subjected to mesoscale modeling studies due to their high frequency of occurrence, climatological impacts and critical role in convection, precipitation and pollution dispersion. Numerous observational and modeled studies of the coastal thermal circulation have yielded detailed understanding of these mesoscale weather phenomena. Despite this understanding, the ability to accurately interpret surface fluxes and roughness lengths and their interactions with complex coastal

regions and its overlying atmosphere remains unresolved. Numerical simulations of mesoscale phenomenon require solving the equations of motion for the conservation of mass, momentum, and energy. Model physics (e.g., surface processes, radiation, latent heating, and turbulent diffusion of heat, moisture, and momentum) and model dynamics (horizontal advection, vertical acceleration, Coriolis effects and time dependence) must be adequately resolved to obtain a realistic simulation (Avissar et al. 1990). Efforts continue to further understand mesoscale modeling limitations and this study is another step towards achieving that goal through use of a dense network of tower measurements.

D. PURPOSE AND OVERVIEW

This study presents data collected from a dense network of 36 towers and five Doppler wind profilers in the Weather Information Network Display System (WINDS) at Kennedy Space Center/Cape Canaveral Air Force Station, Florida (KSC/CCAFS) for the 2008 year. Two five-day periods (1–5 June and 18–22 June 2008) are evaluated for temporal and spatial variability between coastal thermal circulations and the physical properties of the surface. This research uses both objective and subjective analyses techniques to study the temporal evolution for analyzing time series, low-level wind circulations and vertical profiles of measured and calculated variables in conjunction with a high-resolution simulation from the U.S. Navy's Coupled Ocean-Atmosphere Mesoscale Prediction System (COAMPS^{TM}) model. The WINDS data was subjected to numerous quality-control measures to generate a coherent data set ideal for model evaluation. The overall goal of this extensive evaluation is to better understand the diurnal-dependent coastal thermal circulation leveraging a dense mesonetwork and assess the capability of stochastic boundary layer parameterization schemes (e.g., bulk aerodynamic formulations, atmospheric boundary layer parameterizations) commonly employed in high-resolution numerical simulations using various subjective and statistical methods

This chapter included a brief introduction of terminology, concepts and thermodynamics of the lower atmosphere useful in this study. Chapter II provides an overview of recent high-resolution simulations related to sea breezes, some fundamental

theories of surface flux calculations and how these fluxes are parameterized in COAMPS^{TM}. Chapter III describes the method of observed and simulated data collection and processing, and the meteorological characteristics of the region for the presented cases. Chapter IV details results and analyses from observations. Chapter V presents a direct comparison and statistical evaluation of observed sea breezes to numerical model output and Chapter VI summarizes key results and concludes the thesis with recommendations for future research.

E. MILITARY APPLICATIONS

The modern military operates in various terrains and surface types, often in regions where weather observations are sparse. The development and implementation of high-resolution numerical models have aided the military weather community mission to enhance operational safety while exploiting the weather for mission success. Communication via electromagnetic and electro-optical wave propagation, low level aviation, and target acquisition and engagement, are all examples of military operations directly affected by weather conditions on the sub-grid scale and in the near-surface environment. Critical evaluation and verification of modeled sub-grid scale weather phenomena (i.e., surface moisture and heat flux) with fine resolution data is important to improving forecast prediction and mitigating potential loss of life and property.

THIS PAGE INTENTIONALLY LEFT BLANK

II. BACKGROUND INFORMATION

A. COASTAL THERMAL CIRCULATIONS

Beginning shortly after sunrise (~0700 local time) and mixing out of a residual stable nocturnal boundary layer, near surface air parcels slowly begin to rise over the gradually warmer land surfaces. As a result of mass conservation, cooler air from the water flows in at the low levels to replace the ascending parcels and results in the well-known sea breeze circulation. The thermodynamic discontinuity of cooler temperature, low level convergence and slight increase in specific humidity mark the SBF leading edge. Land breezes are forced by differential cooling between the land and water, typically weaker than sea breezes in velocity and depth, and result in clear skies and light offshore surface flow. The speed and direction by which these mesoscale boundaries propagate are sensitive to surface characteristics such as coastline shape, roughness length and moisture.

The coastal circulation life cycle owes its existence to a dependence on many geophysical variables that include the surface sensible heat flux (*SHF*, which determines the coastal temperature difference), ambient geostrophic wind (V_g), atmospheric thermal stability (N), atmospheric moisture (q), water body dimension (d), terrain height (h_t), terrain slope (s), Coriolis parameter (f), surface roughness length (z_o), and shoreline curvature (r). Four of these variables (*SHF*, V_g, N, and q) vary significantly over time at a given location as a function of season. The remaining variables (d, h_t, s, f, z_o, and r) are largely temporally constant at a given location. Since the region of east-central Florida is relatively flat and level, the contributions from h_t and s are negligible in this area.

The effects of geophysical forcing are characterized in terms of four widely used measures of thermally-direct circulation intensity: horizontal (l) and vertical (h) length scales and cross-shore horizontal (u) and vertical (w) wind speeds. Figure 4 portrays the typical magnitude of these quantities within a typical diurnally-driven coastal circulation.

A brief summary of historical advancements in understanding how these geophysical variables influence all aspects of the mesoscale coastal circulation is given below (adapted from Crosman and Horel 2010).

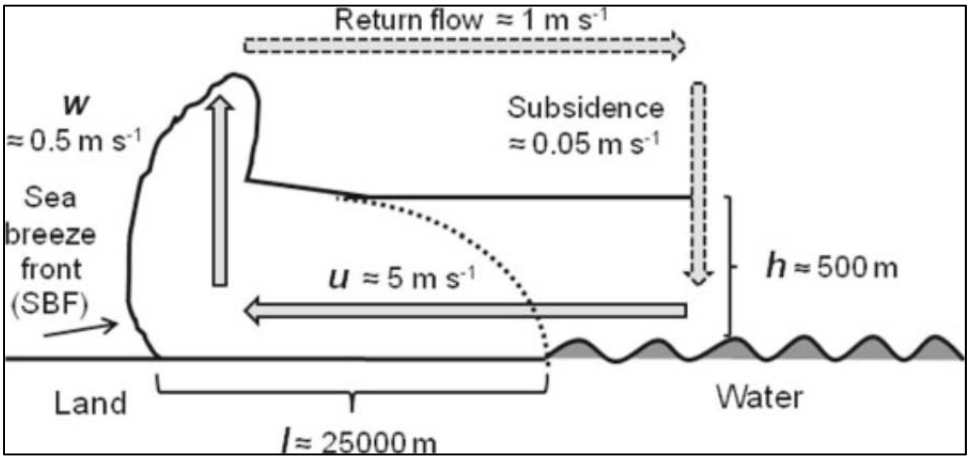

Figure 3. Characteristics of sea breeze horizontal (l) and vertical (h) length scales and horizontal (u) and vertical (w) speed (From Crosman and Horel 2010)

1. Factors Affecting Sea Breeze Circulations from Previous Simulations

The first simulation of a sea breeze circulation by Pearce (1955) included an unsophisticated two-dimensional coordinate system and linearized equations which neglected moisture, latent heating, radiation, and coastal parameterizations. Since his pioneering work nearly seventy years ago, advancements in computational speed, increasingly sophisticated surface layer parameterization schemes and better scientific understanding of boundary layer processes have signaled an increase in three-dimensional simulations of the sea breeze circulation. Through the early 1980s, most studies used two-dimensional hydrostatic models with horizontal grid spacing between 2–15 km, assumed constant flux and treated surface layer turbulence using simple K-theory. Today, Monin-Obukhov similarity theory has replaced simple K-theory to derive surface layer fluxes and three-dimensional, non-hydrostatic model simulations with finer grid resolutions accurately detail coastal thermal circulations. Previous studies have revealed a strong dependence of sea breeze intensity, inland penetration and speed on many physical processes described next.

a. Sensible Heat Flux (SHF)

Differential daytime sensible heating between land and water surfaces results in a horizontal temperature gradient along the coast. This gradient is the main mechanism which drives sea breeze circulations. Numerous studies correlating SHF to sea breeze (Miao et al 2003; Ogawa 2003) intensity prove higher values lead to greater l and u. This relationship coincides with dependence on the size of the heated land surface (Xian and Pielke 1991; Savijarvi and Matthews 2004). Recent findings conclude that as the spatial extent of heating increases, sea breezes tend to become stronger (i.e., smaller strips of land have weaker sea breezes than their larger counterparts.) In the absence of background flow, a coastal circulation is solely a boundary layer problem.

b. Ambient Geostrophic Wind (V_g)

Dependence of sea breeze intensity on synoptic scale flow is an active area of extensive research. In past studies, researchers simplify the background flow by separating into shore-perpendicular (onshore/offshore) and shore-parallel components. Generally, a SBF can be significantly enhanced (weakened) by offshore (onshore) geostrophic winds leading to frontogenesis (frontolysis). Critical values by which these processes enhance/decay a coastal circulation are an area of scientific debate. However, consensus agrees that offshore $V_g > 6$ ms^{-1} and onshore $V_g > 3$ ms^{-1} will impede sea breeze development (Zhong and Takle 1993; Porson et al. 2007). Background flows in between are contributory to intensified l, h and u.

c. Thermal Stability (N)

Thermal stability is represented by the Brunt-Väisälä number (N). Most numerical studies agree on two principles: (1) a weakly stably-stratified atmosphere provides a more favorable environment for sea breezes than a strongly stable-stratified atmosphere, which acts to damp a circulation and (2) diurnal differences in stability are the fundamental reason why nighttime land breezes are weaker than daytime sea breezes (Xian and Pielke 1991). Essentially, an inverse relationship exists between N and h in which increasing stability acts to decrease a sea breeze vertical extent. Disagreement remains about strength of near-surface stable layers and their effects on SBF intensity.

d. Moisture (q)

The influence of atmospheric moisture on sea breeze development has not been thoroughly explored. Baker (2001) explored the rapid moistening of a sea breeze circulation from surface evaporation of soil moisture and found significant modulation of moist convection along the sea breeze front. Basically, increased moisture flux to the immediate atmosphere bolstered convective initiation which vertically stretches a SBF. The residual cloud cover reduces the amount of incoming solar radiation reaching the land surface which relaxes the thermal gradient (Segal et al. 1986).

e. Water Body Dimension (d)

Due to the complex non-linear system of equations required to account for an infinite variation of shoreline features, researchers typically use a general circular or slab-symmetric perpendicular shoreline on a single-dimension to calculate. Abbs (1986) argues that water body dimensions play an important factor for sea breezes associated with semi-enclosed bays and lagoons, which provide an added complication of interactions between the bay breeze and the large scale sea breeze circulation. Zhong and Takle (1992) found extremely complex wind patterns over KSC/CCAFS associated with Merritt Island and multiple river breezes. The varied surface interactions created divergence near river breezes which combined with a westward moving sea breeze circulation to produce an area of enhanced convergence over Merritt Island. They conclude that an overlying boundary layer above a small gulf (d = 5–50 km) is likely to influence ambient land boundary layers competing for limited cool, moist, low level air.

f. Shoreline Curvature (r)

Shoreline curvature (r) strongly influences interactions between prevailing winds and sea breezes. A convex coastline yields convergence of the onshore low-level flow and strengthens the overall circulation, while concave coastlines weaken the circulation through divergence (Gilliam et al. 2004). Baker (2001) noted that shoreline curvature had a major impact on location and timing of sea breeze initiated precipitation.

g. Coriolis Force (f)

The Coriolis force is typically specified by magnitude of the Coriolis parameter, *f*, at fixed latitude, influences wind direction and *l*, *u*, and *h*. Numerical studies provide evidence of *f* on the latter stages of a sea breeze life cycle as it acts to rotate the sea breeze clockwise 360° over a 24-hour period (Zhong and Takle 1992). Coriolis effects are generally small initially when friction and SHF dominate. Six hours after sea breeze onset the wind pattern begins to rotate right and weaken. The effects of *f* are modulated by surface friction (u_*) and sea breeze strength and interact with shoreline curvature to determine areas of enhanced sea breeze-induced convergence (Boybeyi and Raman 1992).

h. Roughness Length (z_0)

Roughness length is a function of surface characteristics and is defined as the height at which mean wind and turbulent flux vanish. The effect of roughness is normally referred to as frictional effects, which act to destroy developing horizontal pressure gradients associated with sea breezes (Anthes 1978). Recent modeling efforts by Couralt (2007) showed that roughness length regulates *h* while work by Boybedi and Raman (1992) found that increasing the roughness length resulted in an enhanced circulation with larger vertical transport of heat. Ellis (2010) found that advective influence of roughness lengths from an upstream surface had a major impact on surface wind speeds and moisture advection. Careful consideration of roughness lengths in a coastal zone is critical since z_0 can range from 10^{-5} m over calm seas to 10^{-1} m over grassland to 1–100 m for cities, forests and mountainous terrain.

2. Previous Studies of Coastal Circulation over KSC/CCAFS

Occurring at any time of the year, but most prevalent throughout the warm season, differential heating of land and water surfaces near KSC/CCAFS gives rise to diurnally cycling coastal winds, commonly referred to as sea breezes during the daytime and land breezes at night, where the SBF defines a discontinuity by a slight decrease in temperature, a sharp increase in humidity and spike in wind speed. During periods of

relatively weak synoptic forcing, the afternoon SBF may travel several hundred kilometers inland from both sides of the Florida Peninsula and merge to trigger numerous showers and thunderstorms over the Peninsula. Several studies of coastal thermal circulations at KSC/CCAFS have been conducted using Doppler radar and cloud photogrammetry (Wakimoto and Atkins 1993), observations (Reed 1979), aircraft soundings (Laird et al. 1995), and with high-resolution mesoscale modeling (Rao and Fuelberg 2000), (Manobianco et al. 1996), and (Baker et al. 2000). In particular, Reed (1979) demonstrated from observations at Tower 0313 that a discernible diurnal oscillation between onshore and offshore wind components was present year-round, with the largest amplitude occurring in May and the smallest in January. Reed also found the largest amplitudes were observed by the highest anemometer and the circulation shifted clockwise (veered) with time, roughly completing a 360° rotation in one day. Zhong and Takle (1992) studied this coastal circulation and intricate wind field generated by differential heating of land and water in this region. Their research details the evolution of divergent and convergent flows associated with friction, turbulence and exchange of energy flux between land, sea and river breezes. Rao and Fuelberg (1999) investigated interactions between diurnally-driven wind fields and Horizontal Convective Rolls (HCRs) and Kelvin-Helmholtz Instability (KHI). They used a high-resolution simulation to produce enhanced vertical motions along an advancing Indian River Breeze (IRB) ahead of the SBF. Their work demonstrated the complex scale of interactions between land-water circulations and other perturbations (e.g., HCRs, KHIs). They also confirmed the KSC/CCAFS SBF's vertical scale to reach 750–1000 m in height. Case et al (2003) performed a detailed land breeze study utilizing the KSC/CCAFS mesonetwork. Their research found the depth and wind speed of nighttime land breezes were directly related to the presence and intensity of daytime sea breezes. The deepest land breezes (>150 m depth) were most often preceded by an afternoon sea breeze, had smaller nocturnal horizontal temperature gradients, and experienced a mean onset time four hours earlier than shallower land breezes.

Despite extensive previous attempts to observe and simulate coastal circulations occurring in this region, details of these diurnally driven coastal circulations are often

poorly resolved due to extensive temporal and sub-grid spatial scale variability. Numerical simulations from mesoscale models have not been thoroughly evaluated to include turbulent fluxes and spatial variability. The coastal thermal circulation over KSC/CCAFS is chosen for this study to take advantage of a dense network of meteorological sensors for a more complete mesoscale model evaluation.

B. SURFACE LAYER AND SURFACE FLUX CALCULATION

The most important concept in surface layer meteorology is perhaps the flux, which is the transport of a variable per unit area per unit time (Stull 1988). Turbulence fluxes at the surface represent the exchange of momentum or heat, and any scalars between the atmosphere and the underlying surface. Often, surface fluxes are expressed in terms of * quantities discussed next. For momentum flux, it is represented by the *friction velocity*, denoted by u_*. The relationship between the two quantities is given by:

$$u_*^2 = \sqrt{\overline{u'w'}^2 + \overline{v'w'}^2} \tag{1}$$

where u', v', and w' are the perturbed horizontal and vertical components of air velocity. For simplicity, ABL meteorologists typically orient their coordinate axes such that the abscissa corresponds to the direction the wind stress is applied (Stull 1988). In this case, one horizontal perturbation dimension is eliminated, and (1) reduces to

$$u_* = \left|\sqrt{\overline{u'w'}}\right| \tag{2}$$

Similarly, scaling parameters for surface-layer virtual potential temperature (θ_{v*}) and water vapor (q_*) were defined that are directly related to surface layer heat and water vapor fluxes:

$$\theta_{v*} = -\frac{\overline{w'\theta_v'}}{u_*} \tag{3}$$

$$q_* = -\frac{\overline{w'q'}}{u_*} \tag{4}$$

These * quantities can be regarded as the magnitude of the turbulence perturbations in the surface layer.

Possibly the most important diagnosis of the ABL that must be undertaken when characterizing turbulence potential is that of its *static stability*. Meteorologists classify a layer's static stability as stable, unstable, or neutral which can be represented by a number of variables such as temperature gradient or Richardson number. Static stability in the boundary layer is usually related to the direction of surface heat flux transport, although other processes may contribute to boundary layer thermal stability.

Surface layer flux-profile relationships were developed based on Monin-Obukhov (M-O) similarity and field measurements and describe how the surface mean variables are related to flux quantities. In similarity theory, diagnostic relationships between dimensionless quantities are drawn using extensive observational and experimental data. The resultant equations are frequently used to obtain values of mean wind, temperature, moisture and other scalars as a function of height when the surface fluxes are known. On the other hand, surface fluxes can also be obtained based on measurements of the mean surface layer quantities. For a thorough treatment of similarity techniques, the reader is referred to Stull (1988) and Kaimal and Finnigan (1994).

A key parameter in M-O similarity theory is the Monin-Obukhov length (*L)* defined as:

$$L = -\frac{u_*^3}{\kappa \frac{g}{\theta_v} \overline{w'\theta_v'}} \tag{5}$$

where κ is the von Karman constant (normal taken with a values of 0.35); u_*, friction velocity; g is gravity; θ_v is virtual potential temperature; and $\overline{w'\theta_v'}$, the vertical turbulent heat flux. The M-O length is commonly leveraged as a stability indicator because its inclusion of the vertical turbulent heat flux term, which undergoes a sign change when static stability changes. If the surface layer $\overline{w'\theta_v'} < 0$, then $L > 0$ and the layer is considered stable thermal stratification. Conversely, if $\overline{w'\theta_v'} > 0$ then $L < 0$ and the layer is

considered thermally unstable. If $\overline{w'\theta_v'}$ = 0, then L approaches infinity and the layer is statically neutral. It is important to recognize, however, the flux-profile relationship based on M-O similarity and the empirical relationship from field measurements are based on assumptions of horizontal homogeneity. Caution is needed to apply the flux-profile relationship to IBLs and other heterogeneous surfaces.

Work by Businger (1971) and Dyer (1974) produced empirical forms of flux-profile relationships for momentum, heat and specific humidity based on measurements from the 1968 Kansas experiment. These widely accepted non-dimensional functions complete the flux-profile relationship with the functional form:

$$\frac{\kappa z}{u_*}\frac{\partial \overline{u}}{\partial z} = \phi_m\left(\frac{z}{L}\right) \tag{6}$$

$$\frac{\kappa z}{\theta_{v*}}\frac{\partial \overline{\theta_v}}{\partial z} = \phi_h\left(\frac{z}{L}\right) \tag{7}$$

$$\frac{\kappa z}{q_*}\frac{\partial \overline{q}}{\partial z} = \phi_q\left(\frac{z}{L}\right) \tag{8}$$

with the subscript *m, h, q* to indicate momentum, heat and specific humidity, respectively. Here ϕ_m, ϕ_h and ϕ_q are given as:

$$\phi_m\left(\frac{z}{L}\right) = \begin{cases} \left[1-\left(\frac{15z}{L}\right)\right]^{-1/4} & \text{for } \frac{z}{L} < 0 \text{ (unstable)} \\ 1 \text{ for} \frac{z}{L} = 0 \text{ (neutral)} \\ 1+\left(\frac{4.7z}{L}\right) & \text{for} \frac{z}{L} > 0 \text{ (stable)} \end{cases} \tag{9}$$

$$\phi_{h,q}\left(\frac{z}{L}\right)=\begin{Bmatrix} 0.74\left[1-\left(\frac{9z}{L}\right)\right]^{-1/2} \text{ for } \frac{z}{L}<0 \text{ (unstable)} \\ 0.74 \text{ for} \frac{z}{L}=0 \text{ (neutral)} \\ 0.74+\left(\frac{4.7z}{L}\right) \text{ for} \frac{z}{L}>0 \text{ (stable)} \end{Bmatrix} \tag{10}$$

If measurements of the mean wind and temperature are available at two levels z_1 and z_2, equations (6)-(8) are integrated using these limits to obtain:

$$u_* = \frac{\kappa\left[\bar{u}(z_2)-\bar{u}(z_1)\right]}{\int_{z_1}^{z_2}\phi_m\left(\frac{z}{L}\right)d\ln z} \tag{11}$$

$$q_* = \frac{\kappa\left[\bar{q}(z_2)-\bar{q}(z_1)\right]}{\int_{z_1}^{z_2}\phi_q\left(\frac{z}{L}\right)d\ln z} \tag{12}$$

$$\theta_{v*} = \frac{\kappa\left[\overline{\theta_v}(z_2)-\overline{\theta_v}(z_1)\right]}{\int_{z_1}^{z_2}\phi_h\left(\frac{z}{L}\right)d\ln z} \tag{13}$$

These integrals are in closed form but must be solved iteratively to obtain q_*, θ_{v_*} or u_* since the integrand involves L which includes these unknowns. For deriving these values to a practical estimate, a few iterations converged to suitable precision. The methods described above are used in this thesis to derive surface fluxes from 17 towers hosting two levels of measurements.

C. SURFACE FLUX PARAMETERIZATION IN MESOSCALE MODELS

Early research in simulating surface fluxes in general circulation models (GCMs) mainly focused on parameterizing bulk exchanges of mass, momentum, and energy between homogeneous surfaces and the ABL. The resolution of early GCMs was on the order of tens to hundreds of kilometers, and crudely dealt with fluxes, friction and surface

roughness heterogeneities at the sub-grid scale. Louis (1979) devised a parameterization scheme for turbulent fluxes that included static stability effects and evaluated its performance in a 10-day forecast model. Wang et al. (2002) suggested adaptations to Louis's approach to better characterize fluxes over smooth surfaces and in cases where momentum and heat fluxes differ due to varying stability.

Two methods are commonly used to account for sub-grid scale surface heterogeneity in GCMs. The technique of parameter aggregation uses the fractional coverage of different surface types within a grid box to obtain grid-averaged parameters and then incorporates the sub-grid averages into the bulk flux parameterization for the larger grid. The flux aggregation method uses bulk parameterization to obtain fluxes for each surface type and then determines grid-averaged fluxes based on the fractional coverage of each surface type within a grid box. At higher resolution, aggregation of fluxes or parameters within a model grid box becomes less of a concern than the advection of these variables from neighboring grid boxes, particularly when surface heterogeneities are at least as large as the model resolution (Ellis 2010).

One of today's greatest challenges to mesoscale numerical weather prediction (NWP) is determination of a model spatial and temporal resolution sufficient to capture local (~ 1 km) phenomenon yet computationally inexpensive enough to run on a timely routine cycle in support of operational forecasters. Despite advancements in supercomputing power and the ability to quickly discretize numerical solutions at finer spatial and temporal scales, there are several important atmosphere processes which cannot be explicitly resolved. A few examples are turbulence, friction, radiation, evaporation and condensation. These processes play a critical role in the global energy budget and cannot simply be ignored without severely degrading the model forecast quality. To account for these sub-grid processes, modelers usually parameterize their net effect at the resolution of the model. Researchers have developed numerous schemes for parameterizing sub-grid scale processes in the atmosphere, and this is an area of ongoing research. Ideally, as our understanding of these ABL processes continues to improve, so will our skill in accurately simulating these processes in numerical models.

1. Bulk Aerodynamic Parameterizations

In general, most numerical models incorporate the transfer of surface fluxes using a bulk or drag method. In this concept, surface wind is assumed zero (which fails in calm wind conditions). Thus, modelers must use frictional velocity to describe the drag of the atmosphere against an underlying surface.

$$C_D = \left(\frac{u_*}{\overline{U_{10}}} \right)^2 \tag{14}$$

The drag coefficient C_D is a generic bulk transfer coefficient 10 m above the surface. Substituting Equation (1), the turbulent surface fluxes become:

$$\overline{w'\theta'} = -C_H \overline{U}_{10} \left(\overline{\theta}_{10} - \overline{\theta}_0 \right) \tag{15}$$

$$\overline{w'q'} = -C_H \overline{U}_{10} \left(\overline{q}_{10} - \overline{q}_0 \right) \tag{16}$$

$$\overline{u'w'} = -C_D \overline{U}_{10}^2 \tag{17}$$

Equations (15-17) are called the aerodynamic formulae. It shows the relationship between fluxes and the mean wind, temperature and specific humidity at *z*-height (WMO standard is 10 m above ground level) and ground level ($z = 0$). Knowledge of these mean values and drag coefficients allows ABL meteorologists to derive surface fluxes.

COAMPS^{TM} utilizes a surface layer parameterization following Louis (1979) scheme, which uses the bulk Richardson number to directly compute surface sensible heat flux, surface latent heat flux and surface drag. The bulk Richardson number is defined as:

$$Ri_B = \frac{gz\Delta T}{u^2 \theta} \tag{18}$$

where *g* is acceleration due to gravity, *z* is the reference elevation (10 m in COAMPS^{TM}), ΔT is the air-sea temperature difference, *u* is the wind speed at *z*, and θ is the mean potential temperature over the depth of the surface layer.

Surface momentum and heat fluxes are obtained directly from bulk Richardson formulation (with similar expressions for latent heat flux) using:

$$C_D^2 = a^2 F_M\left(\frac{z}{z_0}, Ri_B\right) \tag{19}$$

$$C_H^2 = \frac{a^2}{R} F_H\left(\frac{z}{z_0}, Ri_B\right) \tag{20}$$

$$a = \frac{\kappa}{\left(\ln\left(z/z_0\right)\right)} \tag{21}$$

The term a is the neutral drag coefficient, z_0 is the surface roughness and R is the transfer coefficient ratio for heat to momentum (0.74).

2. Roughness Length in Numerical Models

Successful prediction of the near-surface wind field in NWP models is contingent upon accurately parameterizing roughness elements. Considering that surface characteristics determine variation of momentum, heat and moisture fluxes into the overlying atmosphere, it is fair to say that accurate parameterization of surface roughness improves model performance throughout the entire atmosphere. Roughness length over land is typically averaged over some finite portion of the model domain using a reference table. For open ocean, roughness is calculated using Charnock (1955) formulation:

$$z_0 = \alpha \frac{u_*^2}{g} \tag{22}$$

which relates surface wind stress over an open ocean to wave-induced roughness. As wind stress increases, waves grow higher and roughness length increases. In Equation (22), g is gravity and α, known as the Charnock parameter, is typically valued at 0.0144 for flat open seas.

In regions of sharply contrasting surface characteristics, roughness length varies markedly with possible sharp transitions at small spatial scale, which introduces uncertainty in defining a grid-averaged roughness length in mesoscale models. Moreover,

roughness length over land surfaces in mesoscale models are considered constants, while the local boundary layer maybe affected by upwind boundary layers with significantly different roughness. Consequently, roughness heights in regions of extreme heterogeneity may be wind-direction dependent (Ellis 2010). Figure 4 shows the difference between grid averaged surface roughness height in COAMPS^{TM} and those calculated from 17 towers in the WINDS network. Here, calculated surface roughness near the coast can differ up to 0.3 m. It has been suggested (Jacobs and Maat 2005) that a primary source of 10 m wind forecast error is the difference between actual surface roughness and that used in a model's parameterization scheme.

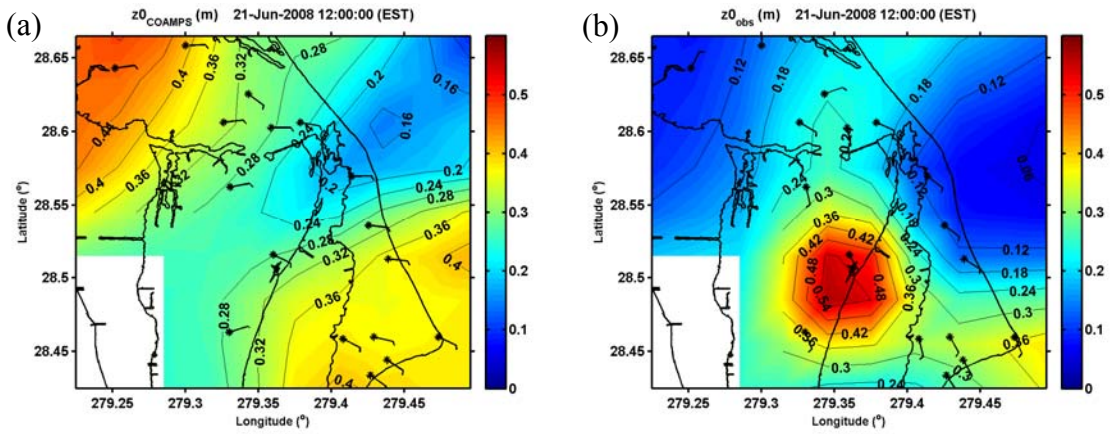

Figure 4. Contour plots of roughness length from (a) COAMPS^{TM} and (b) calculated z_0 from WINDS at 1200 EST on 21 June 2008.

III. DATA PROCESSING AND SELECTED CASES

A. LOWER TROPOSPHERE OBSERVATIONS

Observation data for this research was made from the 1200 km^2 meteorological observation network (Figure 5) in the region surrounding KSC/CCAFS. This mesonetwork is jointly operated by CCAFS and the National Aeronautics and Space Administration (NASA) Headquarters Weather Support Office. The primary mission of WINDS is to provide the 45th Weather Squadron, CCAFS, NASA Safety, and Range Safety personnel with a comprehensive, real-time description of weather conditions in support of the KSC spaceflight mission (Computer Sciences Raytheon [CSR] 2006). Measurements from this network or its previous settings were used in several studies on various topics (Case et al. 2004; Bauman 2008). More recently, Ellis (2010) used the same dataset to study the variability of surface roughness. Detailed descriptions of the KSC/CCAFS mesonetwork can be found in the above mentioned references. A brief description is given next.

1. Weather Information Network Display System (WINDS)

WINDS collects and disseminates continuous observations measured by a suite of over 200 wind, temperature, humidity, and pressure sensors attached to 44 instrumented towers from the surface to 150 m. This study utilizes observations recorded at 5-minute intervals from 36 WINDS towers. As shown in Figure 5, WINDS towers at CCAFS are classified into three categories based on their primary operational function: launch critical, safety critical, and forecast critical towers. The four-digit tower identification number is decoded (except for Towers 9001 and 9404) as follows: the first pair of digits is the tower's distance from the outer coastline, and the second pair of digits is its latitudinal distance from Port Canaveral. Both coded distances are rounded to the nearest integer in nautical miles. The Appendix contains tables of tower locations and instrumentation heights by tower type. For extensive information regarding data collection and tower information, reader is referred to Ellis (2010).

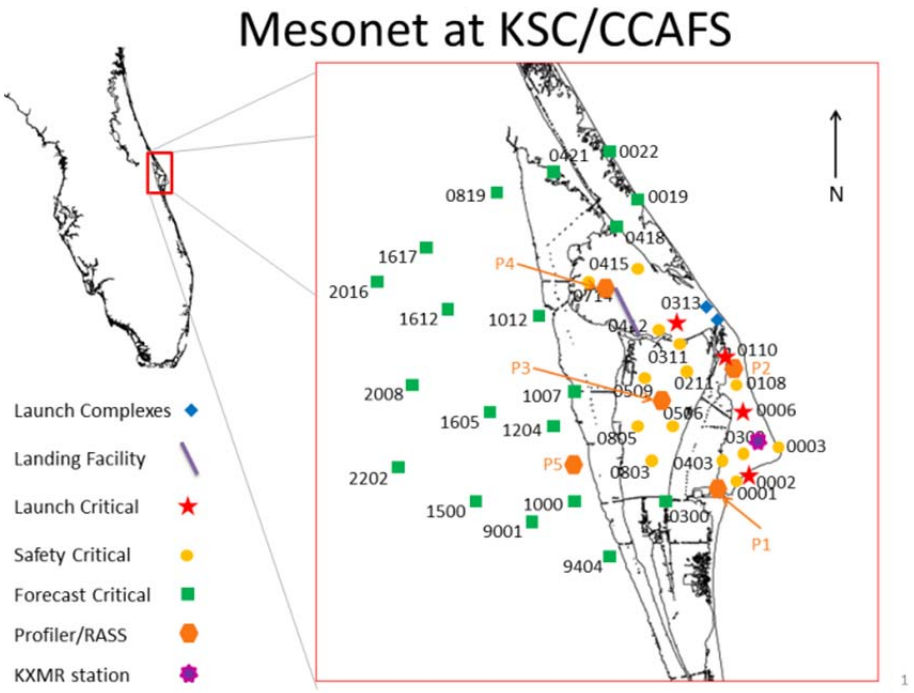

Figure 5. Meteorological instrumentation distribution on KSC/CCAFS (From Wang, 2011).

Although the WINDS network does not provide high-rate turbulence measurements using fast response sensors, it probably provides the largest amount of multilevel measurements within a limited area. Use of the data allows examination of boundary layer processes on fine spatial and temporal scales. Use of the data for model evaluation also reveals new insights into model deficiencies based on distance from the Atlantic Ocean coastline.

2. Doppler Radar Wind Profilers (DRWP)

In addition to the expansive WINDS tower observations, KSC/CCAFS maintains a network of five 915 MHz Doppler Radar Wind Profilers (DRWP) with Radio Acoustic Sounding Systems (RASS). This network provides three-dimensional wind direction and speed estimates in the lower atmosphere from 120–4000 m AGL. The current settings disseminate an averaged observation every 15 minutes with wind speed and direction profiles accurate to within 2 knots and 10°. Locations of the DWRPs are arranged in a diamond-shape configuration enclosing the shuttle launch facility (orange hexagon in

Figure 5). With an average spacing of 10–15 km, these profilers deliver high spatial and temporal resolution wind data above the height of WINDS sensors. For the purpose of this thesis, the DRWP network is used to measure the coastal circulation's vertical extent.

3. Past Studies using KSC/CCAFS Mesonetwork

Numerous studies have been conducted to exploit the abundant meteorological data available in this dense region. Neumann (1971) used tower data to diagnose sea breeze-induced convection. His work narrowed the forecasting challenge to one of an accurate low level wind field prediction. Reed (1979) evaluated the low level wind field from a few towers and was able to identify temporal characteristics of the sea and land breezes. Zhong and Takle (1992) used the complete WINDS dataset to determine the boundary layer's general features and seasonal dependence. Their work was limited to a single level of measurements and hence, were unable to adequately resolve surface layer fluxes. Case and Manobianco (2004) leveraged the dense mesonetwork to test an objective technique for mesoscale model verification. Their focus was solely on model verification of mean variables such as temperature, wind and humidity and did not evaluate surface layer evolution during a phenomena-based event.

Our study examines KSC/CCAFS mesonetwork data for specific characteristics and modifications to the surface layer during ten coastal circulation events. Our focus is the mean variables and derived fluxes from COAMPS^{TM} and KSC/CCAFS mesonetwork. In addition, to take advantage of the densely distributed tower network, we further evaluated how the model bias and error are distributed in the region, which provides a sense of spatial distribution of the model error.

B. DATA ORGANIZATION AND QUALITY CONTROL

For this study, original data in 5-minute intervals were provided with the following precisions: air temperature and dew point, 0.1ºF; surface pressure (Tower 0313 only), 0.1 hPa; wind speed, 1 knot; and wind direction, 1°. Prior to using these observations to derive roughness length, momentum and heat fluxes, the data were converted to corresponding SI units and subjected to quality control algorithms that excluded all missing, illogical (decreasing time) and erroneous (-1000 gkg^{-1} humidity)

data. Due to the relative coarse precision of wind speed measurements, observations taken when speed differences between the two levels did not exceed 1 knot (about 0.5 ms^{-1}) were excluded from roughness length and flux calculations. In this thesis, the term 'mean' quantities refers to potential temperature, specific humidity and wind while 'flux' quantities refers to sensible heat flux (SHF), latent heat flux (LHF) and momentum flux (MFL).

Several of the multilevel towers house duplicate sensors on opposite sides of the tower, usually northwest and southeast sides. For wind data, MATLAB was used to merge upwind side observations only to alleviate corrupted downwind measurements due to the flow distortion of the tower structure. This additional discriminate action assures minimal influence from the tower structure itself onto variables of interest. The observations were reordered and organized into a coherent dataset suitable for model evaluation. Calculations of kinematic fluxes are dependent on availability of multilevel measurements of temperature, moisture and wind. The Appendix lists 17 WINDS towers housing necessary multilevel instrumentation for calculating fluxes in this research.

Finally, MATLAB was employed to composite all coherent data from all towers together with common level measurements in a two-dimensional matrix for analyzing coastal circulations. The common levels are 16.5 m for wind data, 1.8 m for temperature and relative humidity. Compositing all measurements of the same variable from different towers into a logical dataset permitted visualization of spatial variability relative to the surface features such as the coastline. Figure 6 shows an example of such variability in potential temperature distribution during a SBF passage using WINDS towers. Similar plots can be produced for other variables including fluxes calculated from the 17 towers.

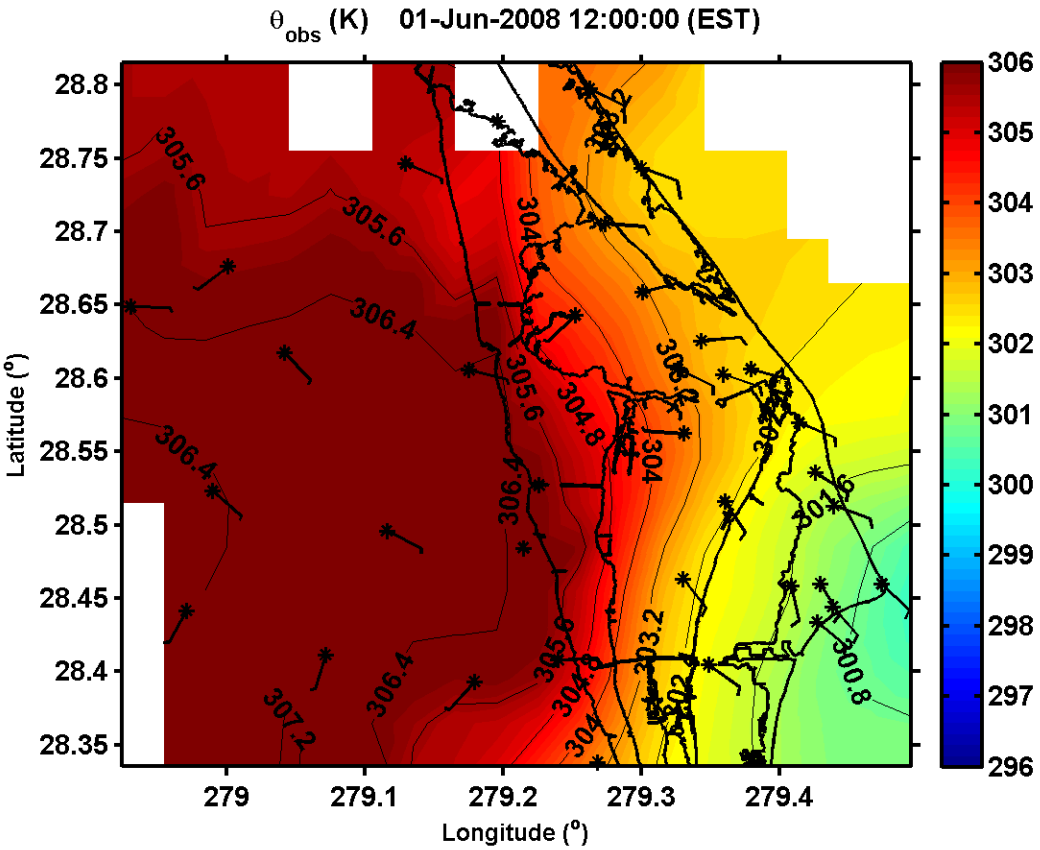

Figure 6. Contour plot of potential temperature measured at 1.8 m at 1200 EST on 1 June 2008. A SBF is clearly seen in this figure in the region of dense isotherms.

C. COAMPS™ MODEL SIMULATION

Meteorological analysis and forecast simulations were conducted with COAMPS™ version 4.2.2. COAMPS™ was run from cold start in simulation mode similar to the current operational forecast model (30 levels), on four nested grids with a horizontal grid spacing of 27, 9, 3, and 1 km as depicted in Figure 7. COAMPS™ obtains terrain characteristics from high-resolution databases maintained by the U.S. Geological Survey. Physical parameterization schemes including a subgrid mixing scheme following (Deardorff 1980), a (Mellor-Yamada 1982) type 1.5 turbulence closure, an explicit moisture physics package (Rutledge and Hobbs 1983), a modified cumulus convective processes (Kain and Fritsch 1993) and complex radiation bundle (Harshvardan et al. 1987).

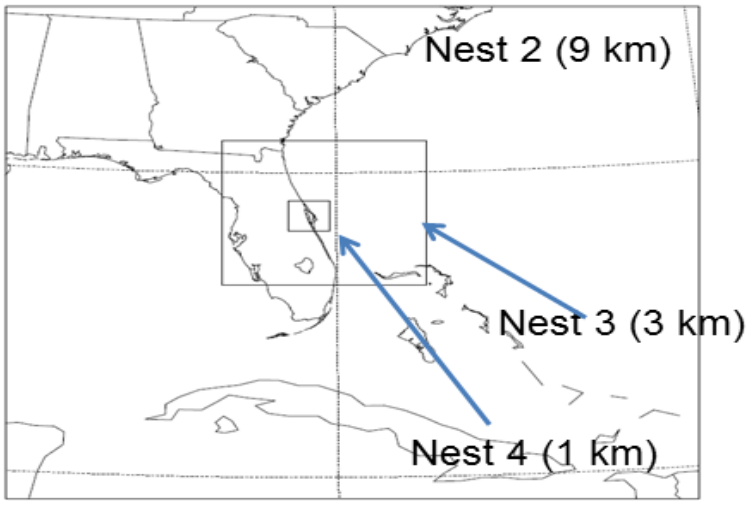

Figure 7. COAMPS^{TM} model nested boundaries for simulations in this study.

COAMPS^{TM} simulations were made twice daily at 0000 and 1200 UTC with data assimilation using conventional data and the global NOGAPS analysis as boundary conditions. Each forecast was run for 48 hours with a twelve hour data assimilation cycle. None of the WINDS data from KSC/CCAFS were assimilated in the COAMPS^{TM} simulations. Therefore the comparisons between the model and the WINDS observations are truly independent and the mesoscale and boundary layer structure in the simulation relies mostly on the model physics and large scale forcing. These features are typically under-resolved using standard assimilated observations, including data sets used in the operational model such as surface observations, coastal buoys, rawinsondes, and satellite data. The final analyzed forecast package used is a composite of multiple forecast runs between hour six and hour seventeen. This period of forecast is considered optimal with minimum effects from initial spin up or error due to extended forecast time.

The COAMPS^{TM} output is analyzed using MATLAB from the hybrid sigma height coordinate and interpolated to the nearest WINDS tower height. For temperature and humidity, output was interpolated to 1.8 m height. For wind speed and direction, the output was interpolated to 16.5 m height. Both levels were chosen to match the largest abundance of measured variables following the Appendix. Figure 8 illustrates a simulated sea breeze frontal passage using COAMPS^{TM} interpolated potential temperature at 1.8 m height level. The results shown here match the same time frame as Figure 6. Compared to

the observed SBF location, the COAMPS™ simulations produced SBF is further inland, signaling an earlier predicted SBF onset. It is also seen that the COAMPS™ potential temperature is significantly lower than observations. These model discrepancies will be thoroughly discussed in Chapter V.

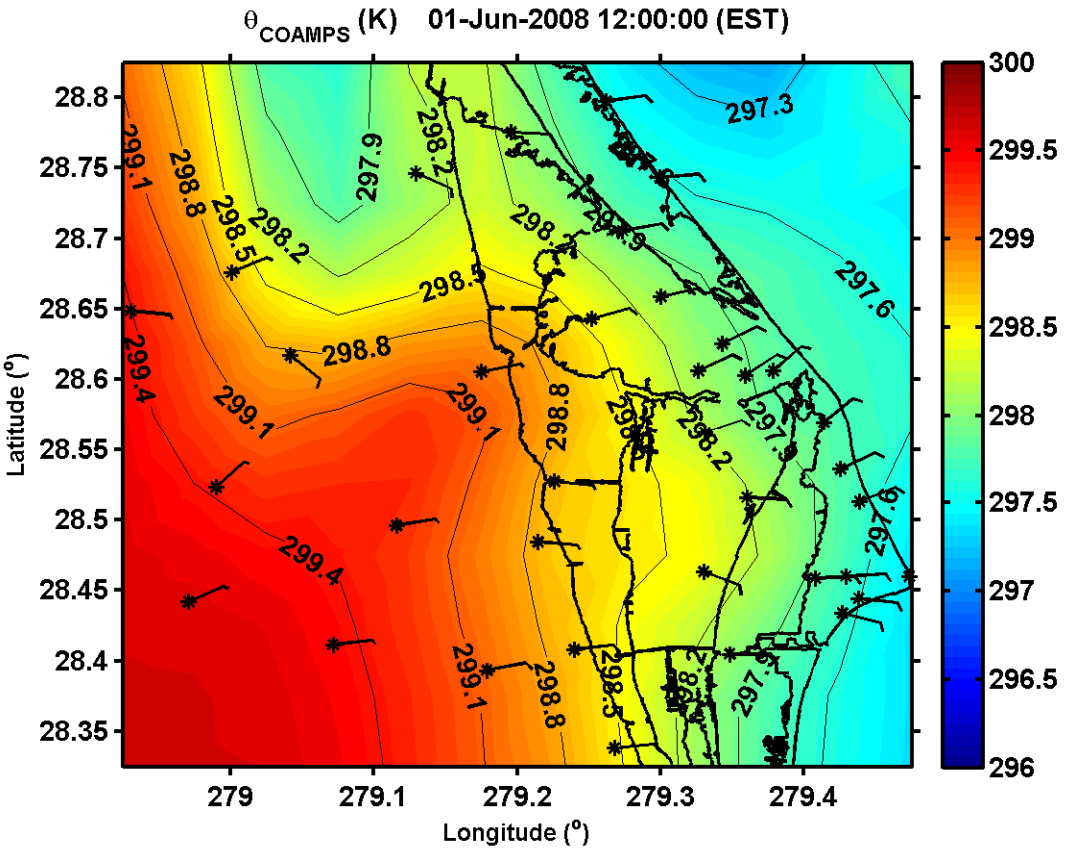

Figure 8. COAMPS™ generated contour plot of 1.8 m potential temperature at 1200 EST on 1 June 2008.

THIS PAGE INTENTIONALLY LEFT BLANK

IV. KSC/CCAFS OBSERVED SEA BREEZE CIRCULATIONS

A typical summer atmosphere over east-central Florida is dominated by a prevailing subtropical anticyclone commonly known as the Bermuda High. This semi-permanent area of high pressure forms over the cooler Atlantic Ocean during the warm seasons and is a central weather player for the southeastern United States. The clockwise circulation around the high produces a general light geostrophic flow over the Florida peninsula and also deflects any cyclone track northward.

The synoptic scale anticyclonic circulation over the region provides the necessary wind and redistribution of energy and moisture to enhance sea and land breeze circulations along coastal regions. In this chapter, we will focus on two 5-day periods when sea breeze circulations are most apparent under weak synoptic forcing. The two cases are referred to as Case #1 (1–5 June 2008) and Case #2 (18–22 June 2008). The general characteristics of these observed coastal circulations will be discussed here, which sets the stage for COAMPS^{TM} simulations evaluation discussed in Chapter V.

A. MEASURES OF VARIABILITY

1. Temporal Variability

Figure 9 contains time series of observed mean wind speed, wind direction, potential temperature, (θ) and humidity (q) from the lowest level sensors of Tower 0313 from Case #1. Green arrows in Figure 9 indicate the time of SBF passage for each day, which occurred shortly before noon on days 152–155 (1–4 June 2008). SBF passage is most easily identified in time series plots by a sudden backing of wind direction from southwest to east followed by a sharp increase in wind speed.

A clear diurnal variation in all variables is evident with the exception of specific humidity. For all five days shown in Figure 9, potential temperature at 1.8 m varies by about 10 K between day and night, while near surface wind varied between calm and 5 ms^{-1} with the highest wind speed occurring one to several hours after SBF passage. Complex temporal variations are seen in water vapor specific humidity with some sudden changes. Abrupt increase in q are seen in some days following sea breeze onset (days

152 and 155), but not apparent on other days. On day 153, sudden decreases in both temperature and q are seen following the onset of land breeze. A weak correlation between q variability and timing of maximum daily wind speed exists. The complex water bodies around KSC/CCAFS make it difficult to isolate an exact source and causes of q variability throughout the day.

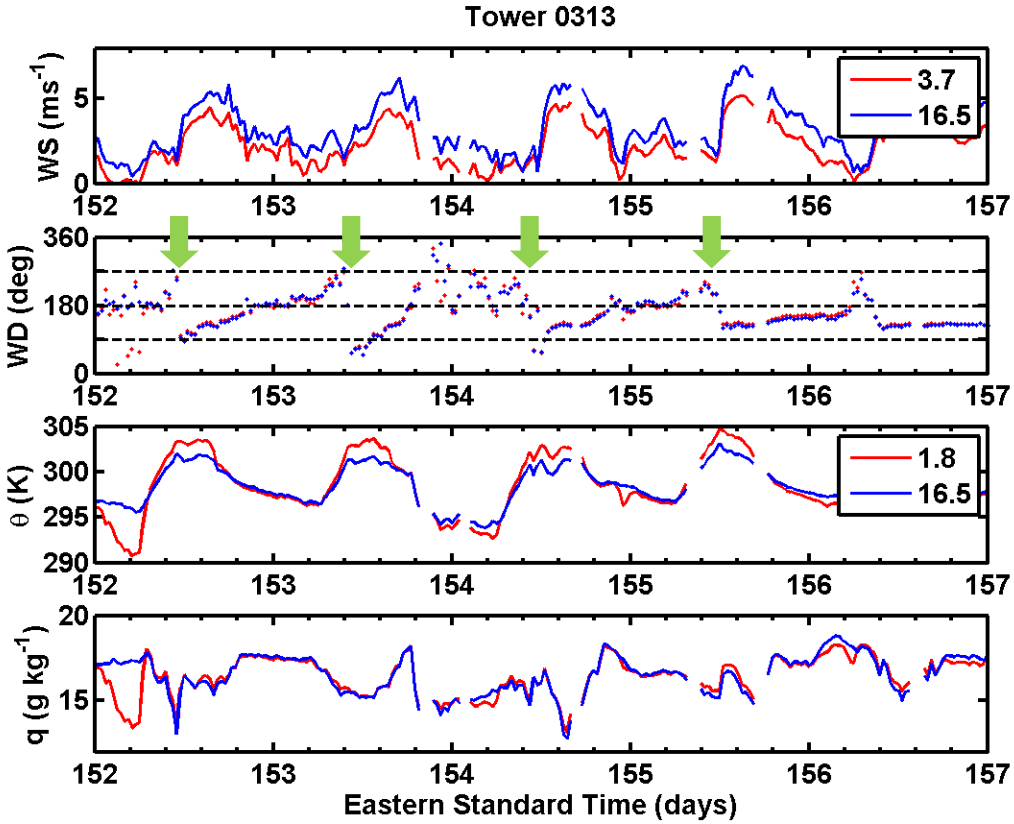

Figure 9. Temporal variations of observed wind speed (*WS*), wind direction (*WD*), potential temperature (θ) and specific humidity (q) from Tower 0313 for Case #1.

Figure 10 contains time series of the calculated latent heat flux (LHF), sensible heat flux (SHF) and momentum flux (MFL). All three fluxes show some signs of diurnal variability, particularly in SHF. At tower 0313, about 5.5 km inland from the coast, the SHF is the largest at midday at about 350 Wm^{-2} and coincide with maximum daily air temperatures. The LHF does not indicate well-defined diurnal variations except for Day

155 and 156 where the peak LHF reached ~200 Wm^{-2}. The LHF's complicated variability is likely associated with the irregular *q* variability seen in Figure 9, which is affected by a combination of horizontal advection from nearby water sources. The MFL increases following SBF passage as winds shift from offshore to onshore and increase in magnitude. During nighttime, negative and low SHF values were calculated (although not obvious in Figure 10 due to its small magnitude compared to the daytime maxima). Similarly, the MFL and LHF are both trivial in the nocturnal stable boundary layer.

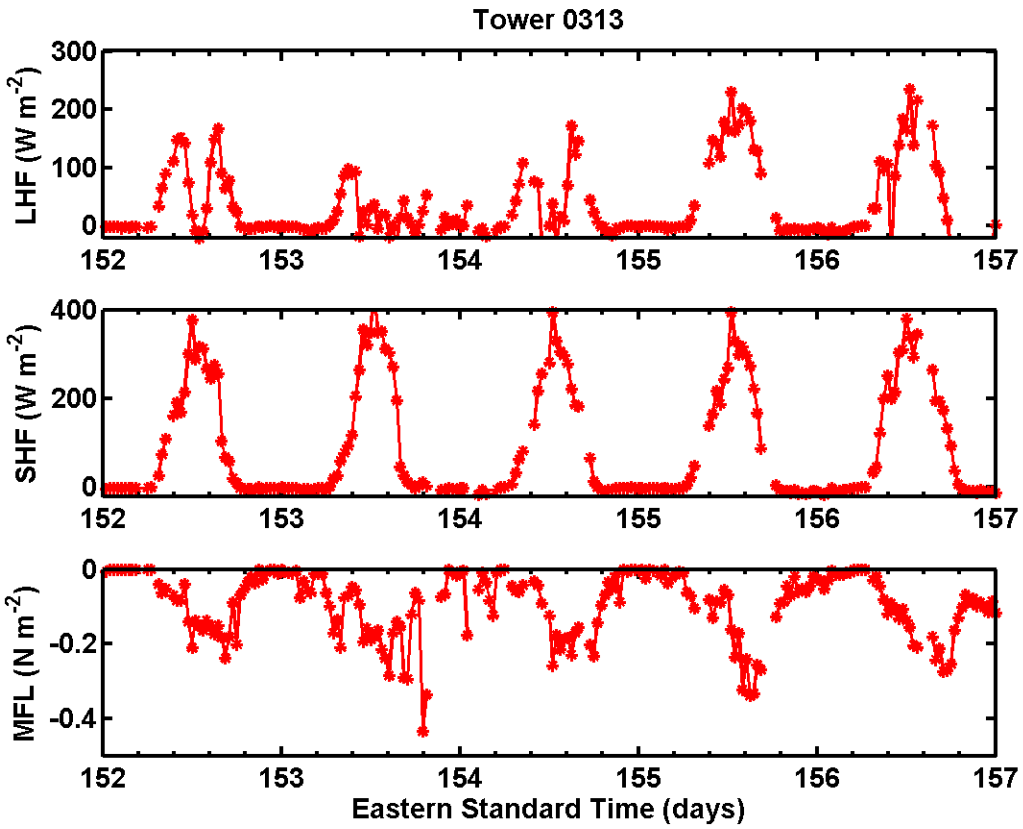

Figure 10. Temporal variations of calculated latent and sensible heat flux and momentum flux from Tower 0313

Figures 11 and 12 depict temporal variation during Case #1 as seen from Tower 0002, located at the Atlantic Ocean coastline. The SBF is not as well-defined as at Tower 0313, especially with the mean synoptic wind coming from the south on days 152, 155, and 156. The diurnal variability in potential temperature at both levels and in surface

SHF is still apparent, although the maximum SHF is much smaller with a maximum of about 200 Wm^{-2} at this coastal location. A relatively large diurnal variation of specific humidity, compared to Tower 0313, exists owing to close proximity to an abundant advective source region. On the last two days of Case #1, LHF has very weak diurnal variations with larger night time values and smaller magnitude during the day compared to inland towers, possibly reflecting the effects of upwind marine air.

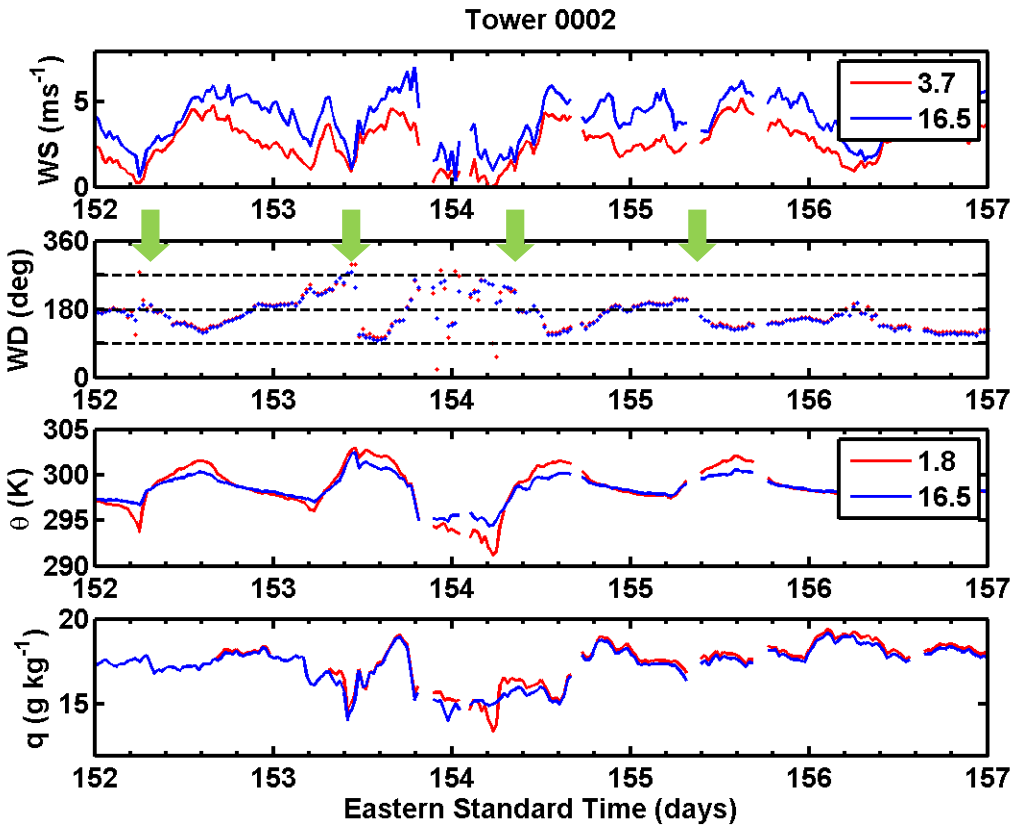

Figure 11. Temporal variations of observed wind speed, wind direction, potential temperature and specific humidity from Tower 0002 for Case #1.

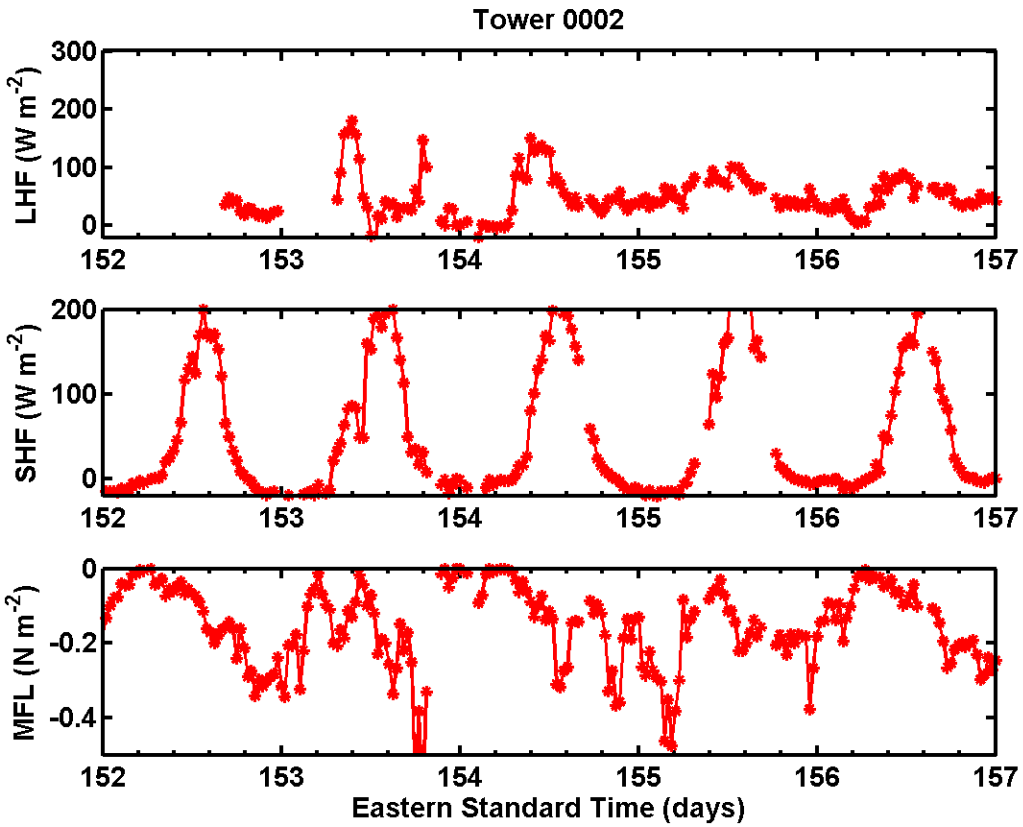

Figure 12. Temporal variations of calculated latent and sensible heat flux and momentum flux from Tower 0002

Figures 13 and 14 are time series plots of observations and calculated fluxes from Tower 0110, a launch critical tower located approximately 1.8 km from the shoreline. The eastern shore of the Banana River (actually a large brackish lagoon) is about 50 m west of Tower 0110. In Figure 13, a strong diurnal temperature variation is observed at both levels. The unstable thermal stratification is apparent in the temperature difference during the most unstable daytime period. Similar to Case #1, water vapor specific humidity shows abrupt changes associated with SBF passage on certain days. Some abrupt changes in q, such as at day 171.8, were associated with slight wind direction shifts, which is also evident in other nearby towers. Again, this change in q has to do with the complex water sources in the area. Similar to Case #1, a mostly well-mixed q is observed in the lowest layers supporting a notion that the primary source of surface layer moisture is from advection by nearby sources and not vegetative or soil fluxes.

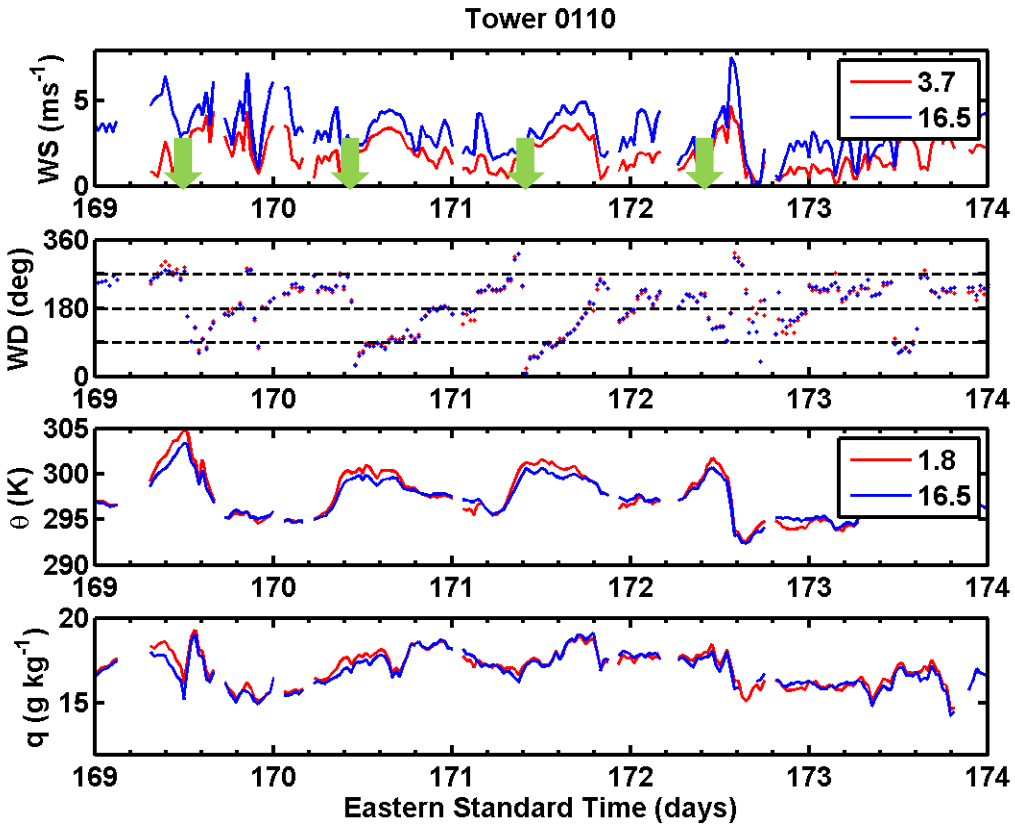

Figure 13. Time series of wind speed, wind direction, potential temperature and specific humidity from Tower 0110 in Case #2.

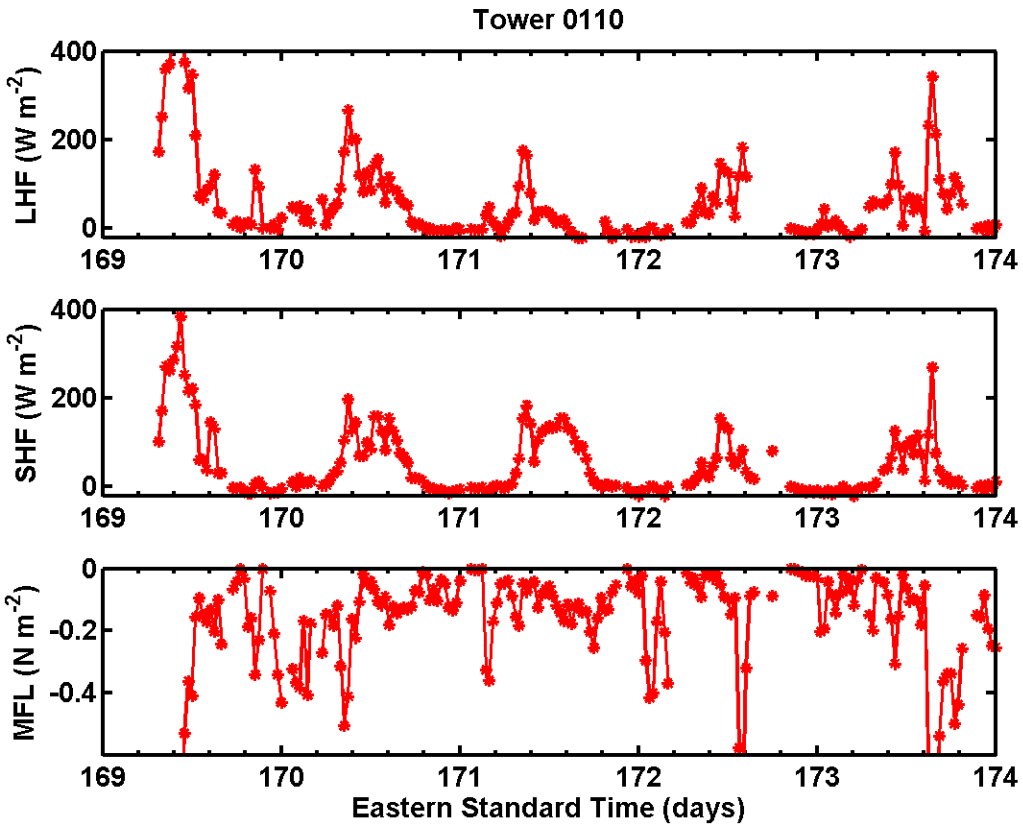

Figure 14. Time series of calculated latent and sensible heat fluxes and momentum flux from Tower 0110 in Case #2.

A second example from Tower 0006, a launch critical tower, in Case #2 is shown in Figures 15 and 16. This tower is located along the Atlantic Ocean coastline approximately 7 km south of Tower 0110. Again, green arrows on Figure 15 identify the approximate timing of a SBF passage on each day. This timing is chosen based on the switch of wind direction to onshore, which sometimes also accompanied by slightly lower temperatures at both levels. These figures indicate extreme similarity with the corresponding plots from Tower 0110. Note that both towers share a stretch of relatively straight coastline with no significant curvature. The similarity of their measurements indicates a region of some homogeneity in a rather complex area.

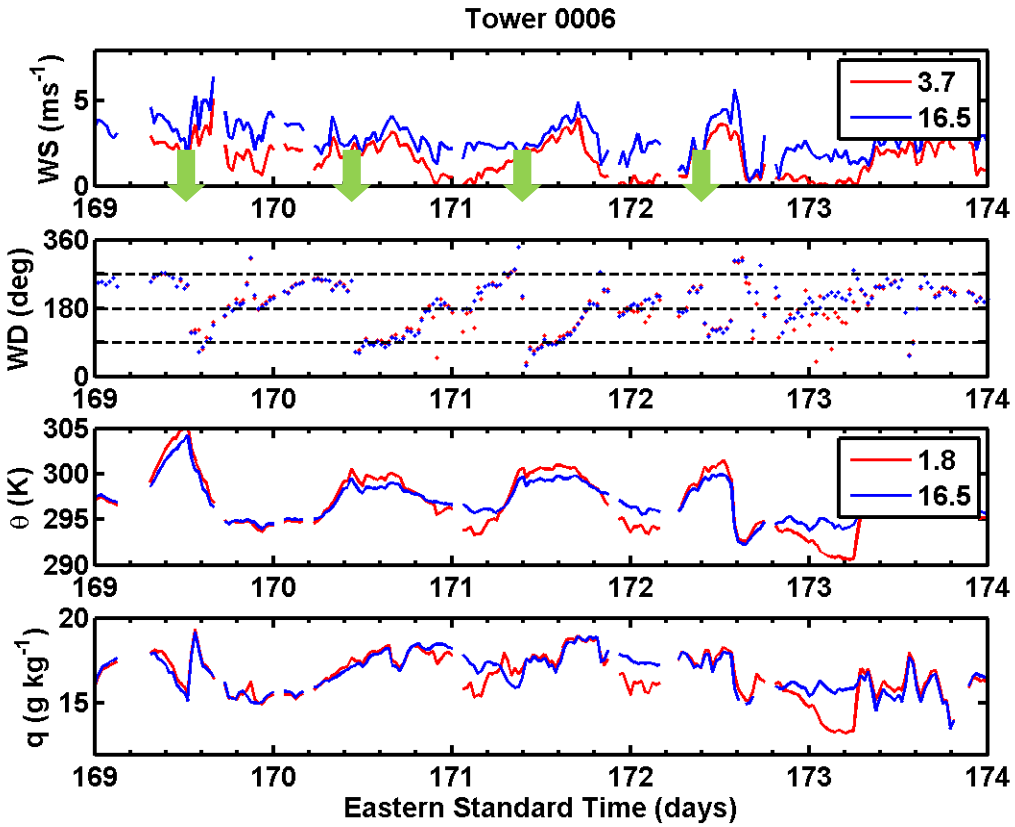

Figure 15. Time series of wind speed, wind direction, potential temperature, specific humidity from Tower 0006 in Case #2.

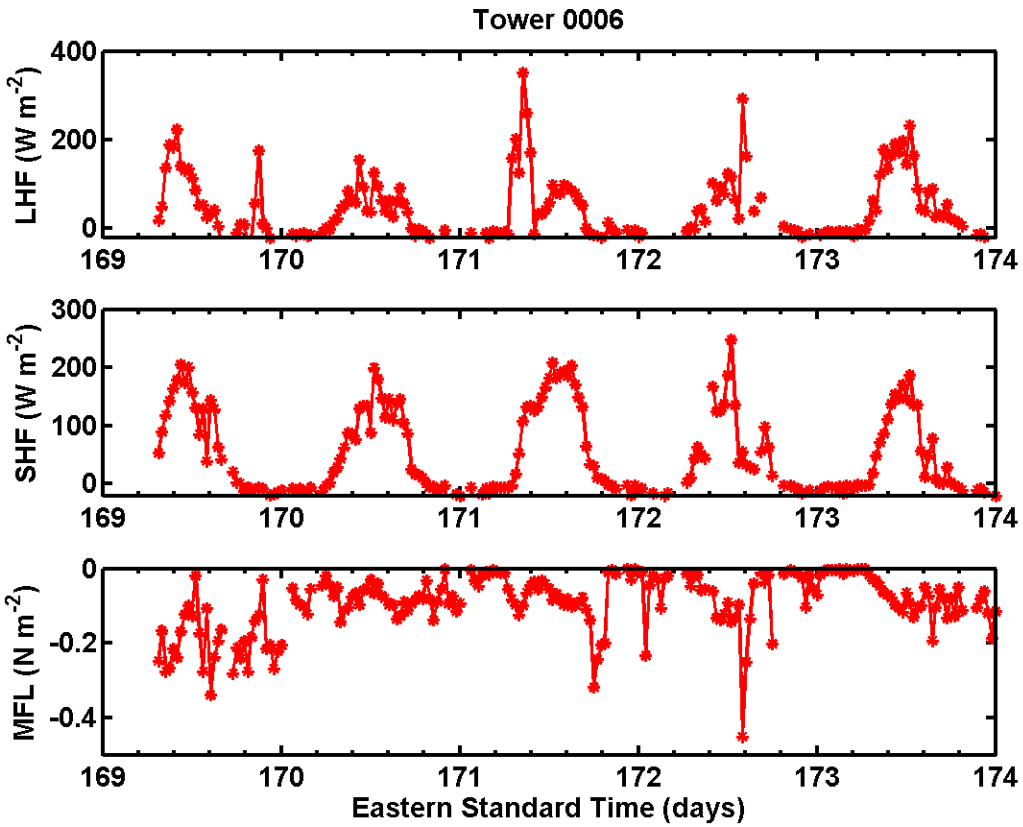

Figure 16. Time series of calculated latent and sensible heat flux and momentum flux from Tower 0006 in Case #2.

2. Spatial Variability

Contour plots generated in MATLAB are useful tools when examining horizontal spatial variability of phenomena-based events. Figure 17 is a series of potential temperature contour plots generated from WINDS tower observations during a SBF passage on 1 June 2008. Beginning at 1000 EST, offshore winds slow as the nighttime temperature gradient between the Atlantic Ocean and land dissolves leaving a fairly uniform temperature field across KSC/CCAFS. The land mass continues to warm through midday forcing air to rise; initiating a low level onshore wind shift and advection of cooler air from the Atlantic Ocean. Figure 17b shows the wind field complexity associated with a concave shoreline and numerous inland waterways. The advancing SBF converges over Merritt Island and bows the isotherms up and around the Indian River. The temperature gradient between points east of the Indian River and Atlantic Ocean

reach an astounding 6 Kelvin by 1400 EST. A combination of prolonged cool air advection and decaying sunlight dissolves and pushes the boundary inland by 1600 EST.

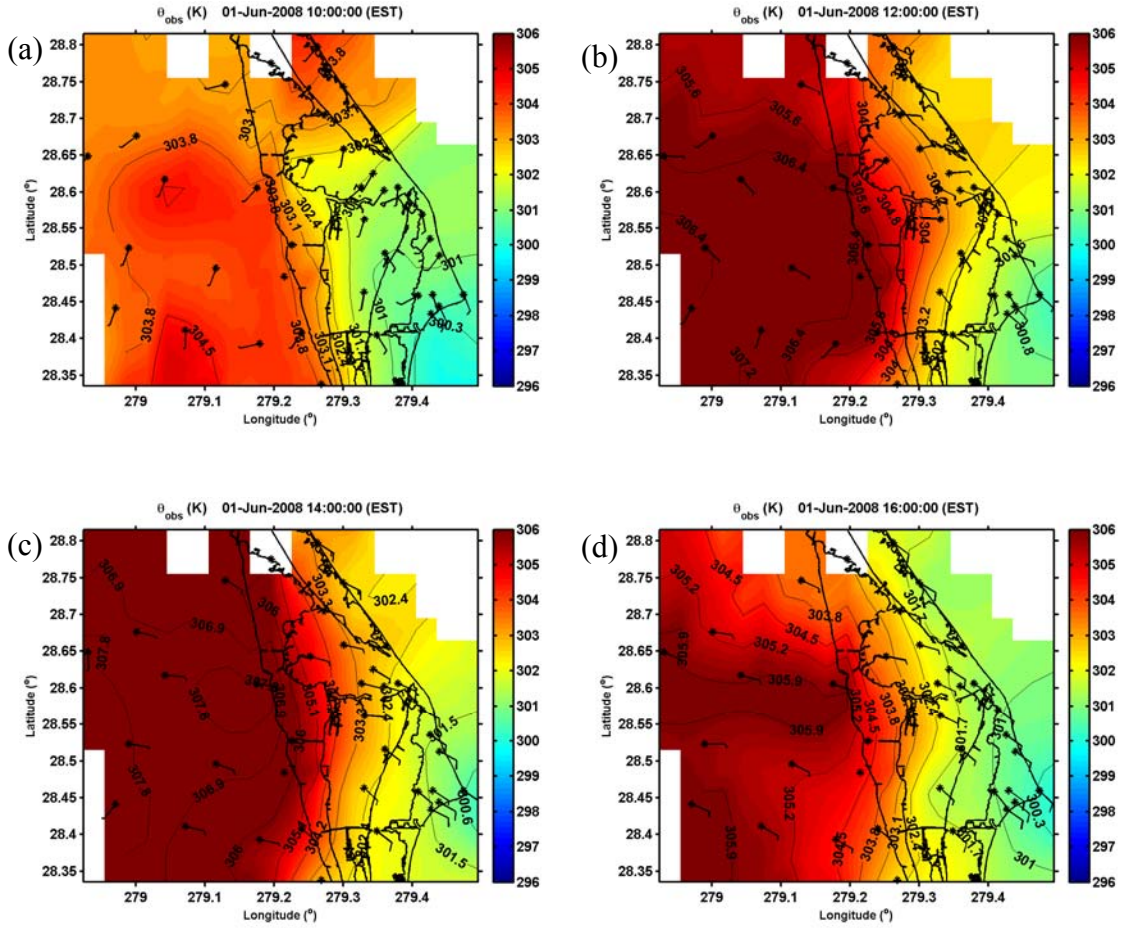

Figure 17. Contour plots of WINDS measured potential temperature distribution at (a) 1000, (b) 1200, (c) 1400 and (d) 1600 EST on 1 June 2008.

Figure 18 is a series of potential temperature contour plots generated from WINDS tower observations during a SBF passage on 18 June 2008. As in Figure 17, morning offshore flow results from a fairly uniform potential temperature field through the region. In the afternoon, winds begin to switch to onshore and lead cool, moist air advection from the Atlantic Ocean inland. Again, the Indian River slows the inland progression of cool air and a strong temperature gradient develops. The SBF is particularly robust in this example with an 11 K difference between Cape Canaveral and western border of the Indian River.

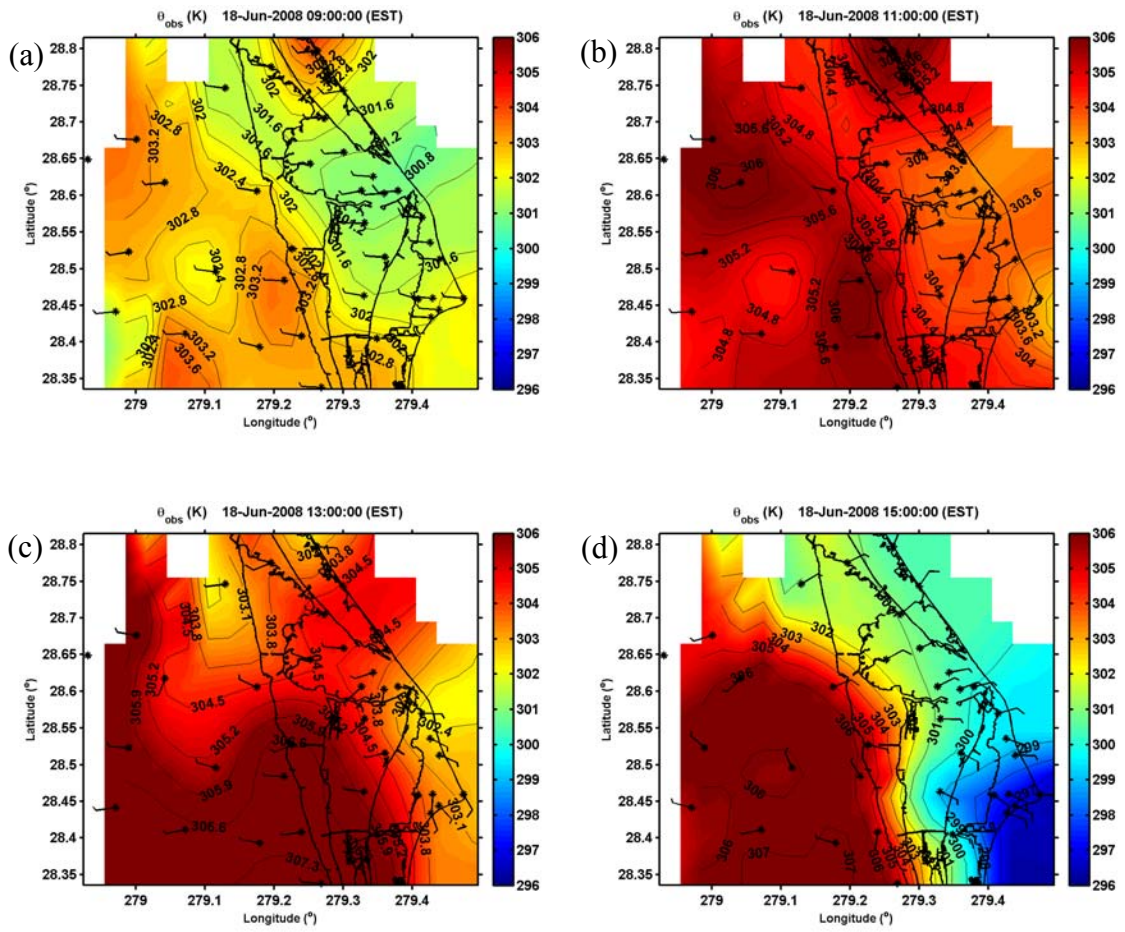

Figure 18. Contour plots of WINDS measured potential temperature distribution at (a) 0900, (b) 1100, (c) 1300 and (d) 1500 EST on 18 June 2008

Figure 19 is a four-panel time series of contour plotted SHF spaced every two hours during the same sea breeze event as in Figure 17. The SHF values increase in response to daytime surface heating and remain fairly high through the time series as heat is fluxed upward into the near surface layer. The largest values are calculated near CCAFS (CCAFS is mostly concrete and hardened facilities) from Tower 0003. We exercise caution with accepting SHF values from Tower 0003 as it returns routinely high values as measured against nearby towers. The smallest values are closer to the Indian River owing to the larger heat capacity of water than land and thus, minimal upward heat flux. By 1500, SHF is maximized over land surfaces due to onshore flow and entrainment of cool, moistened air from the Atlantic Ocean competing against upward heat fluxes.

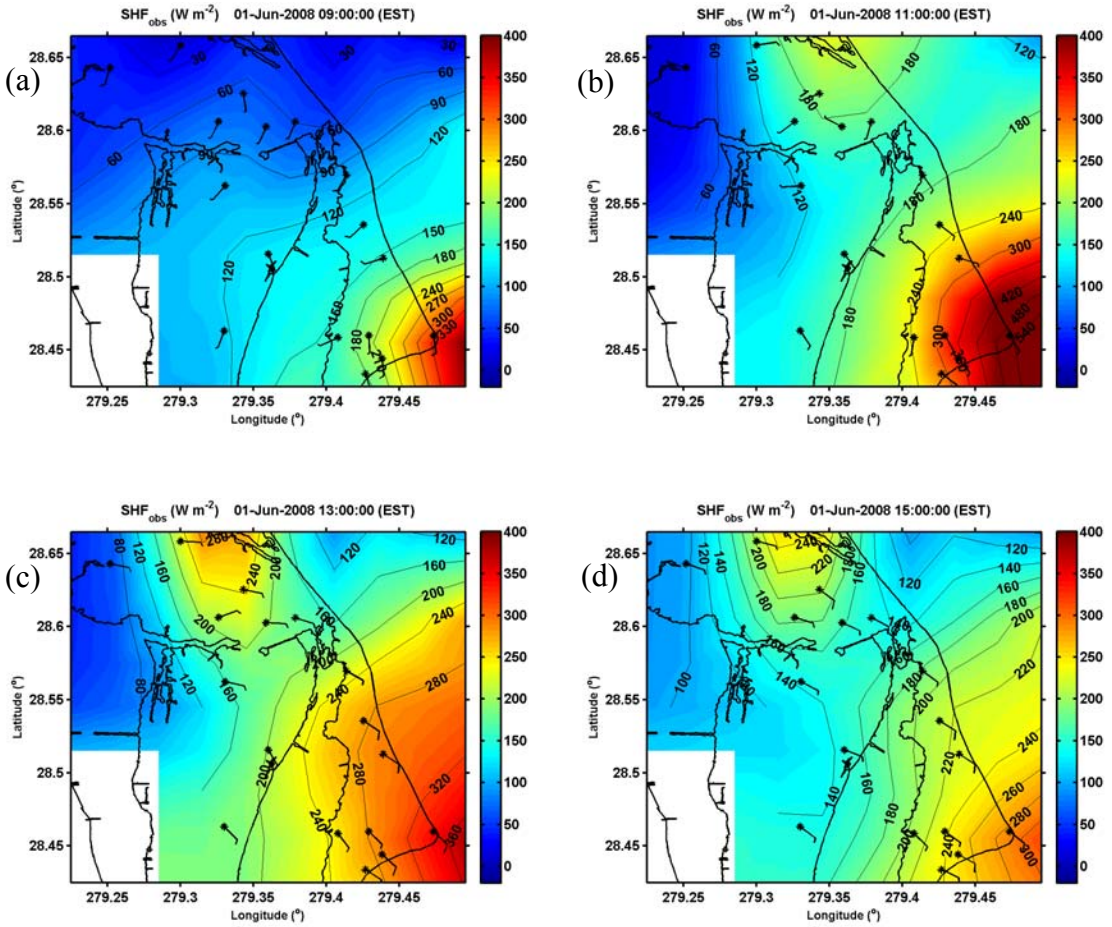

Figure 19. Same as in Figure 17, except for sensible heat flux (SHF from 17 towers).

To fill a data void region above 150 m in the boundary layer, part of the KSC/CCAFS mesonetwork, is a network of five 915 MHz DWRPs in a diamond-shape configuration (see Figure 4) surrounding the shuttle landing facility. Profiler data is used to better understand the vertical variability of a complex coastal circulation. Figures 20 and 21 show time-height contour plots of wind speed and wind direction, respectively, from four of the profilers for Case #1 (data from Profiler #4 was verified against nearby tower data, reasoned to be erroneous and omitted from this study). The onset and termination of the sea breeze events are clearly seen in these figures. The sea breeze vertical extent is around 1 km as indicated by SBF passage wind speed spikes ranging between 6–12 ms^{-1}. Land breeze heights are difficult to observe but range between 150–300 m high and are best seen through WINDS tower measurements.

Comparing measurements from the four spatially-separated profilers reveals substantial similarity in wind speed and direction from all locations, especially in profilers 1, 2, and 3. These three profilers are within 20 km of each other and are closer to the coastline. Profiler 5 is further inland on the other side of the Indian River and thus, the sea breeze signature is weaker. A slight delay in the SBF can be seen at Profilers 3 and 5 compared to Profilers 1 and 2. This is also due to the difference in location as Profiler 1 and 2 and Profilers 3 and 5 are divided by the Banana River. Day 155 shows an increased vertical extent to around 1200 m. This enhancement may be caused by HCRs forming along an advancing SBF boosting the vertical extent (as observed by Rao and Fuelberg, 1999). A proven hypothesis is beyond the scope of this study.

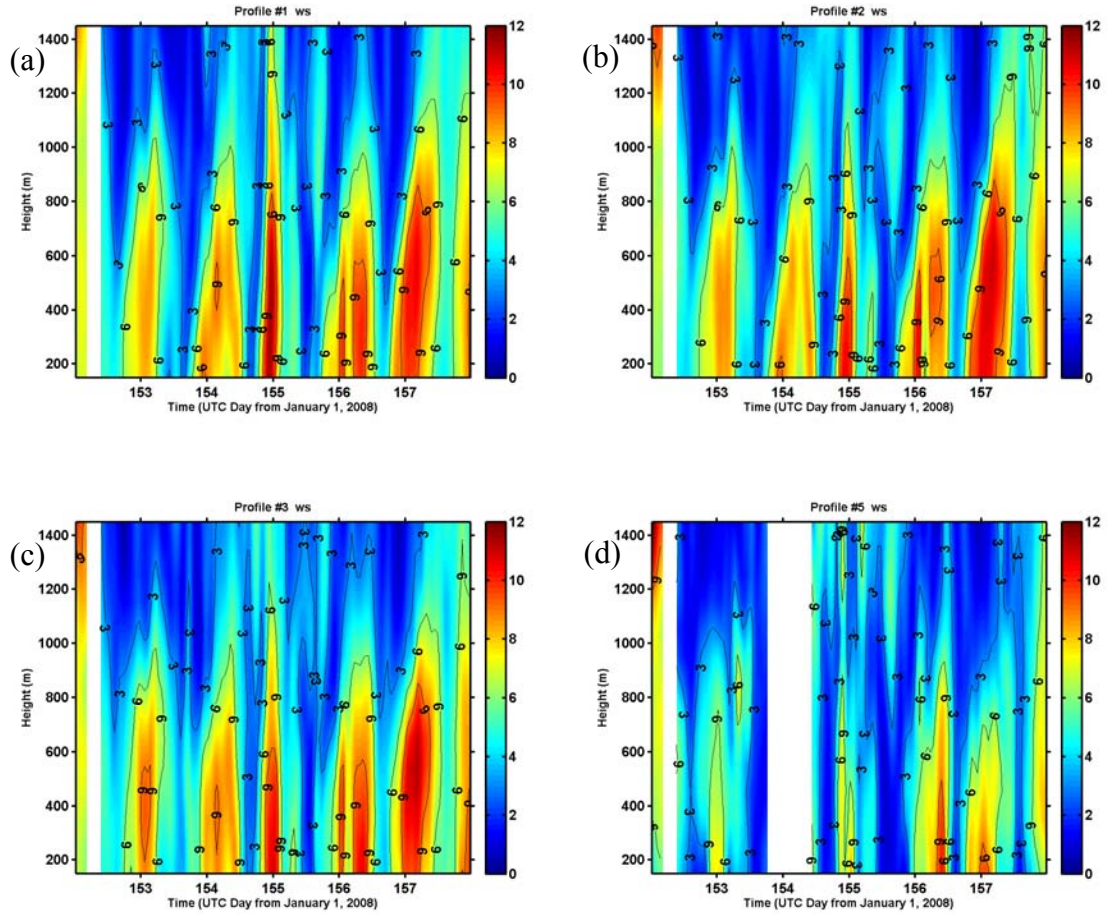

Figure 20. Wind speeds (ms^{-1}) from DWRP (a) 1, (b) 2, (c) 3 and (d) 5 for Case #1.

Figure 21 reveals similar results to the wind speed measurements. SBFs are identified by sudden veering of winds from southwest (orange in color bar) to southeast (blue in color bar) coinciding with increased wind speeds. On day 154, low level winds suddenly veer from 210^0 to 70^0 while upper level winds remain from 210^0 for a few hours. The daytime circulation depth reaches 1 km; matching our observation from Figure 20. Winds shift to an offshore, land breeze beginning shortly after 0000 UTC for most days. The clockwise rotation of the coastal circulation is evident, however far from uniform. Winds rapidly rotate during the daytime, turn slowly in the evening and are steady-state overnight.

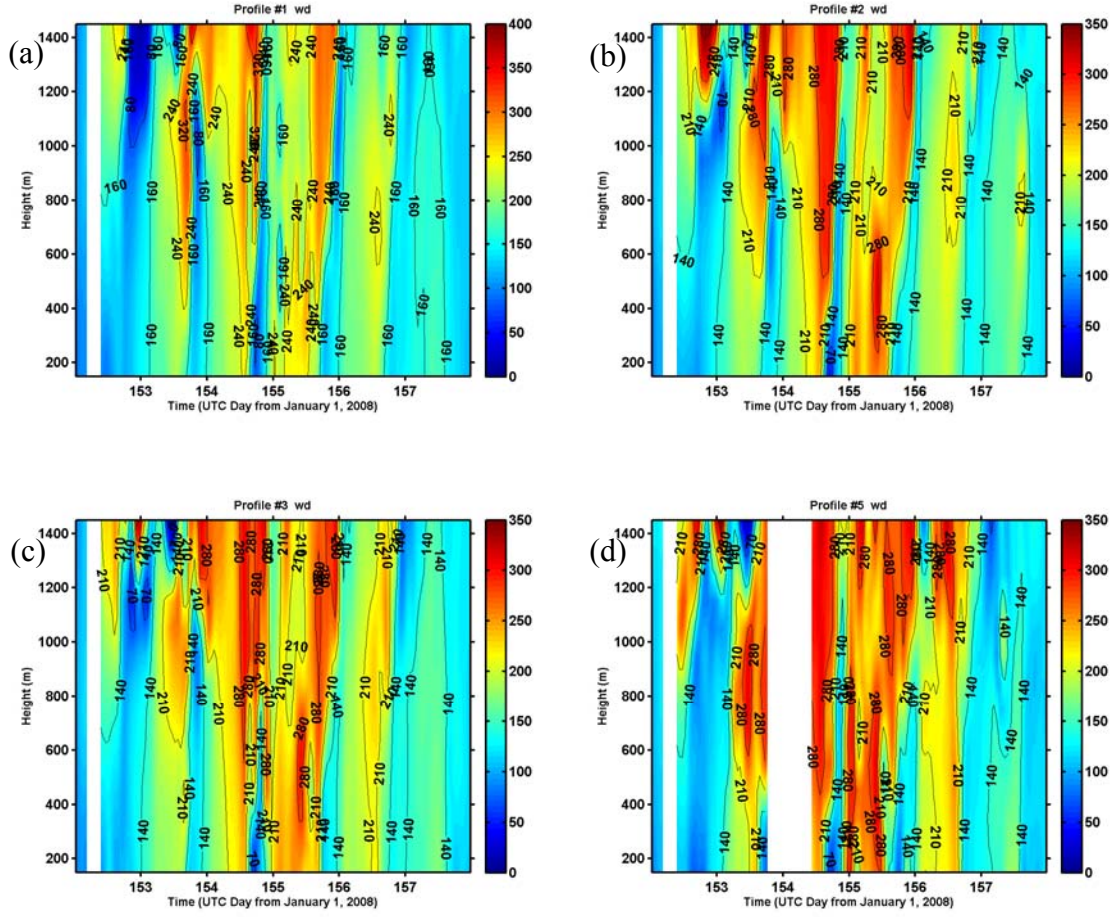

Figure 21. Wind direction from DWRP (a) 1, (b) 2, (c) 3 and (d) 5 for Case #1

3. Surface Layer Evolution

With multiple levels in the lower 150 m (tower 0313) and 70 m (tower 0110), one can examine the surface layer vertical structure in great detail. Figure 22 contains observed vertical profiles of θ, q, wind speed and wind direction from these two towers on 3 June 2008. In both figures, at 0600 EST (prior to sunrise) the surface layer is thermally stable. With daytime heating, the lowest layers become increasingly unstable; all profiles after 0900 EST show an unstable/neutral surface layer. Warming of the surface layer is seen until 1200 EST followed by a gradual decrease. The sea breeze onset at Tower 0313 is likely just before 1200 EST. For Tower 0110, SBF passage was most likely well before noon as indicated by the evolution of both wind speed and wind direction. On this particular day, the surface layer moisture was relatively low at sunrise and increased until sea breeze onset. A sharp decrease in q is seen in both towers about 3–4 hours after the SBF passed despite an onshore southeast wind. It is not clear what caused this rather significant drying spell. As indicated in the time series analyses, q shows various abrupt variations, which are likely related to higher wind speeds and the numerous complex water bodies of different dimensions and temperatures.

The dashed-blue line in both figures is fitted log-wind profiles using the lowest two levels of wind measurements. The close proximity of the fitted line to the measurements at upper levels indicates weak thermal effects on surface layer mixing during the measurement period. Wind directions shift clockwise throughout the period similar to earlier presented time series.

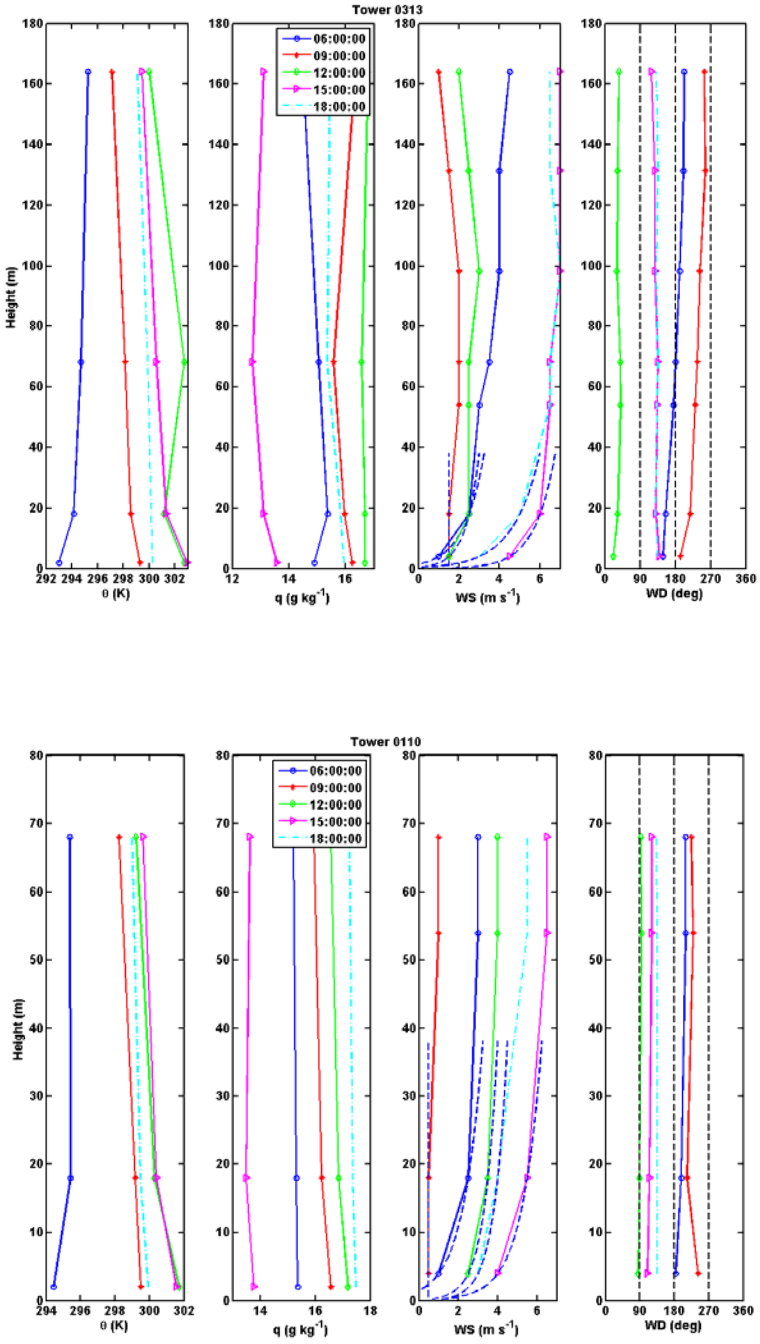

Figure 22. Vertical profiles of potential temperature, specific humidity, wind speed and direction from Tower 0313 (top) and Tower 0110 (bottom) every three hours on 3 June 2008

Vertical profiles with small temporal increments were crafted in order to show surface layer metamorphosis during a sea breeze onset. Figure 23 is a time series of

vertical profiles from Tower 0313 every 30–45 minutes before, during and after SBF passage on 1 June 2008. All potential temperature profiles are superadiabatic in the surface layer and near adiabatic above 60 m. The wind speeds are subgeostrophic throughout the surface layer and decrease to zero at the surface, resulting in a wind profile that is nearly logarithmic with height. This log-wind profile is plotted in dashed-blue lines for the lowest two layers. At 1125, wind directions in the lowest four levels indicate a SBF passage while measurements aloft remain unchanged from 1100. Wind speeds remain minimal at 1125 but increase rapidly throughout the profile by 1200. By this time, a SBF has passed through all levels as indicated by a low level moisture surge, cooling of the surface layer potential temperature profile and a 4 ms^{-1} wind speed increase.

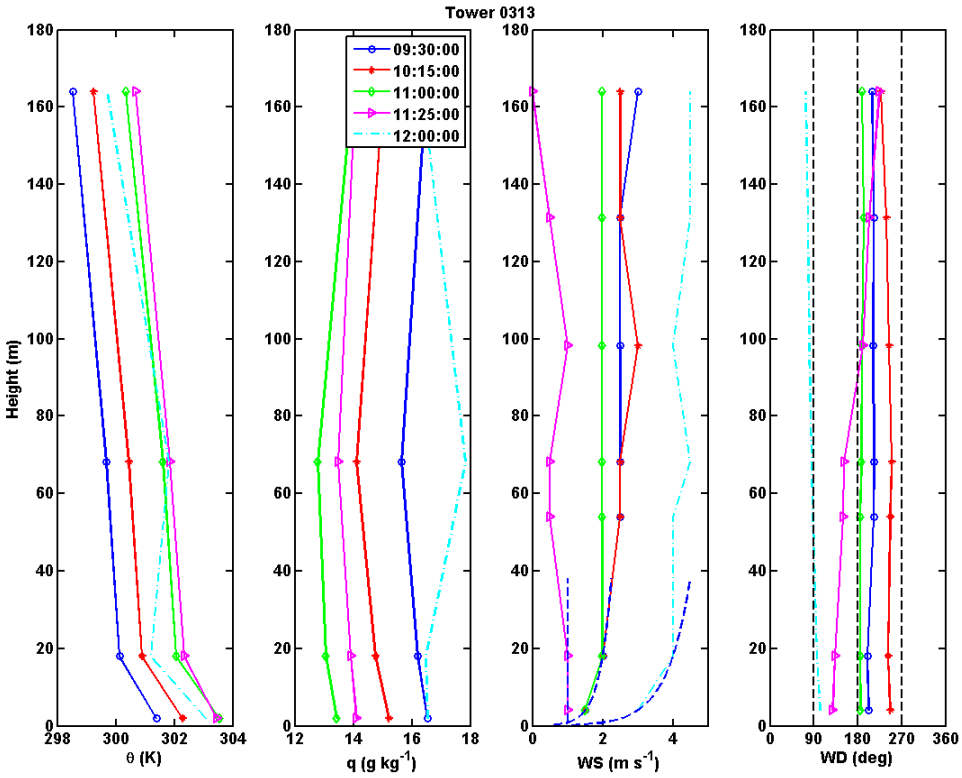

Figure 23. Vertical profiles of potential temperature, specific humidity, wind speed and direction from Tower 0313 shortly before, during and after SBF passage on 1 June 2008.

THIS PAGE INTENTIONALLY LEFT BLANK

V. EVALUATION OF COAMPS™ SIMULATED COASTAL CIRCULATIONS

COAMPS™ has provided operational regional weather forecasts to the U.S. Navy and DoD partners for nearly 20 years. Since inception in 1995, numerous modifications to the physics parameterization packages have improved COAMPS™ ability to parameterize sub-grid scale processes with better success. COAMPS™ has been run with increased model resolution in past studies in an effort to resolve fine structures of mesoscale circulations over complex surface configurations, such as near a coast. Previous research has shown the value of higher-resolution models. The higher-resolution models show improvements in structure definition and more provide a more realistic representation, which researchers then evaluate subjectively. The objective evaluation of such high-resolution simulations is problematic due to insufficient spatial and temporal observation density to match the model resolution. This issue was discussed in Mass et al (2002). Because high-resolution models generate much stronger spatial variability, traditional methods of verification are likely to fail when using observations from a single point. It is recognized that objective verification scores are highly dependent on the quality and density of an observation network. With insufficient data density, important mesoscale features can be missed or poorly represented in analyses, resulting in different (and often better) verifications for lower resolution domains compared to high-resolution grids.

With the dense meteorological sensor population at CCAFS, high-resolution model simulations can be evaluated with increased amount of measurements distributed over an area equivalent to the inner domain of a model. This chapter presents a first attempt to evaluate COAMPS™ simulations using the measurements from CCAFS mesonetwork. Cases with apparent sea breeze/land breeze circulation (as discussed in previous chapters) will be the target of this model evaluation. These cases are considered

'simple' due to the weak synoptic forcing and high frequency of occurrence. The CCAFS coastal circulation provided several days of similar flow patterns to allow significant statistical comparison.

All model forecasts in this study are verified against WINDS tower observations by interpolating linearly the grid based forecasts to the tower sites. The models' ability to forecast is being evaluated using a variety of methods. Traditional statistical verification, although may not be perfect for high-resolution models, still offers a quantifiable assessment of skill and required focus of deficiency. Such an evaluation is referred to as an objective evaluation. The WINDS network allows for thorough objective model evaluation and errors can be viewed with detailed spatial variability, such as distance from the coastline. To complement our objective analyses, this thesis work also employed subjective evaluation techniques to fully access the model strength and weakness. Hence this study is able to reveal in great detail about COAMPS^{TM} performance in simulating a coastal circulation.

Table 1 defines objective verification statistics employed in this study. Here, f_i and o_i represent COAMPS^{TM} forecast interpolated onto the *i*th tower and the observation from the *i*th tower, respectively. The overbar represents an average over all towers. These statistics will be used to compare COAMPS^{TM} forecast for potential temperature (θ), water vapor specific humidity (q), wind speeds (*WS*) and wind direction (*WD*), sensible (*SHF*) and latent heat (*LHF*) fluxes and momentum fluxes (*MFL*).

Table 1. Table of objective statistics used in this study.

Statistic	Formula
Bias	$= \frac{1}{n}\sum_{i=1}^{n}(f_i - o_i)$
Error Variance	$= \sum_{i=1}^{n}(f_i - o_i)^2$

Statistic	Formula
Root Mean Squared Error	$=\sqrt{\frac{1}{n}\sum_{i=1}^{n}(f_i-o_i)^2}$
Correlation Coefficient	$=\frac{\sum_{i=1}^{n}(f_i-\overline{f})(o_i-\overline{o})}{\sqrt{\sum_{i=1}^{n}(f_i-\overline{f})^2\sum_{i=1}^{n}(o_i-\overline{o})^2}}$

A. RESULTS FOR SELECTED CASES

The objective of this thesis is to examine COAMPS^{TM} performance in representing the diurnal sea breeze circulation normally under weak synoptic forcing. Due to the diurnal occurrence of sea breeze circulation, many similar cases can be obtained to enhance the statistical significance of a model evaluation. All cases selected for this study were chosen for their prominent coastal circulation features seen from the measurements of all spring and summer days from 2008. Careful examination of each day discovered the existence of 64 sea breeze days in 2008. Of those 64 days, the two blocks of time (1–5 and 18–22 June) included in this study showed consistent sea breeze characteristics across a five day span. These consecutive occurrences of sea breeze days are best cases for COAMPS^{TM} simulation for the purpose of model observation comparison.

1. Case #1, 1–5 June 2008

Case #1 defines a typical spring period along the east-central Florida coast. Reed (1979) found the strongest coastal circulations formed in the late springtime over KSC/CCAFS. This is due to an amplified temperature gradient between a cool Atlantic Ocean recovering from winter and a land surface subjected to increased heating from solar radiation. Figure 24 is a series of SE CONUS surface observation charts for June 2008 (Adapted from NOAA) showing the dominance of a weak surface high pressure over the Gulf of Mexico, resulting in relatively weak synoptic-scale influence over the

Florida Peninsula. These charts reflect overall synoptic conditions for all sea breeze days presented in this thesis except for 18 June 2008. On 18 June 2008, a decaying stationary frontal boundary was located 100 km north of KSC/CCAFS and may have increased the ambient flow over this region.

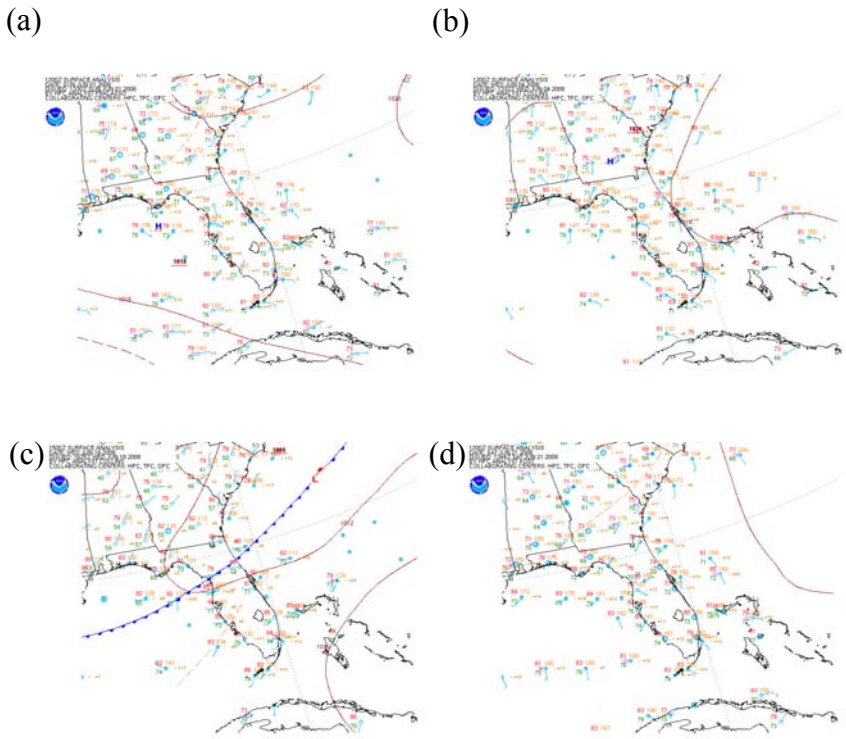

Figure 24. Series of surface observation charts for (a) 1, (b) 4, (c) 18 and (d) 21 June 2008 at 1200 UTC (From NOAA).

Figure 25 presents a comparison between COAMPS^{TM} interpolated and 36 WINDS tower observations of θ (at 1.8 m) contour plots over the KSC/CCAFS region at 1000, 1200, and 1400 EST on 2 June 2008. The wind barbs from each tower or tower locations are also shown in this figure.

The most apparent temperature difference between COAMPS^{TM} and WINDS is the cold bias in the COAMPS^{TM} simulation. On the ocean side, the near-coast observed temperature is warmer by nearly 4 K, while on the inland side, the observed temperature is nearly 10 K warmer. The observations show at 1000 EST an offshore land breeze persists as land temperatures west of the Indian River rapidly warm and coastal sites near

waterways are generally uniform. By midday, an observed tightening thermal gradient and sea breeze wind flow west of the Indian River marks the placement of a SBF in the observation. By 1400, the SBF stalls 10 km west of the Indian River and a 7 K temperature difference is seen between the coastline and the inland area. The simulated COAMPS^{TM} fields appear to have difficulties warming up the inland air temperature. As a result, the simulation is slow in establishing the coast-inland temperature gradient as seen in the 1.8 m temperature. The temperature difference is also small in magnitude. COAMPS^{TM} does depict a SBF but only calculates a sea breeze inland penetration of 10 km from the coastline which is approximately 20 km east of the observed location. This case is atypical of other simulated days in the timing of establishing the SB circulation, which is normally earlier than observations. It is speculated that the weak and slow daytime warming of the land surface low level temperature is a result of cloud cover generated in the model, although cloud cover was minimal from observations.

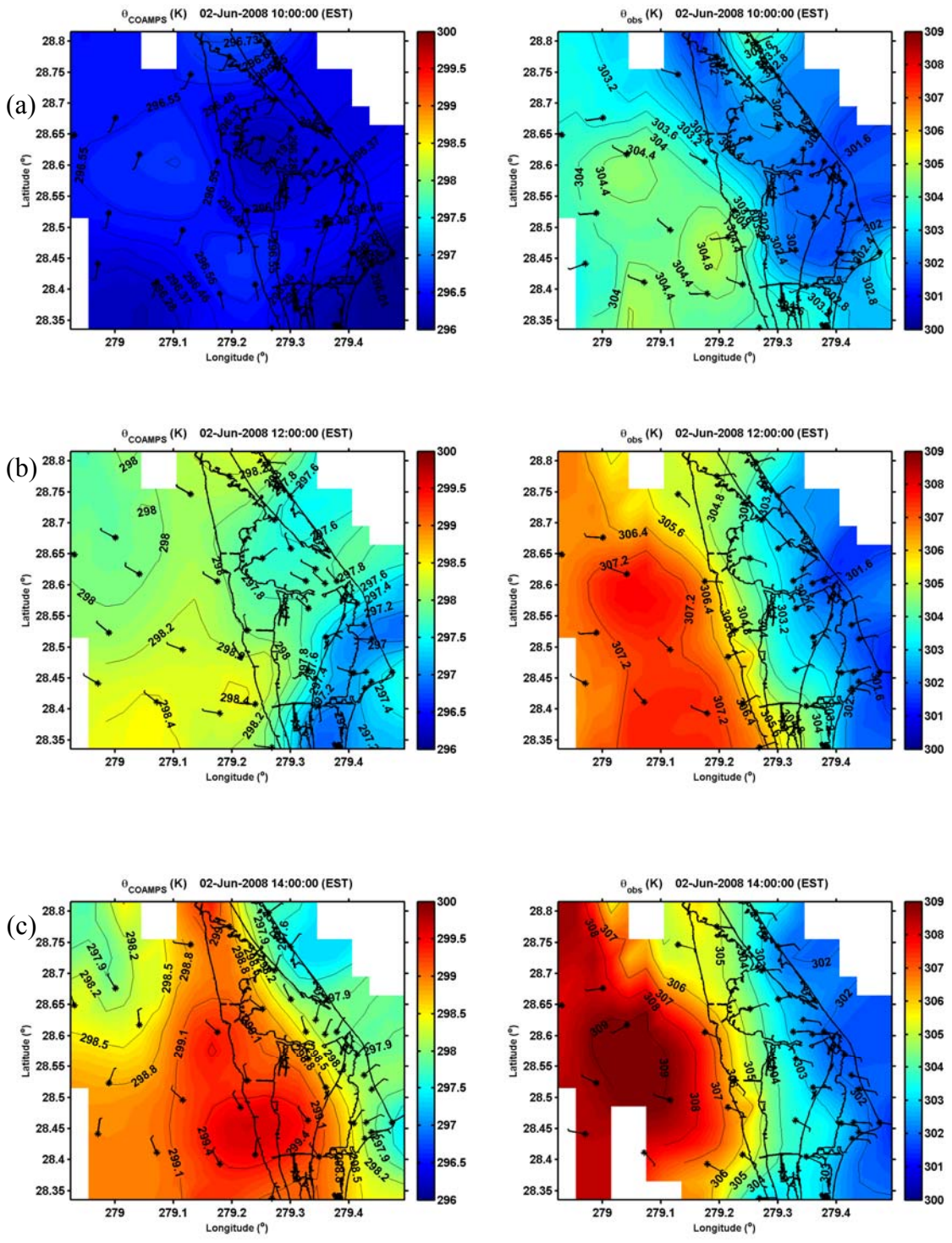

Figure 25. Contour plots comparing COAMPS™ (left) and WINDS observations (right) of potential temperature at (a) 1000, (b) 1200 and (c) 1400 on 2 June 2008.

Figure 26 contains vertical profiles of θ, q, WS and WD from COAMPS^{TM} (blue) and WINDS Tower 0313 (red) observations at 0600 and 1200 EST. Forecast and observation show fair consistency at 0600. COAMPS^{TM} has a cold bias of 1.2 K throughout the profile depth. COAMPS^{TM} wind speeds are weaker in the higher surface layer, but q and WD compares well with observations. Similar to other wind profiles, log-wind profiles are plotted in black dashed lines fitted for the observed lowest two levels of wind. Between 0600 and 1200, a SBF passed Tower 0313 as indicated by the wind direction and speed profiles at 1200 (Figure 26 bottom panels). The simulation does not show any onshore wind from SB circulation at this hour yet, suggesting a delay in SBF passage compared to the observations. On the other hand, the observed wind is also significantly stronger than the COAMPS^{TM} prediction by 2 ms^{-1} and the near-surface wind increased following SBF passage. This WS increase is also accompanied by a decrease in low level q. Again at 1200 EST, we see evidence of a COAMPS^{TM} cold bias.

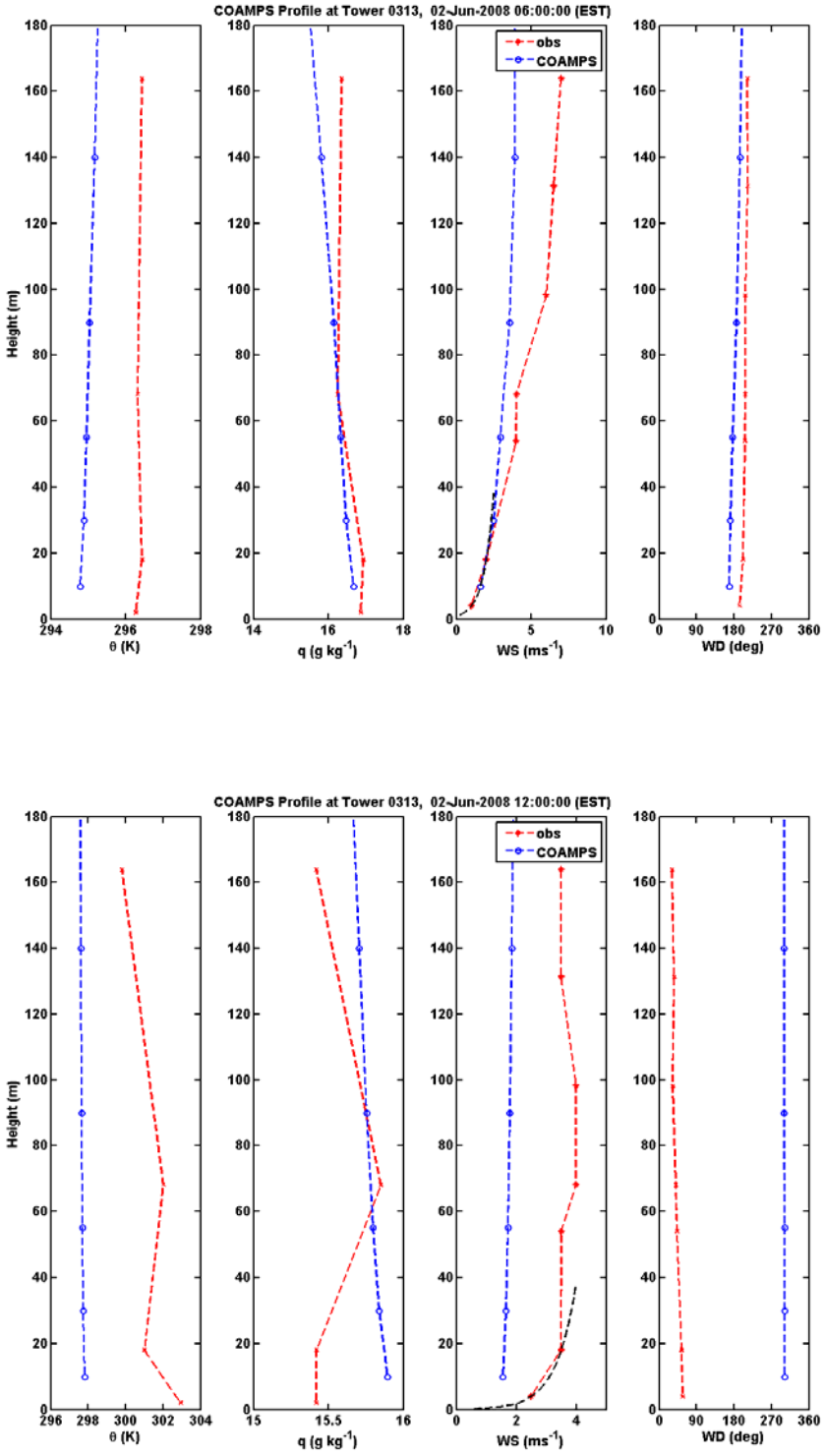

Figure 26. WINDS (red) and COAMPS™ (blue) vertical profiles of potential temperature, specific humidity, wind speed, and wind direction from T ower 0313 at 0600 (top) and 1200 (bottom) EST on 2 June 2008.

Figures 20 and 21 in Chapter IV contained observed vertical profiles of WS and WD from Profilers #1, 2, 3, and 5. We noted a sharp increase in wind speeds marking the SBF passage at all four sites. We also saw a similar WS magnitude for Profiles 1, 2 and 3 in Figure 20 but a delay in SBF passage between Profiles 1 and 2 and Profiles 3 and 5 in Figure 21. This variability is caused by location proximity to the numerous water bodies around KSC/CCAFS. Figures 27 and 28 contain COAMPS^{TM} simulated vertical profiles of WS and WD interpolated to the DWRP sites plotted in Figures 20 and 21. In general, COAMPS^{TM} underestimates WS under relatively higher wind conditions and extends higher vertically by roughly 300 m at each of these locations. For days 152 and 153 WS is fairly accurate with a peak speed of 8 ms^{-1} and vertical extent of 1 km. Figure 28 depicts this SBF passage with winds veering onshore shortly after 1500 UTC as indicated by dark blue adjacent to dark orange (see color bar). COAMPS^{TM} fails to depict the spatial differences between the location proximity to the Indian River.

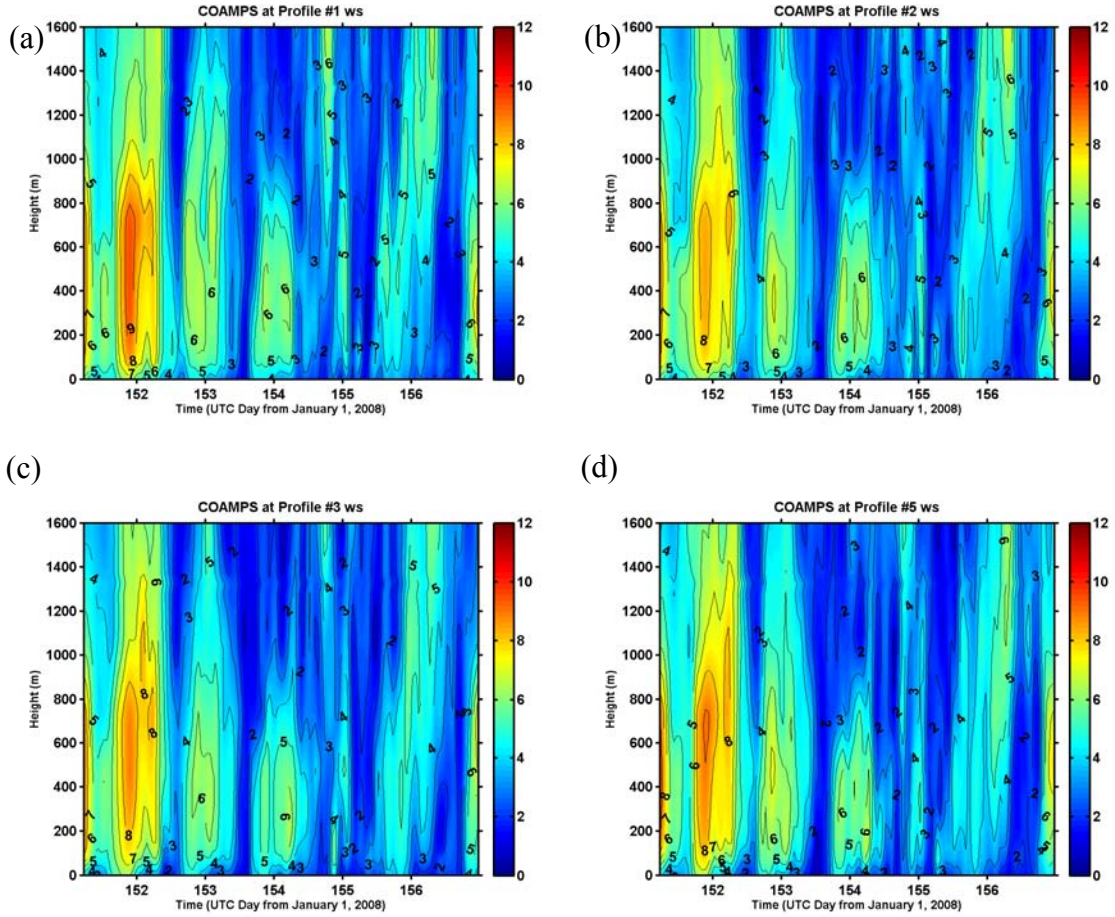

Figure 27. COAMPS^{TM} interpolated time-height wind speed (ms^{-1}) plots at DWRP (a) 1, (b) 2, (c) 3 and (d) 5.

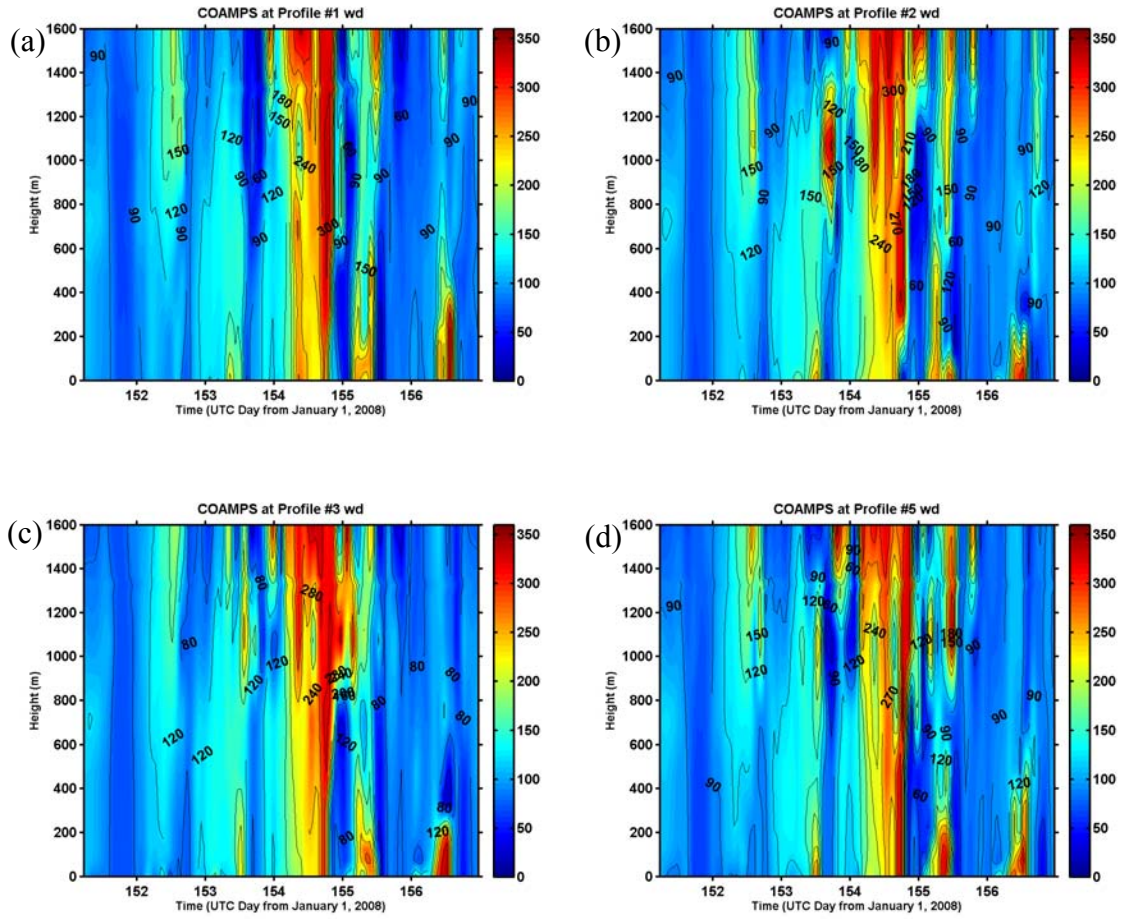

Figure 28. COAMPS^{TM} interpolated time-height wind direction (deg) plots at DWRP (a) 1, (b) 2, (c) 3 and (d) 5.

Figure 29 compares time variations over several days in Case #1 for mean and flux measurements from WINDS Towers 0313 and 0006 against COAMPS^{TM} interpolated to these tower locations. For temperature, the COAMPS^{TM} simulations at both tower sites does capture the diurnal θ cycle. The COAMPS^{TM} simulations do not represent the diurnal variation θ magnitude observed at both tower locations. Diurnal variations in q are not apparent in both model and observations; COAMPS^{TM} has a slight dry bias but simulations and observations at both towers do not seem to correlate well. Overall, simulated q has smaller temporal variations compared to those measured at each tower. WS and WD compared reasonably well, especially in the first two days. COAMPS^{TM} timing of SBF passage at both towers is discrepant by nearly an hour. This premature SB circulation onset is best understood on day 154.

SHF, LHF, and MFL, computed from two levels of tower measurements, are shown in Figure 29b. At both towers, especially at Tower 0006, all three surface fluxes show apparent diurnal variations of all three fluxes with SHF being the dominant of the two heat flux terms. The COAMPS^{TM} simulated surface fluxes mirrors such diurnal variations fairly well. There are significant overestimations of the peak LHF, which is over predicted by ~200 Wm^{-2}. Note the q does not show heightened diurnal variation as seen previously. The simulated diurnal variation in LHF is likely a result of strong diurnal variations in near-surface temperature, which results in diurnal variation in near surface q (saturation specific humidity at surface temperature multiplied by moisture availability). It is possible that the general dry bias contributed to the much larger simulated LHF. It is interesting to note that MFL at Tower 0006 was significantly over-predicted in magnitude even though WS for these days were underestimated. This result indicates a substantially larger drag coefficient at Tower 0006 compared to observation.

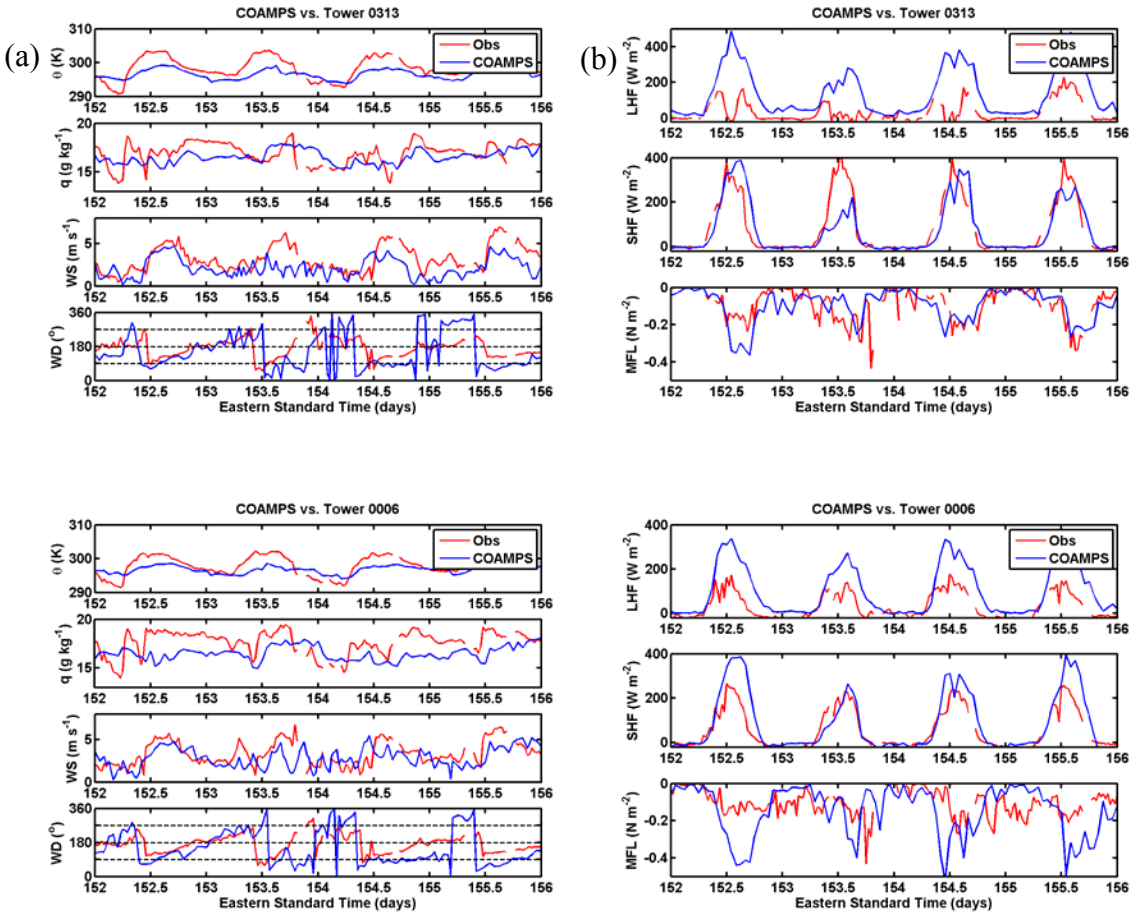

Figure 29. WINDS observation (red) and COAMPS™ (blue) of (a) mean and (b) calculated flux values at Tower 0313 (top) and 0006 (bottom) for Case #1.

2. Case #2, 18–22 June 2008

Case #2 occurred later in springtime than Case #1. However, comparable synoptic conditions and sea surface temperatures still stimulate vigorous coastal circulations over east-central Florida. Figure 30 presents a similar series of contour plots as in Figure 25 but for 19 June 2008. For this particular day, COAMPS™ temperature ranges are 296–300 K again while observations have a slightly lower range of 297–305 K. Beginning at 1100 EST, observations show a sea breeze initiating at coastal towers while COAMPS™ already had onshore flow throughout the region. At 1200 the simulated sea breeze is fully developed and places a relatively tight thermal gradient just west of the Indian River. Despite a significant cold bias, COAMPS™ was able to generate an east-west temperature gradient to reflect the water-land thermal contrast. COAMPS™ did not

reproduce the north-south temperature gradient west of the Indian River in the lower half of the simulated domain as evident in Figure 30c. For this case, the observed sea breeze migration beyond the Indian River does not take place until 1400, which is atypical of other cases. It will be shown later that on average COAMPS^{TM} tended to predict an early sea breeze onset for most days in this study.

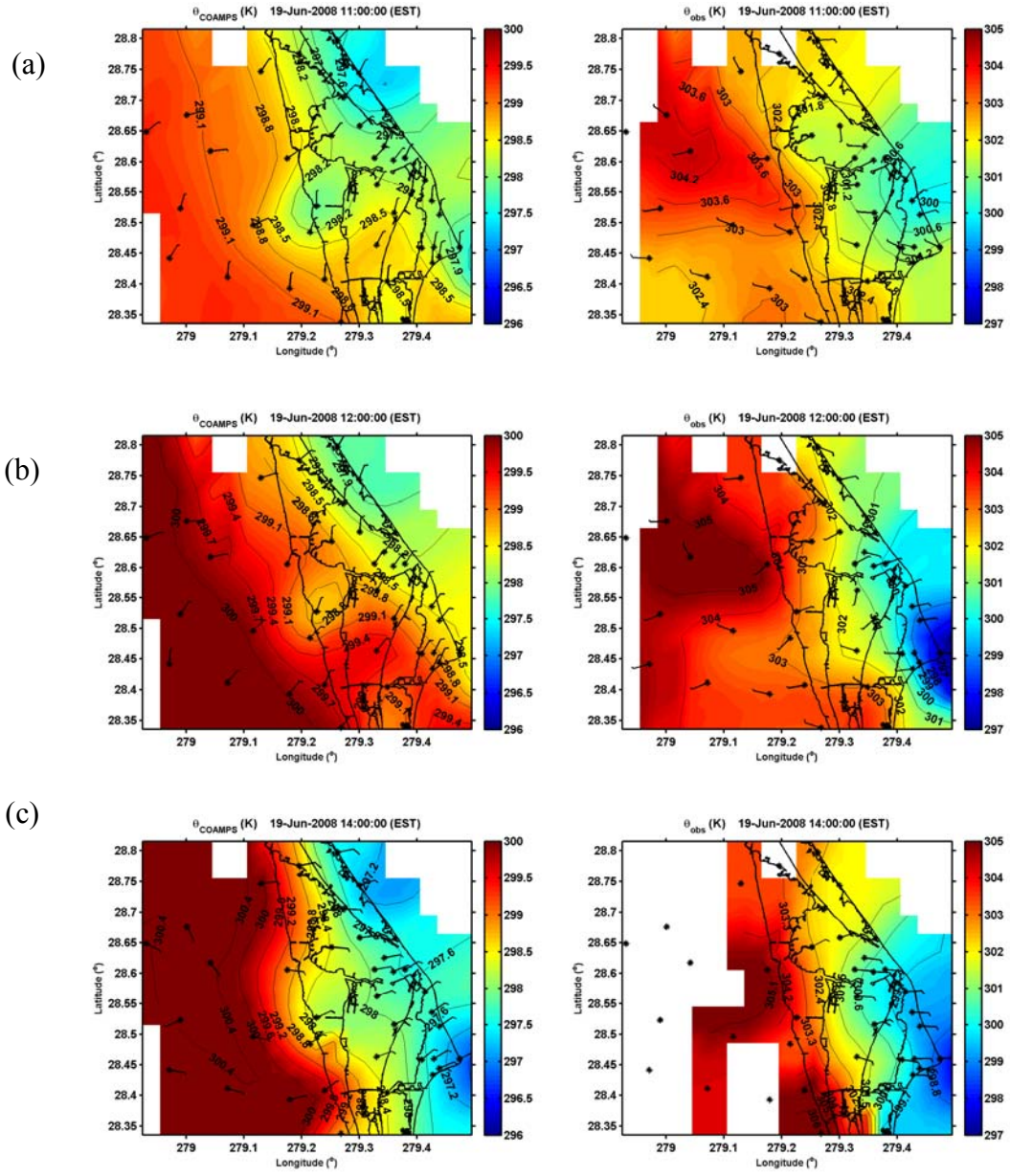

Figure 30. Contour plots comparing COAMPS^{TM} (left) and WINDS observations (right) of potential temperature at (a) 1100, (b) 1200 and (c) 1400 on 19 June 2008.

Figure 31 contains vertical profiles of thermodynamic and wind variables from WINDS observation and COAMPS^{TM} -derived corresponding quantities at Tower 0313 for 0600 and 1200 on 20 June 2008. In both examples, COAMPS^{TM} and observations are consistent to a certain extent. At 0600 EST, a thermally stable nocturnal surface layer is evident in both θ profiles. We note the simulated θ is warmer between 30-100 m above surface. By 1200 UTC, both observation and COAMPS^{TM} revealed an unstable surface layer and the WS forecast is nearly perfect. At this hour, COAMPS^{TM} has a cold bias of ~3 K for nearly all levels. Statistical comparison of multiple cases, to be shown in a later section, suggests COAMPS^{TM} has a warm temperature bias at low temperature values and a cold bias during warm, daytime temperatures. This is likely a reflection of the difference in temperature bias between day and night as seen in Figure 31.

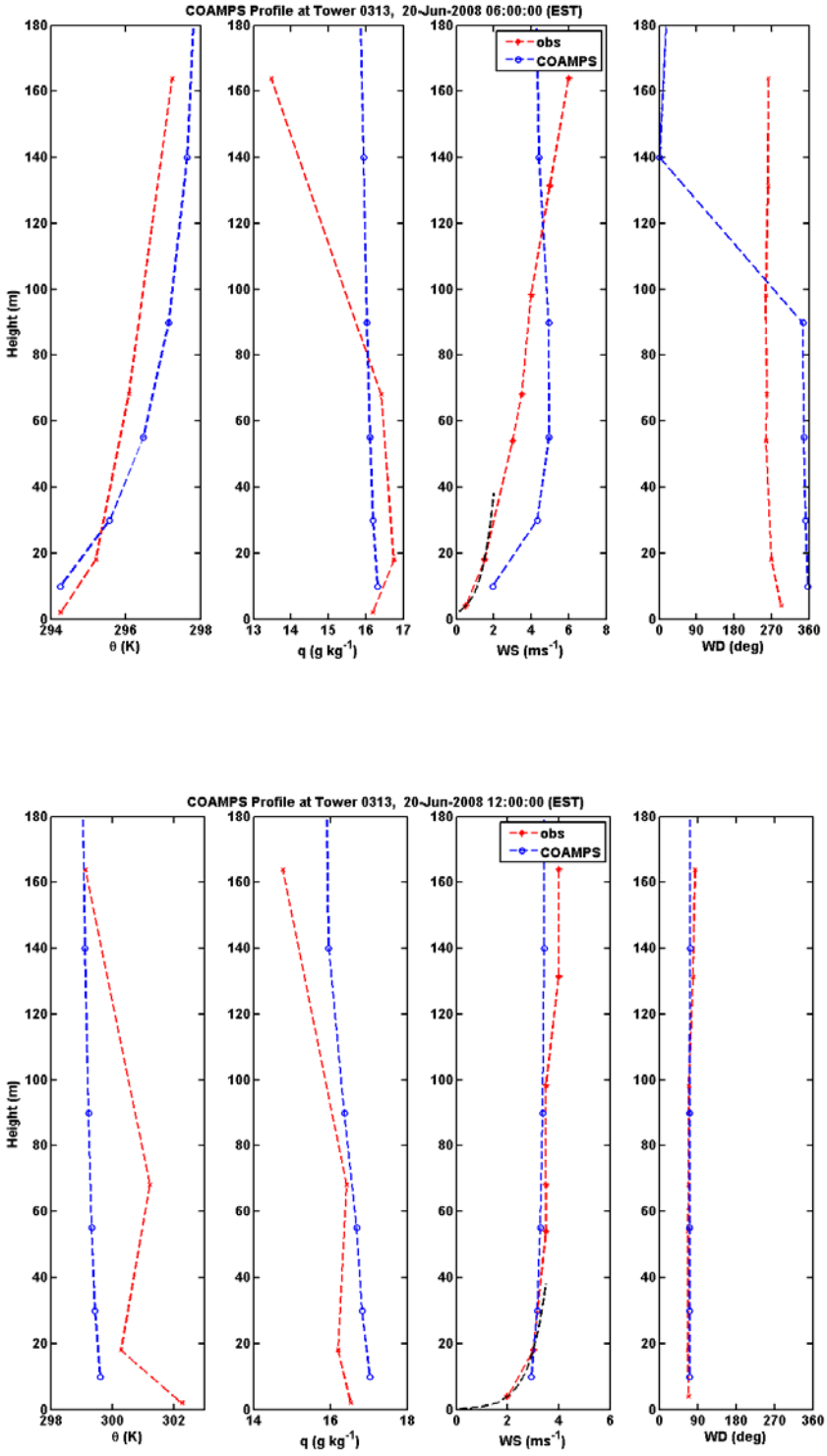

Figure 31. Observed (red) and COAMPS^{TM}-derived (blue) vertical profiles of potential temperature, specific humidity, wind speed, and wind direction from Tower 0313 at 0600 (top) and 1200 (bottom) EST on 20 June 2008.

Figure 32 shows the temporal variation of measured and simulated quantities similar to those in Figure 28 except for Case #2. These comparisons were made for mean and flux measurements at Towers 0313 and 0110. Very similar results were found as compared to Figure 28. COAMPS^{TM} shows a cold bias during maximum afternoon temperatures of ~3 K but equals nighttime temperatures fairly well with only a slight warm bias on certain days. Both towers show marginal q fluctuations and a dry bias of 1-2 g kg^{-1}. This dry bias is more apparent at Tower 0110 which is closer to the coastline by 3 km. COAMPS^{TM} resolves SBF timing of WD shift well on days 169 and 170 but is an hour early on day 171 at both towers. The simulated WS is skillfully resolved but do not depict the higher winds recorded at Tower 0110 beginning in the late afternoon of day 169 and ending the morning of day 170.

Surface fluxes derived from WINDS measurements and the COAMPS^{TM} simulations are shown on the right panels of Figure 32. In case #2, the LHF possessed a weak diurnal variation with afternoon maxima reaching an average 200 Wm^{-2} at both towers with the exception of day 169. On this particular day, Tower 0110 records LHF greater than 400 Wm^{-2} before noon corresponding to peak θ and q values. The COAMPS^{TM} largely overestimated daytime and nocturnal LHF contributions at Tower 0313 likely due to a coinciding dry bias. The SHF maintains a well-defined diurnal variation at both locations with daytime peaks around 200 Wm^{-2}. Temporal differences exist between these two locations with Tower 0313 peaking in the afternoon and Tower 0110 in the midmorning. These temporal differences likely owe to their respective proximity to water sources and the presence of low-level clouds throughout the morning prior to SBF passage. The MFL shows a diurnal variation at Tower 0313 with most forcing occurring during sea breeze periods of high WS. COAMPS^{TM} depicts this diurnal trend at both locations but missed the higher values at Tower 0110 calculated for nighttime of day 169.

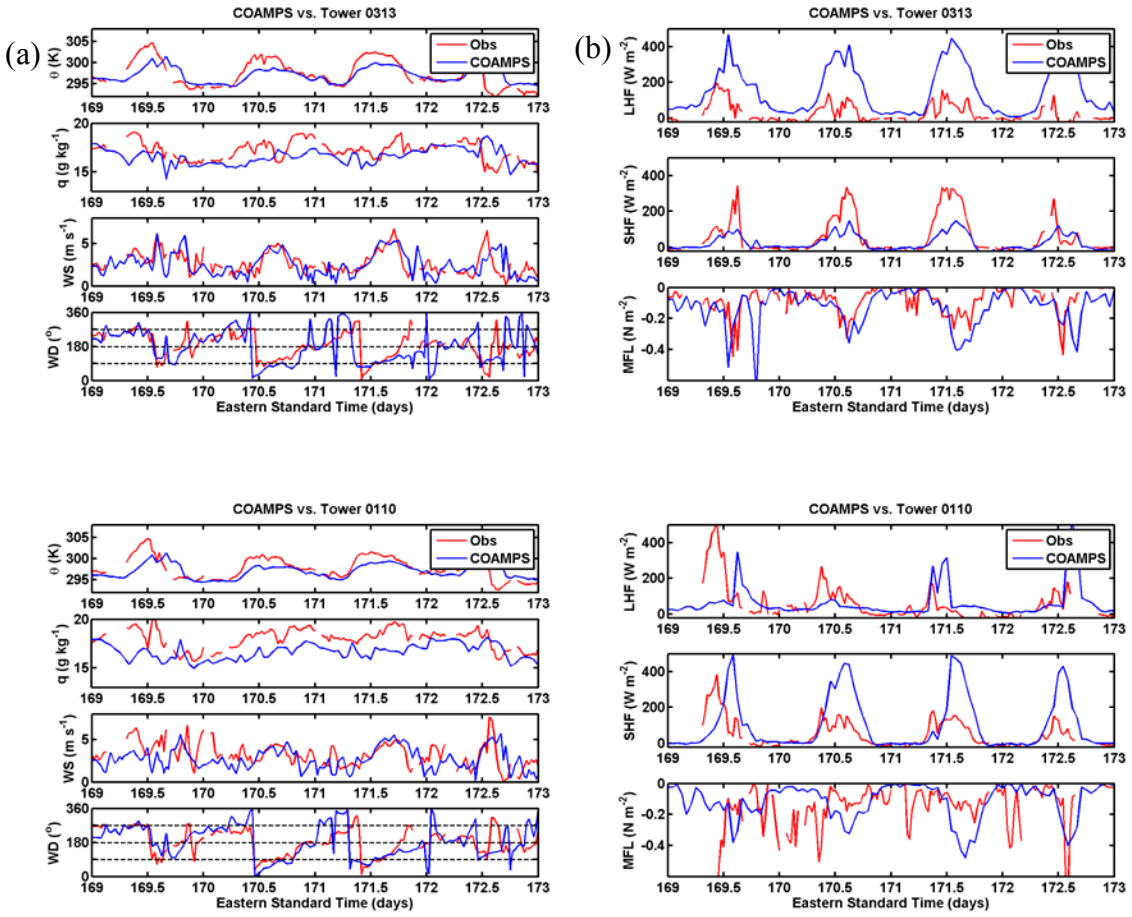

Figure 32. WINDS observation (red) and COAMPS^{TM} (blue) of (a) mean and (b) calculated fluxes at Towers 0313 (top) and 0110 (bottom) from Case #2.

3. Sea and Land Breeze Transition

This section includes subjective analyses on the timing of sea and land breeze onsets observed by the wind towers and simulated by COAMPS^{TM}. For the observational study, we used all 64 sea breeze cases identified from the 2008 measurements, most of which were in spring and early summer. All ten days in Cases #1 and #2 were used for subjective analysis of the COAMPS^{TM} simulations. The identifiable signals of a SBF passage include an abrupt wind direction switch from westerly to southeasterly, a spike in wind speed larger than 4 ms^{-1}, a slight drop in θ and increase in q. We selected 11 out of the 36 towers for this subjective analysis. These 11 towers were chosen based on a near linear path from coastline to as far inland as possible to examine horizontal progression of the coastal circulation across complex surface morphology. All four launch towers

were also included in this study because of the availability of multi-level measurements. Figure 33 is a map with the location of all 11 towers used in this subjective examination. The first two digits of the tower names indicate the distance (in nautical miles) from the coastline at the same latitude.

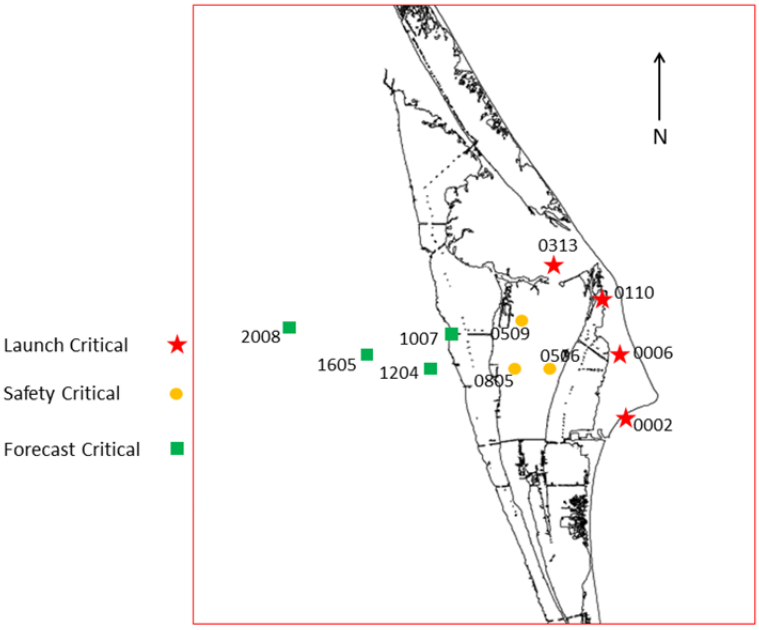

Figure 33. Locations of WINDS towers used for subjective analysis in this study.

Based on the identified SB/LB onset time from each day, an average onset time for each tower was obtained for the observations and COAMPS^{TM} simulations. The results are summarized Figure 34, which shows the SB/LB onset time as a function of distances to coastline. The duration of SB was obtained as the difference between the LB and SB onset time.

Figure 34 shows a gradual SBF progression from coast to inland. In both model and observation, the sea breeze took an average of 2.5 hours to advance from coast to 36 km inland. Larger scattering is seen in the observed data, especially for the SB onset time. The most apparent deviation from other towers is seen at Tower 1007 (at ~18 km from the coast) which indicates an early onshore wind shift by nearly one hour compared to nearby towers. This indicates that local Indian River circulations interfered with the

larger scale coastal circulations. IRBs generally precede SBFs and are difficult to discriminate due to marked similarities in wind and moisture advection characteristics. As a result, the duration of the sea breeze at this point is roughly one hour longer than nearby points. Other variability in SB onset time is also likely associated with local surface morphology. For example, Figure 34a shows a difference of 15 minute in wind shift at the two towers at nearly the same distance from the coast (Towers 0506 and 0509 at ~10 km). The onset time difference at these two points is likely a result of their close proximity to the western Indian River bank and eastern Banana River bank, respectively. Land breezes (Figure 34b) also averaged 2.5 hours to progress from 36 km inland to the coast, normally between 1930 to 2130 EST, and thus, share an inverse relationship to the SB. The LB observed time progression depicts a rather steady progression from inland to the coast. Figure 34c shows the shortest SB period at 36 km inland was about seven hours, while the SB duration at the coastline is about 11 hours from observation.

Compared to observations, COAMPS^{TM} depicts a smooth linear progression of a SBF from coastline to inland. In general, COAMPS^{TM} also began the sea breeze about an hour early at the coast but reached Tower 2008 at roughly the same time. A larger difference is apparent in the LB onset time (Figure 34b) where COAMPS^{TM} postponed the nighttime flow by over one hour at some points. This leads to a longer sea breeze duration and perhaps intensified simulated sensible weather.

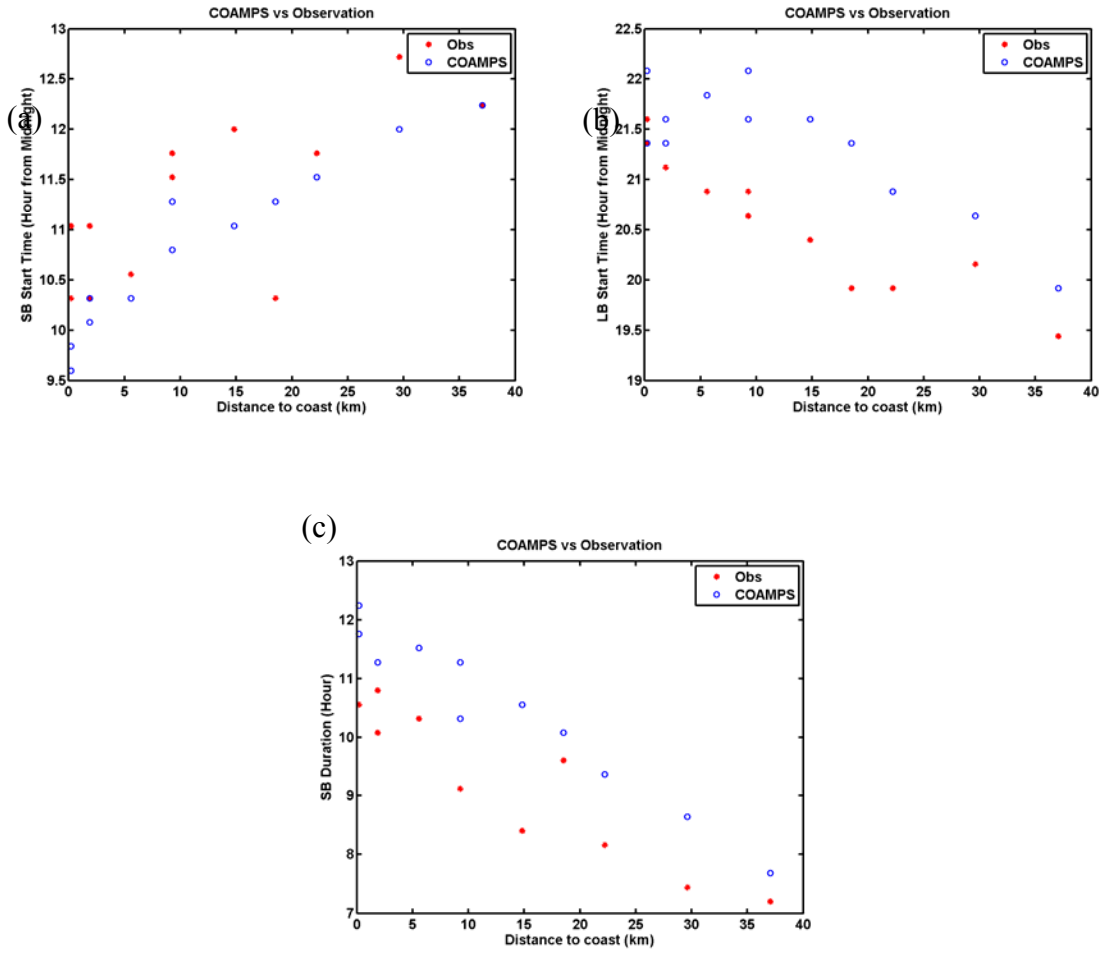

Figure 34. Subjectively analyzed WINDS observation (red) and COAMPS^{TM} (blue) mean time for (a) sea breeze onset; (b) land breeze onset and (c) sea breeze duration.

B. STATISTICAL EVALUATION

Traditional objective evaluation for mesoscale models may not be the best approach in evaluating high resolution models. An attempt is made here, due to the increased number of cases and observations enabling a more accurate representation of the model errors. The scatter plots in Figures 35 and 36 have 502 pairs of mean and surface fluxes from measurements and simulations, comparing COAMPS^{TM} (y-axis) against WINDS towers (x-axis) with a bisecting red line of perfect match (i.e., a point on this line represents a perfect forecast). All COAMPS^{TM} results were interpolated to the time and location of each tower used in this comparison. For the mean variables (wind

speed and direction, potential temperature, and specific humidity), a total of 36 towers were used. For the derived fluxes of momentum and sensible heat, a total of 17 towers were used that have two common levels of measurements in wind and temperature. For latent heat flux, only the four launch towers were used because they host more than one level of relative humidity measurements. Scatter plots are color coded by day as displayed in Figure 35a legend.

A first glance of the θ and q comparison indicate consistent bias of the COAMPS^{TM} simulations for both variables. These biases can be depicted almost as a linear function of magnitude of our predicted respective variable, with negative biases at low temperatures (specific humidity) and increased biases as temperature increases. Figure 35a shows three days are responsible for most of the deviations from the linear bias as evident in θ (day 170, 171, and 173, all from Case #2). For q, day 152 from Case #1 is the apparent outlier from the general trend. Results from our selected statistics defined in Table 1 are shown in Table 2. A mean bias for θ of -2 K and q of -3 g kg^{-1} are the most obvious discrepancies. Relatively large linear correlation coefficient of 0.71 is calculated between the observed and simulated θ, probably due to the strong diurnal variation signal. Conversely, the correlation coefficient for q is very small at 0.33 owing to the reality that simulations for water vapor are particularly difficult in this region because of the multiple water sources in the region including the Banana River, Indian River, and expansive lagoon and marsh land. In Figures 35a and 35b, COAMPS^{TM} θ and q show smaller variation ranges compared to observations, an indication that the model, although at high resolution, is still incapable of resolving perturbations resulting from sub-grid scale surface property variation.

Wind speed is perhaps best simulated among all variables with a small bias of -0.35 and a relative high correlation coefficient of 0.52 (Figure 35c and Table 2). The scatter points to the right of the 1:1 line suggest that COAMPS^{TM} may have difficulties simulating WS greater than 7 ms^{-1}. For wind direction (Figure 35d), the two clusters of points around 100^{o} (observed and simulated) and 250^{o} (observed and simulated) suggests COAMPS^{TM} was able to accurately capture several SB/LB wind shifts. The large scattering in the 180^{o} to 270^{o} range of observed wind shows COAMPS^{TM} has difficulty in

simulating the offshore winds. The error denoted in the COAMPS^{TM} WD scatterplot displays a high bias toward onshore flow when observations show offshore. This correlates well with the subjective analysis of COAMPS^{TM} predicting an early sea breeze onset in Figure 34a. Note: a COAMPS^{TM} forecast of 350° and observation of 10° are only flawed by 20° but show large scatter and seemingly poor forecast skill.

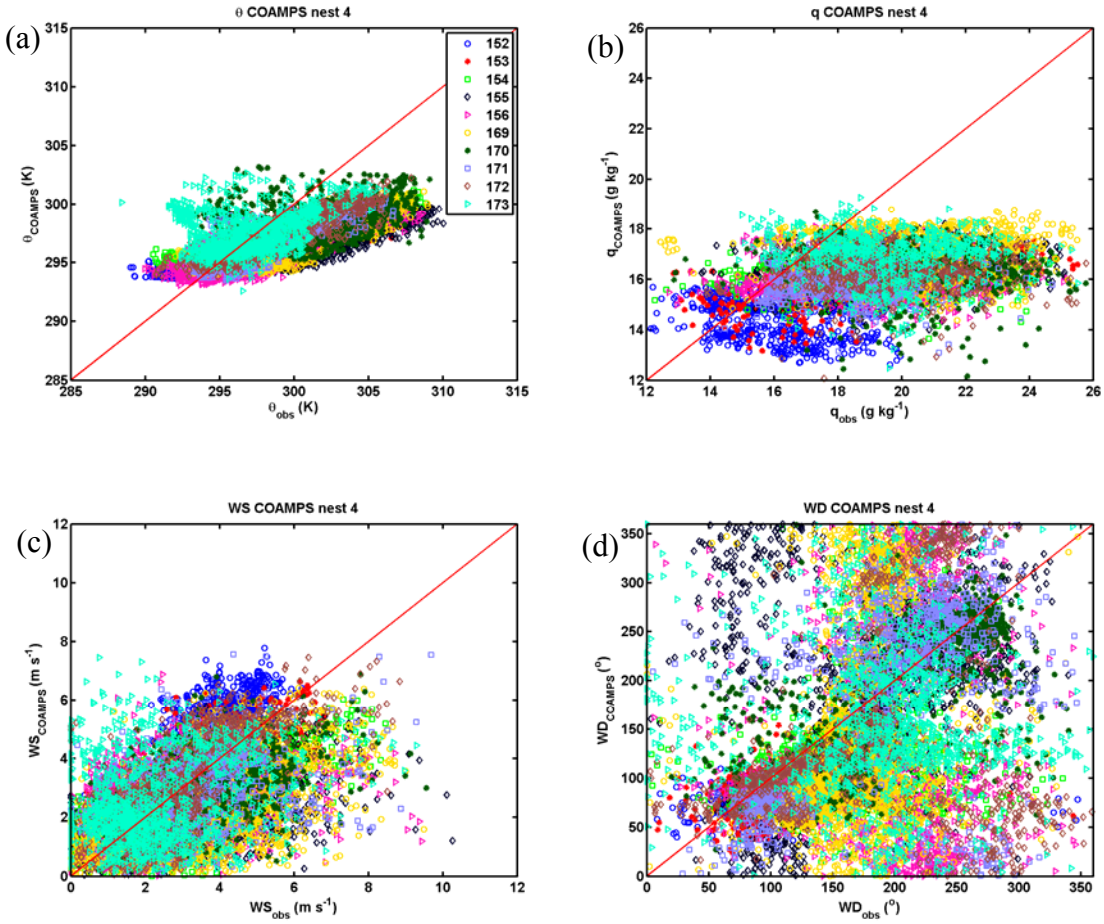

Figure 35. Scatterplot comparing COAMPS^{TM} and observations of (a) potential temperature, (b) specific humidity, (c) wind speed and (d) wind direction color coded by day (legend in θ) in case #1 and #2 to show temporal error variances.

Table 2. Statistical skill score of select COAMPS^{TM} forecast vs. observation variables

	THETA	Q	WS	WD	SHF	MFL	LHF
BIAS	-2.05	-3.01	-0.35	-18.59	8.92	.006	71.31
RMSE	3.39	3.77	1.58	87.91	97.19	0.19	137.07
VARIANCE	2.71	2.26	1.55	85.92	96.79	0.12	117.11
CORR	0.71	0.33	0.52	.381	0.62	0.19	0.41

Evaluation of the surface fluxes are separated by the coastal region and the inland region for momentum and sensible heat fluxes (Figure 36). Towers in the coastal region are defined as those within 10 km of the coast and those from the inland are towers more than 10 km away from the coast. Figure 36 shows larger momentum flux in general, both near the coast and inland. Over the inland towers, however, COAMPS^{TM} is more likely to produce lower momentum fluxes, especially in higher wind conditions. This is consistent with previous results of mean wind comparison indicating that COAMPS^{TM} tends to under-predict mean wind speeds greater than 7 ms^{-1}.

Larger sensible heat flux scattering is seen in Figure 36a (coastal towers), although no true bias is represented. Further inland, COAMPS^{TM} holds a consistent bias to produce larger SHF by significant amount. This bias is not apparent in the averaged skill score when all locations are considered (Table 2). In the stable surface layer regime (negative sensible heat flux), COAMPS^{TM} seemed to produce better heat flux compared to observations. Latent heat flux is significantly over-predicted by COAMPS^{TM}. This is expected giving the substantial q dry bias (Figure 35b). The current measurements only have data from four coastal towers. It is not clear how representative this result is to inland locations.

The trend of sensible heat flux over-prediction by COAMPS^{TM} is tied to the cold bias in COAMPS^{TM} discussed earlier. Although coastal and inland θ shows a similar linear bias trend, the inland temperature varied over a broader range especially in the high temperature end (290 K to 305 K near the coast vs. 290 K to 310 K inland, not shown). As a result, the COAMPS^{TM} simulations produced a larger magnitude of temperature bias which propagated into the parameterized surface sensible heat flux.

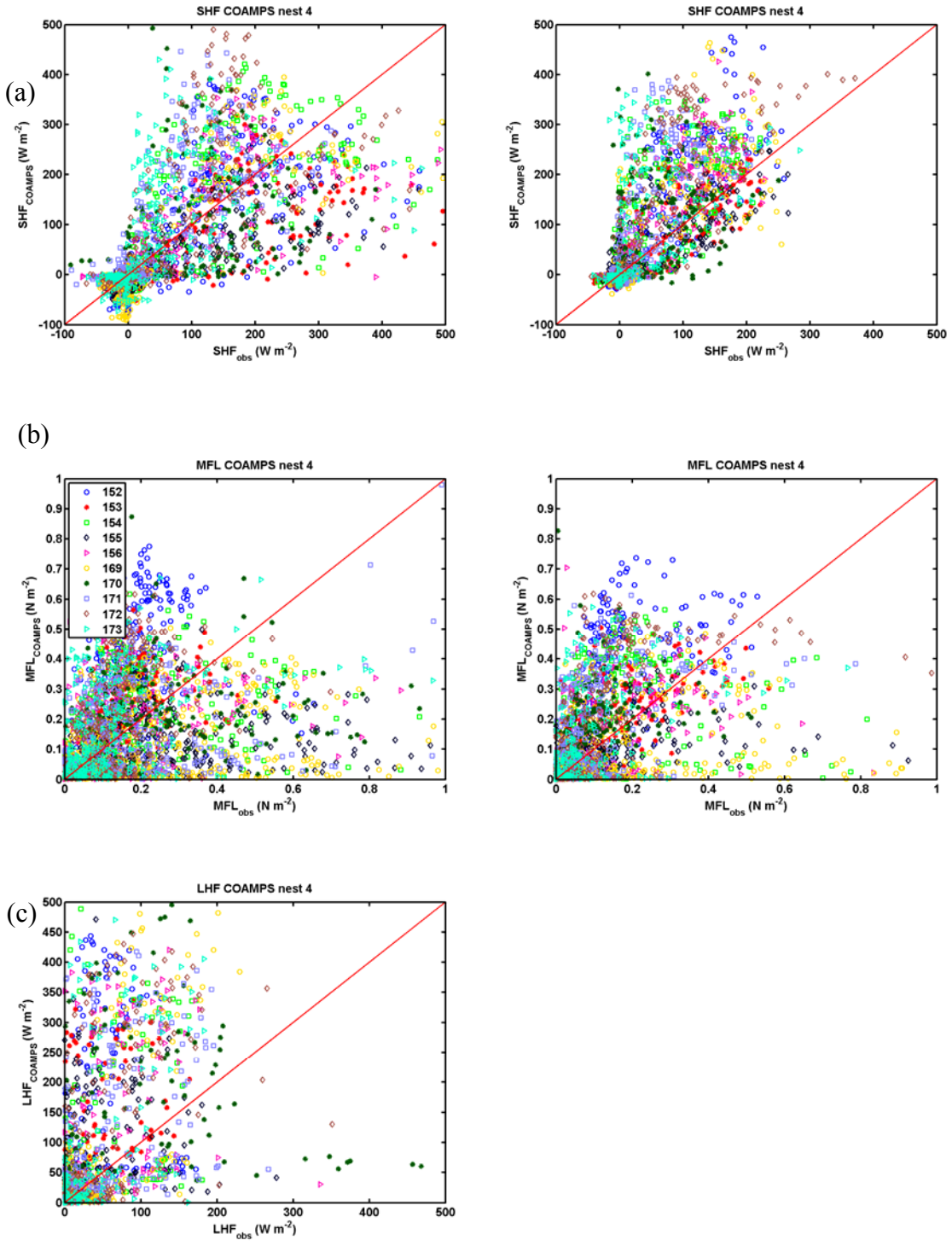

Figure 36. Scatterplots comparing COAMPS^{TM} and observation of (a) sensible heat, (b) momentum and (c) latent heat fluxes at the coast (left) and inland (right) color coded by each day (legend in MFL) in case #1 and #2 to show temporal error variances.

Figure 37 contains mean bias Contour Error Maps (CEM) of θ, q, WS and WD from all towers. The CEM concept was adapted from Case and Manobianco (2004) and incorporated into this study to interpret the spatial forecast error distribution. If we ignore the regions north of 28.7° latitude where only few observational towers are available, we can see a clear error distribution trend in the region. Figure 37a shows the smallest θ and q bias occurred nearest the coast. WD is also simulated better near the coast with largest error west of the Indian River. WS showed a slight high bias inland and low bias near the coast. Weaker inland heating in COAMPS™ is likely to produce a weaker sea breeze circulation consistent with the negative bias in coastal wind speeds.

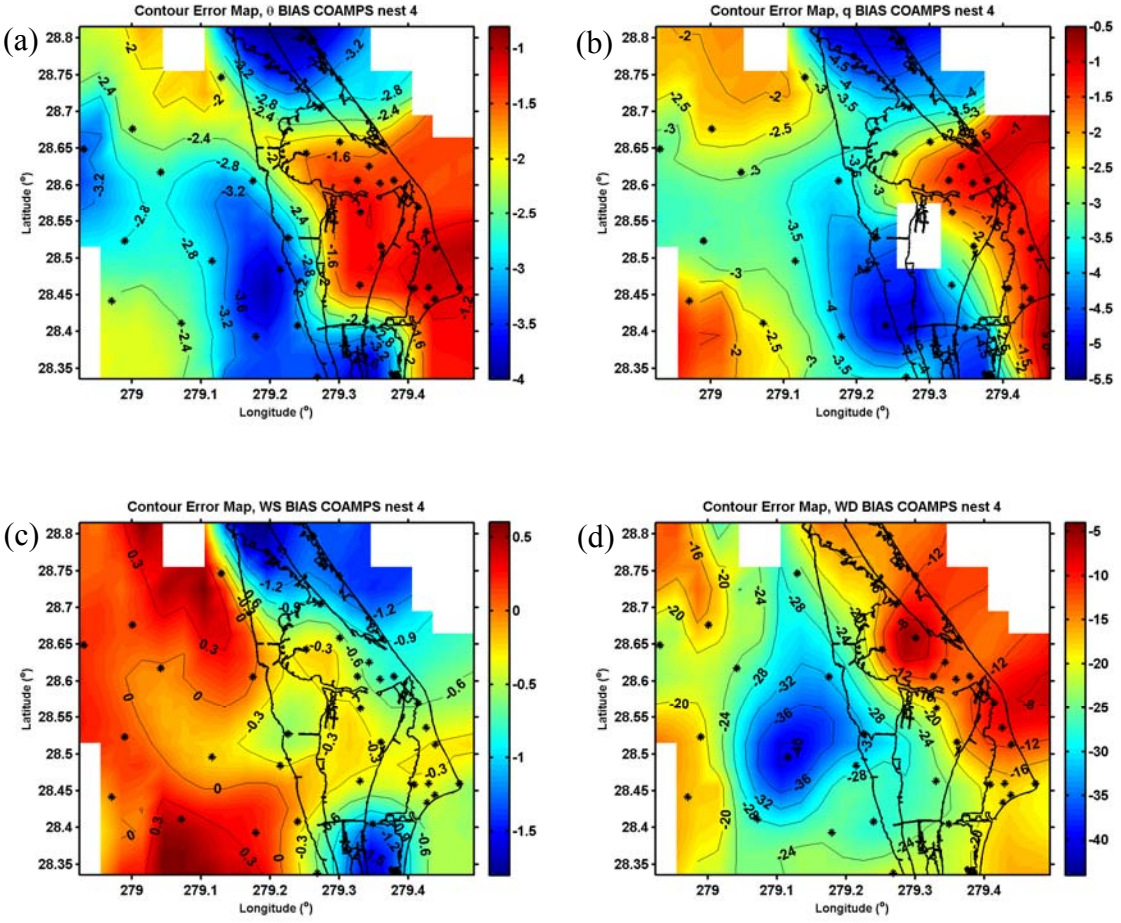
(a)
Contour Error Map, θ BIAS COAMPS nest 4
(b)
Contour Error Map, q BIAS COAMPS nest 4
(c)
Contour Error Map, WS BIAS COAMPS nest 4
(d)
Contour Error Map, WD BIAS COAMPS nest 4
Latitude (°)
Longitude (°)

Figure 37. Error bias Contour Error Maps of observation and COAMPS™ for (a) potential temperature, (b) specific humidity, (c) wind speed, and (d) wind direction with distance from shore.

To further examine how discrepancies between the COAMPS^{TM} simulated cases and observation vary according to distances from the coastline, Figure 38 plots the error statistics listed in Table 1 against distance from shore. All skill scores in Table 1 were calculated for θ, q, WS, WD, MFL and SHF.

Figure 38a for potential temperature shows the model bias being separated into two groups: coastal sites within about 18 km of the coast with a bias of less than 2 K, or inland sites with a bias of 2-5 K. A few coastal sites also have a bias greater than 2 K, the reason for these outliers are yet to be identified. Simulated θ error can also be seen to increase away from the coast while the correlation coefficient becomes increasingly large further inland. This correlation increase between model and observation is a result of dominant diurnal variation well-predicted by COAMPS^{TM}. For q, the bias and RMSE do not show any separation between the coast and inland. The only clear signal to show simulated q varied further inland is that the COAMPS^{TM} results and observations are less correlated away from the coast. WS and WD seem to show an opposite variation trend with distance from the coast. For wind speed, the RMSE and error variance decreases almost linearly with distance from the coast while correlations increase. This result proves COAMPS^{TM} holds a forecast consistency for WS in this region. The same skill score for wind direction shows an opposite trend. The COAMPS^{TM} forecast WS carries an acceptable 1–2 ms^{-1} negative bias suggesting forecasted post SBF winds are slightly too weak. This is supported in the correlation plot as values increase further away from the coast suggesting WS forecasts mirrored observations further inland where a SBF might not have extended. For the increasing error in WD away from the coast, it might also be a result of the SBF's inland penetration being miscalculated.

The SHF and MFL skill scores do not show consistent variation from the coastline. Although the overall mean bias is not large, the large RMSE and error variance suggest problematic surface flux representation for each time instance. Results in Figure 36 suggested flux errors can vary significantly from day to day and by location with significant bias towards higher or lower values. While we are examining the error statistics against the observations, it should be kept in mind that the 'observed' surface fluxes were derived using Monin-Obuhkov similarity and the associated empirical

functions. These flux estimates have inherent error although we have gone through a significant QC process. Unfortunately, without fluxes from direct eddy correlation methods, these derived fluxes are our only source of observation.

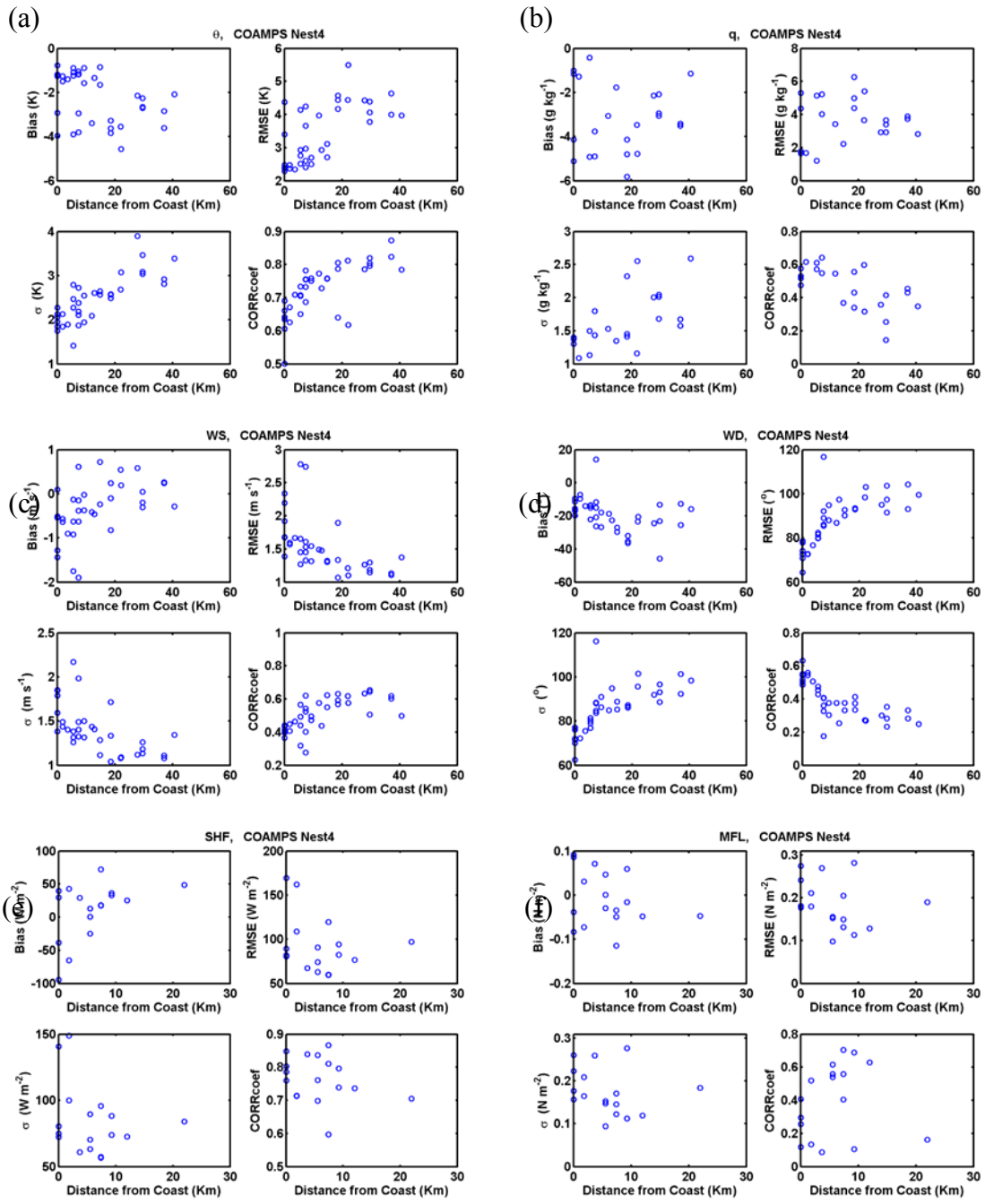

Figure 38. Statistical analysis of observation and COAMPS™ for (a) potential temperature, (b) specific humidity, (c) wind speed, (d) wind direction, (e) sensible heat flux and (f) momentum flux with distance from shore.

VI. SUMMARY AND CONCLUSION

A. SUMMARY

Coastal thermal circulations occur regularly at KSC/CCAFS during the warmer months. The region surrounding KSC/CCAFS contains diverse surface types including urban areas, marshes, temperate forest, barrier islands, sheltered inland waters and the Atlantic Ocean. The coastal circulation in the region is modified by the presence of complex surface characteristics despite a relatively flat terrain profile. A unique feature of KSC/CCAFS sea breeze is the complex interaction between the SBF and the IRB which results in flow convergence near the Indian River.

WINDS towers and DWRP profilers are key components of the mesonetwork around KSC/CCAFS region. In this study, we used measurements from all 36 wind towers and all five wind profilers. A total of 17 wind towers has two common vertical levels of measurements and hence were used to calculate surface fluxes of momentum and sensible heat flux. Four towers had multi-level relative humidity measurements to allow calculations of the moisture flux (latent heat flux). Four of the five profilers functioned properly to allow analyses on the vertical extent of the sea breeze circulation. Much of the efforts were spent on quality checking of the data to avoid possible flow distortion of the tower structure and to eliminate measurements with insufficient precision or accuracy. Two sets of datasets, one for the mean quantity with 36 towers and one for the flux quantities with 17 wind towers, were created as the final product of data quality control.

The objective of this thesis work is to evaluate the performance of COAMPS^{TM} in simulating coastal circulations under weak large-scale forcing. Coastal circulations have been simulated by many studies in the past. However, a thorough evaluation with the focus on near surface mean and turbulence properties is rare. The dense network of measurements by the WINDS towers and profilers in the CCAFS region provides a unique dataset for evaluating mesoscale models from different perspectives. This research takes advantage of the dense population of sensors to examine how the

simulated results vary at different locations relative to the coastline. It is a first step in understanding the model behavior for future model improvements.

In this study, we first analyzed the observational data to identify temporal and spatial variability of the coastal circulation and the associated surface layer mean properties and surface fluxes. For the period of 2008, we identified 64 days with clear signals of a sea breeze circulation. All these sea breeze days were used to document the onset times of sea breeze and land breeze circulations. We then picked two five-day periods where sea breeze circulation can be identified on each consecutive day. For these two periods, labeled as Cases #1 and #2, COAMPS^{TM} simulations were made with the inner-most grid resolution of 3 km. The simulated results within these 10 day period were analyzed and compared with the observational results.

A variety of model verification analyses were employed to analyze and compare the simulated sea breeze against independent WINDS data during the Case #1 and Case #2 time periods. Our research focused on the errors in the simulated Cases #1 and #2 by comparing COAMPS^{TM} surface layer and surface fluxes during a mesoscale circulation. This coastal circulation is selected for COAMPS^{TM} evaluation due to the high frequency of occurrence, critical role in precipitation, and an abundance of meteorological data in this particular region.

Comparison of the COAMPS^{TM} simulated mean field indicate that COAMPS^{TM} captured the diurnal variations of temperature and wind fields fairly well although with small magnitude of the diurnal extremes. The diurnal variation of specific humidity was not prominent either in tower observations or in COAMPS^{TM}. From the scatter plot between observations and simulated results, it was clear that COAMPS^{TM} consistently shows a mean bias for temperature and specific humidity, with a small magnitude for the mean wind. The bias for both temperature and humidity varies with the observed mean temperature or q with larger bias at larger temperature or q. Close examination of the data points by separating them by day and by location relative to the coast, it was clear that most of the lower temperature range where COAMPS^{TM} had positive bias were in the nighttime nocturnal boundary layers, while the higher temperature instances with significant cold bias have to do with the daytime convective boundary layers. These

results were also supported by comparisons of the low level wind and thermodynamic profiles from the tall tower (0313). Overall, a cold bias of roughly 3 Kelvin exists inland where large daytime maximum temperatures occurred. This error was not so prominent near the coastline where temperatures were moderated by numerous waterways and daily SBF passage. COAMPS^{TM} also held a ~2 gkg^{-1} dry bias near the coast. In general, COAMPS^{TM} shows a smaller range of variability during any given day compared to the observations, which is consistent with the model not being able to resolve the effects of small surface features.

Wind speed prediction was fairly accurate with a slight low bias near the coast and high bias inland. Wind direction errors were larger inland than near the coast. A large reason for these errors is likely linked to a poorly simulated SBF inland extent and intensity. A comparison of sea breeze and land breeze onset times indicated that COAMPS^{TM} tends to simulate an early onset of the sea breeze which also lasted slightly longer. A key result showed that regions between the simulated and observed SBF had a high wind bias owing to the fact that winds speeds increase following a SBF.

Time evolution plots showed that simulated sensible heat, latent heat and momentum fluxes followed a diurnal curve consistent with surface fluxes derived from the tower observations. The observed surface flux diurnal variation is modulated by significant variability stemming from surface layer mixing influenced by nearby local surface properties. These small temporal and spatial variations cannot be accounted for in COAMPS^{TM}. This variability also leads to substantial scattering as seen in comparison plots with reduced correlation from observations. With inherent smoothing and filtering in numerical models, adequate depiction of fine spatial and temporal variability observed at individual sensors cannot be adequately simulated unless the model contains resolutions equivalent to large eddy simulation models.

The significantly large inland SHF and LHF at the four coastal towers seen in COAMPS^{TM} reflect the bias in the simulated air temperature (cold), surface temperature (not discussed in this thesis), as well as in specific humidity (dry). These biases have been identified by previous studies using COAMPS^{TM}, but are confirmed with the cases studied here. Through the enhanced surface fluxes, such bias would affect boundary layer

dynamics and hence the entrainment exchange with the free atmosphere. These discrepancies will eventually propagate and increase through all modeled field variables. The surface fluxes are also essential to the existence and strength of a sea breeze circulation. The COAMPS^{TM} over forecasted SHF values were a likely cause of the stronger SBF than observation. The MFL is important for producing the observed surface wind profile and prevents extremely high wind speeds in the near surface. The over forecasted MFL quantities likely aided the stunted wind speeds mentioned above.

Each surface feature possesses distinct roughness length and flux properties. Evidence was presented to show observed interruptions of inland progression as SBF interacted with numerous waterways and diverse landscape. The simulated SBF tended to smooth these complex surface interactions and temporal progression was often over forecasted. This is likely caused by the COAMPS^{TM} tendency to smooth naturally occurring randomness in surface properties.

The sea breeze vertical extent ranged between 800–1000 m in height and varied by amount of SHF and proximity to surface features. Profiler wind data showed a relationship of varying vertical height between Profiler #1 and Profiler #5 with the latter showing considerably less height than the former. This difference was concluded to be based upon relation to the Atlantic Ocean coastline since Profiler #5 resides further inland.

B. RECOMMENDATION FOR FUTURE RESEARCH

Wind speed observations with a precision of about 0.05 ms^{-1} is measured and recorded by the WINDS sensors, but was not available for this study. Use of this high-precision data would have greatly increased the accuracy of surface-layer flux calculations for all cases. For future work, it is recommended that this high-precision data be acquired and exploited for boundary layer research.

This study represents an initial effort to quantify the skill of COAMPS^{TM} to simulate a coastal circulation in region complex surface characteristics. Additional research should be conducted to fully identify the source of the errors and therefore provide guidance for model improvements.

Synoptic scale phenomena routinely affect this region in the colder months. Future utilization of this dense meteorological data set and conduction of similar studies to synoptic-scale weather phenomena could benefit a multitude of audiences. Thorough examination of migrating cold fronts will likely yield different results since near surface winds and sensible heat fluxes will be unlike coastal circulations. Similar evaluation of high-resolution mesoscale model output could reveal boundary layer responses to clouds and precipitation.

THIS PAGE INTENTIONALLY LEFT BLANK

APPENDIX. CCAFS WINDS TOWER LOCATIONS AND INSTRUMENT COMPLEMENTS

Table 3. Locations and instrumentation heights for the four launch critical WINDS towers and CCAFS used in this study (After CSR 2006).

TOWER #	LOCATION	INSTRUMENTATION HEIGHT (m)		
		Wind	Temperature	RH
0002	28° 26' 39" N 80° 33' 44" W	62.2 44.2 27.4 16.5 3.7 -	62.2 - - 16.5 - 1.8	62.2 - - 16.5 - 1.8
0006	28° 30' 47" N 80° 33' 41" W	62.2 49.4 16.5 3.7 -	62.2 - 16.5 - 1.8	62.2 - 16.5 - 1.8
0110	28° 34' 11 N 80° 35' 12" W	62.2 49.4 16.5 3.7 -	62.2 - 16.5 - 1.8	62.2 - 16.5 - 1.8
0313[2]	28° 37' 32" N 80° 39' 26" W	150.0 120.1 89.9 62.2 49.4 16.5 3.7 -	150.0 - - 62.2 - 16.5 - 1.8	150.0 - - 62.2 - 16.5 - 1.8

[1] Launch critical towers support dual instrumentation packages at each level, aligned northwest to southeast on Towers 0002, 0006, and 0110; and northeast to southwest on Tower 0313.

[2] Tower 0313 also houses redundant Vaisala PTB220 Series barometric pressure sensors at 1.8 m AGL (4.3 m MSL).

Table 4. Locations and instrumentation heights for the 14 safety critical WINDS towers at CCAFS used in this study (After CSR 2006).

TOWER #	LOCATION	INSTRUMENTATION HEIGHT (m)		
		Wind	Temperature	RH
0001	28° 26’ 02” N 80° 34’ 25” W	16.5 3.7 -	16.5 - 1.8	-
0003	28° 27’ 35” N 80° 31’ 37” W	16.5 3.7 -	16.5 - 1.8	-
0108	28° 32’ 09” N 80° 34’ 30” W	16.5 3.7 -	16.5 - 1.8	-
0211	28° 36’ 22” N 80° 37’ 18” W	16.5 3.7 -	16.5 - 1.8	-
0303	28° 27’ 36” N 80° 34’ 17” W	16.5 3.7 -	16.5 - 1.86	-
0311	28° 36’ 10” N 80° 38’ 29” W	16.5 3.7 -	16.5 - 1.8	-
0403	28° 27’ 31” N 80° 35’ 33” W	16.5 3.7 -	16.5 - 1.8	-
0412	28° 36’ 23” N 80° 34’ 03” W	16.5 3.7 -	16.5 - 1.8	-
0415	28° 39’ 31” N 80° 42’ 00” W	16.5 3.7 -	16.5 - 1.8	-
0506	28° 30’ 57” N 80° 38’ 24” W	16.5 3.7 -	16.5 - 1.8	-
0509	28° 33’ 44” N 80° 40’ 10” W	16.5 3.7 -	16.5 - 1.8	-
0714	28° 38’ 35” N 80° 44’ 54” W	16.5 3.7 -	16.5 - 1.8	-
0803	28° 27’ 47” N 80° 40’ 13” W	16.5 3.7 -	16.5 - 1.8	-
0805	28° 31’ 05” N 80° 41’ 47” W	16.5 3.7 -	16.5 - 1.8	-

LIST OF REFERENCES

Abbs, D. J., 1986: Sea breeze interactions along a concave coastline: Observations and numerical modeling study. *Monthly Weather Review*, **114**, 831–848.

Baker, R. D., B. D. Lynn, A., Boone, W. K. Tao, and J. Simpson., 2001: The influence of soil moisture, coastline curvature and land breeze circulations on sea breeze-initiated precipitation. *Journal of Hydrometeorology*, **2**, 193–211.

Benson, J., 2005: *Boundary Layer response to a change in surface roughness.* Masters of Science Thesis, University of Reading, August 2005.

Boybedi, Z., and S. Raman, 1992: A three-dimensional numerical sensitivity study of convection over Florida Peninsula. *Boundary Layer Meteorology*, **60**, 325–359.

Businger, J. A., J. C. Wyngaard, Y. Izumi, and E. F. Bradley, 1971: Flux-profile relationship in the atmospheric surface layer. *Journal Atmospheric Science*, **28**, 181–189.

Case, J., M. Wheeler, and J. Manobianco, 2003: A 7-year Climatological Study of Land Breezes over Florida Spaceport. *Journal of Applied Meteorology*, **44**: 340–356.

Cheng, H., and I. P. Castro, 2002: Near wall flow over urban-like roughness. *Boundary Layer Meteorology*, **104**, 229–259.

Computer Sciences Raytheon, 2006: *Eastern Ranges Instrumentation Handbook*, CDRL A209, Contract F08560–00-C-0005.

Couralt, D., P. Drobinski, Y. Brunet, P. Lacarrere, and C. Talbot, 2007: Impact of surface heterogeneity on a buoyancy-driven convective boundary layer in light winds. *Boundary Layer Meteorology*, **124**, 383–403.

Crosman, E. T., and J. D. Horel, 2010: Sea and lake breezes: A review of numerical studies. *Boundary Layer Meteorology*, **137**, 1–29.

Ellis, M., Capt, USAF, 2010: *Roughness length variability over heterogeneous surfaces.* M.S. thesis, Naval Postgraduate School, March 2010.

Esbensen, S. K., and D. Vickers, 1998: Subgrid surface fluxes in fair weather conditions during TOGA COARE: Observational estimates and parameterization. *Monthly Weather Review*, **126**: 620–633.

Garratt, J. R., 1992: *Atmospheric Boundary Layer*, Cambridge University Press, 316 pp.

Gilliam, R. C., S. Raman, and D. Niyogi, 2004: Observational and numerical study on the influence of large-scale flow direction and coastline shape on sea-breeze evolution. *Boundary Layer Meteorology*, **111**, 275–300.

Hodur, R. M., 1997: The Naval Research Laboratory's Couple Ocean/Atmosphere Mesoscale Prediction System (COAMPS^{TM}). *Monthly Weather Review*, **125**: 1414–1430.

Kalnay, E., 2003: *Atmospheric Modeling, data Assimilation and Predictability*, Cambridge Univ. Press, 341 pp.

Laird, N. F., D. A. R. Kristovich, R. M. Rauber, H. T. Ochs III, and L. J. Miller, 1995: The Cape Canaveral sea and river breezes: Kinematic structure and convective initiation. *Monthly Weather Review*, **123,** 2942–2956.

Louis, J. F., 1979: A parametric model of vertical eddy fluxes in the atmosphere. *Boundary Layer Meteorology*, **17**, 187–202.

Mahrt, L., C. K. Thomas, and J. H. Prueger, 2009: Space-time structure of mesoscale motions in the stable boundary layer. *Quarterly Journal Royal Meteorology Soc*., **135**, 1–9.

Mahrt, L., and D. Vickers, 2010: Sea-surface roughness lengths in the midlatitude coastal zone. *Quarterly Journal Royal Meteorology Soc*., **5**, 1–11.

Mellor, G., and T. Yamada, 1974: A hierarchy of turbulence closure models for planetary boundary layers. *Journal of Applied Meteorology*, **31,** 1792–1806.

Miller, S.K., B.D. Keim, R.W. Talbot, and H. Mao, 2003: Sea breeze structure, forecasting and impacts. *Journal of Geophysical Research*, **41**, 1–131.

NRL Publication, 2003: *General Theory and Equations-Coupled Ocean/Atmosphere Mesoscale Prediction System (COAMPS^{TM})*. pp. 33–66. NRL/PU/7500--03–448.

Porson, A., D.G. Steyn, and G. Schayes, 2007: Sea breeze scaling from numerical model simulations. *Boundary Layer Meteorology*, **122**, 17–41.

Rao, P.A., and H.E. Fuelberg, 2000: An investigation of convection behind the Cape Canaveral sea-breeze front. *Monthly Weather Review*, **128**, 3437–3458.

Reed, J. W., 1979: Cape Canaveral sea breezes. *Journal of Applied Meteorology*, **18**, 231–235.

Savijarvi, H., and S. Matthews, 2004: Flow over small heat islands: a numerical sensitivity study. *Journal of Atmospheric Science*, **61**, 859–868.

Segal, M., Purdom, J., Song, J., Pielke, R., and Y. Mahrer, 1986: Evaluation of cloud shading effects on the generation and modification of mesoscale circulations. *Monthly Weather Review*, **114**, 1201–1212.

Simpson, J. E., 1996: Diurnal changes in sea-breeze direction. *Journal of Applied Meteorology*, **35,** 1166–1169.

Stull, R. B., 1988: *An Introduction to Boundary Layer Meteorology*, Springer 670 pp.

Wakimoto, R. M., and N. T. Atkins, 1994: Observations of the sea breeze during CaPE: single Doppler, satellite and cloud photogrammetry analysis. *Monthly Weather Review*, **122**, 1092–1114.

Wang, Q., 2012: *Air-Sea Interaction*. Naval Postgraduate School, MR4413 lecture notes.

14th Weather Squadron (14 WS), cited 2013: Patrick AFB, Florida Narrative. [Accessed online at http://www.meted.ucar.edu/afwa/climo/operations/media/patrick_narr.pdf].

Xian, Z., and R. E. Pielke, 1991: The effects of width of land masses on the development of sea breezes. *Journal of Applied Meteorology*, **30**: 1280–1304.

Zhong, S., and E.S. Takle, 1992: Observational study of sea and land breeze circulations in an area of complex coastal heating. *Journal of Applied Meteorology*, **32**: 1426–1438.

THIS PAGE INTENTIONALLY LEFT BLANK

INITIAL DISTRIBUTION LIST

1. Defense Technical Information Center
   Ft. Belvoir, Virginia

2. Dudley Knox Library
   Naval Postgraduate School
   Monterey, California

3. Prof. Qing Wang
   Naval Postgraduate School
   Monterey, California

4. Prof. Wendell Nuss
   Naval Postgraduate School
   Monterey, California

5. Air Force Weather Technical Library
   Asheville, North Carolina